

**PHOTON FACTORY
ACTIVITY REPORT**

1987

5

**PF
10th
Anniversary**



NATIONAL LABORATORY FOR HIGH ENERGY PHYSICS, KEK

PHOTON FACTORY
ACTIVITY REPORT
1 9 8 7



Editorial Board

ANAMI Shozo

IIDA Atsuo*

FUKUDA Shigeki

KATSURA Kyotaro

KOBAYASHI Masanori

SAKABE Noriyoshi

(*Chief editor)

KEK Progress Reprt 87-2

(C) National Laboratory for High Energy Physics, 1987

KEK Reports are available from

Technical Information Office

National Laboratory for High Energy Physics

1-1 Oho, Tsukuba-Shi

Ibaraki-Ken, 305

JAPAN

Phone : 0298-64-1171

Telex : 3652-534 (Domestic)

(0)3652-524 (International)

Cable : KEKOH

You can jump to the article by clicking its title.

contents

Preface	5
Outline of the Photon Factory	7
1. Introduction	11
2. History	11
3. Plan of the facility	16
4. Organization and staff	16
5. Budget	16
6. Operation time and proposal	17
7. List of Proposals	21
7.1 Proposal accepted by Program Advisory Committee	
7.2 Proposals accepted for charged beam time assessment	
8. PF seminars, meetings and publications	34
Injector Linac Department	37
1. Introduction	39
2. Progress of the positron generator injection	40
2.1 Electric gun system development	
2.2 Modification of the waveguide system	
2.3 Acceleration characteristics of the positron generator injector	
3. Improvement of the PF linac injector	43
3.1 The electron gun system	
3.2 The rf control system for the prebuncher and buncher	
4. Improvements of the positron focussing system	45
4.1 The modification of the beam transport of the primary electron beam	
4.2 Modification of the positron target	
5. High gradient acceleration by recirculator	46
5.1 The recirculating accelerator structure	
5.2 Test of the high gradient acceleration	
6. The microwave source	48
6.1 Operational status	
6.2 Phase control	
7. Control system	50
7.1 Display system for control console	
7.2 Monitoring system for krystron RF outputs	
Light Source Department	53
1. Introduction	55
2. Operation	56
2.1 Operation	
2.2 Low emittance operation	
2.3 Beam dynamics	
3. Improvements	63
3.1 Injection	
3.2 Improved RF-cavities and high power tests	
3.3 Vacuum	
3.4 Superconducting vertical wiggler	
3.5 Photon beam stabilization	
3.6 Beam channel	
Instrumentation Department	77
1. Beam lines, optics and instrumentation	79
1.1 Beam lines	
1.2 Instrumentation	
1.3 Summary of beam lines and optics	90
2. List of apparatus	94
User's short reports	98
1. Content for experimental progress reports	98
2. Experimental progress reports	112
Author index	372
Subject index	376
List of publications	381

PREFACE

The Photon Factory made great strides in 1987. The low-emittance operation of the PF ring was achieved in March and resulted favorably in brilliance increases ranging from 2 to 20 times for all the beam lines with a high beam stability. At the same time, installation of insertion devices is under way for all available straight sections of the ring. A 54-pole wiggler/undulator has been commissioned at BL-16. The devices to be inserted in the near future are a multipole wiggler for BL-13, an undulator for BL-19, and an undulator for circular polarized radiation at BL-28. Construction of beam lines has continued; Four new beam lines, BL-6, BL-9, BL-16, and BL-17, are now in operation. Two beam lines, BL-13 and BL-19 are under construction. Five beam lines are in the design stage; they are BL-3, BL-5, BL-18, and BL-20, and BL-28. Thus, all the 24 beam ports available for use of synchrotron radiation have been occupied. Since its inauguration with the four beam lines in 1982, the Photon factory has grown rapidly and is approaching to the goal to operate the PF ring with positrons in full use of its beam ports and of the straight sections for insertion devices.

The total operation time was limited by the FY1987 budget to 3000 hours, an increase of 200 hours over that of the previous fiscal year. About 80 % of the operating hours were devoted to users experiments. During 1987, 342 of the experiments proposed from many universities and governmental institutes were under way, and participants from industry made 18 experiments with a total of 1577 station-hours.

The joint research programs between KEK and such industrial companies as Fujitsu, Hitachi, Mitsubishi, Nippon Electric Company (NEC), Sanyo, Shin-Nittetsu, Sony and Toshiba were also expanded; 24 programs have run during 1987 involving such subjects as the characterization of semiconductor materials, surface-structure analyses, photochemical reactions, trace impurity analyses, and in-situ observations of crystal growth defects.

Nearly perfect operation of the 400-m-long Linac has continued in 1987 and has supplied both electron and positron beams to the TRISTAN experiments for the world's highest energy (28 GeV) electron and positron collisions as well as the electron beam to the PF experiments. Such a stable and busy operation has been carried out under the leadership of the new director of the Injection Department, Professor G. Horikoshi, who moved from TRISTAN. He has also served as the leader of the research group for development of klystrons.

The light source, the 2.5 GeV electron storage ring, is normally operated with an emittance of 130 nm²rad, and a maximum filling of 300 mA and the life time more than 20 hours have been achieved. The brilliance of the 54-pole wiggler at BL-16 is two orders of magnitude higher than that of the vertical wiggler at BL-14 in the spectral range up to 10 keV. Extensive machine study has revealed the various origins for beam

instabilities and succeeded in suppression of the beam fluctuations to less than 0.1 mm by developing a feedback system. To operate the PF ring with positrons at a sufficiently high current, the accumulation rate will be increased by the end of March 1988.

Many users have enjoyed the highly brilliant light source. By the low-emittance operation, various experiments advanced remarkably in quality; they are structure analyses of surfaces and interfaces, dynamic structure analyses, diffraction experiments with small specimens less than 1 μ m, structure analyses under a high pressure environment, magnetic scattering, and high-resolution EXAFS and photoemission spectroscopy. One of memorable events in 1987 is the extensive study on high T_c superconducting substances such as $YBa_2Cu_3O_{7-x}$ by spectroscopy. The valency of Cu ions and precise band structure have been investigated to understand origins of superconductivity.

These outcomes were presented in the Fifth Annual Photon Factory Symposium which was held with about 270 participants on November 20 and 21, 1987. Oral presentation was made on the activities at BL-1, BL-7, BL-8, and BL-9 which were constructed by industrial companies and the University of Tokyo. Also, 122 poster-session papers were presented.

From their experiences with the PF ring, most of the users are now seeking high-brilliance light sources in the X-ray and VUV spectral ranges. Especially, needs for powerful hard X-ray sources are rapidly increasing. They are for Compton scattering, magnetic scattering, dynamic structure analyses of bio-substances, structure analyses under a high-pressure environment, X-ray-induced chemical reactions, medical diagnostics, etc. Workshops on future plans were often held and ring designs for the next generation have been proposed. Our final goal is to construct 10 GeV low-emittance ring "super PF" which covers the spectral range up to the absorption K-edge of uranium.

To accumulate experience for this purpose, two beam lines with undulators are now being constructed in the experimental hall located in the north-east section of the TRISTAN Accumulation Ring (6 GeV). They will be completed by March of 1989. Furthermore, some designs for use of the TRISTAN Main Ring have been proposed; possibilities of its early use are now discussed extensively.

We would like to acknowledge the cooperation of Mr. Tom Oversluizen from Brookhaven National laboratory, U. S. A. He stayed with us from May to December, 1987. His development of water-cooled monochromators for the new beam line BL-16 with the multipole wiggler was greatly appreciated.

The 3rd International Conference on Synchrotron Radiation Instrumentation, SRI-88, will be held during August 29 to September 2, 1988, at Tsukuba. It will cover new developments of instruments from light sources to detectors.

About 30 invited papers will be presented. Some of them are planned to be chosen from contributed papers. The second circulars are now available from Secretariat for SRI-88, Simul-International

Inc. Kowa Bldg. No. 9, 8-10, Akasaka 1-Chome, Minato-ku, Tokyo, 107. All scientists and engineers concerned with synchrotron radiation around the world are welcome to Tsukuba.

A handwritten signature in black ink that reads "J. Chikawa". The signature is written in a cursive, flowing style.

Jun-ichi Chikawa
Director

Outline of the Photon Factory

Photon Factory 10th Anniversary

— History in pictures —



Construction of the Linac building. (1980)



Linac tunnel before installation (1980)



Construction of the building for the storage ring and experiments. (Oct., 1980)



*Installation of bending magnets.
(Jan., 1982)*



Experimental hall under construction (Apr., 1982)



The meeting of the "working group"
(Nov.1980)



Users preparing for the experiment.
(July.1982)



Photon Factory completion ceremony.(Nov.2.,1982)



First 120 pole undulator before comissioning.
(Feb.,1983)



First Photon Factory Symposium at Tsukuba.
(Nov.4~5.,1983)

History of Photon Factory

- 1971 KEK was established and the construction of a 12-GeV proton synchrotron was started.
The Crystallography Group organized a workshop on "High Power X-ray Generators". A high-energy storage ring was found to be the most powerful. This group requested the cooperation of the High Energy Accelerator Group.
- 1972 The High Energy Accelerator Group of the Institute for Nuclear Study, University of Tokyo, started to design electron accelerators, including X-ray and stretcher rings. During the preliminary design period, the project named the "Photon Factory" (PF) was selected.
- 1973 The PF community was organized.
KEK started to tun the TRISTAN workshop.
- 1974 The Science Council of Japan recommended to the government the establishment of the PF.
- 1975 The PF community requested the cooperation of KEK.
- 1976 The 12-GeV KEK proton synchrotron was commissioned.
- 1977 The Feasibility Study Committee for the PF was organized at KEK.
- 1978 The government approved the PF construction at KEK.
Dr. K. Kohra was appointed as the Chief Director.
- 1979 A ground-breaking ceremony was held in January.
- 1981 The linac produced its first beam with an energy of 0.5 GeV.
The TRISTAN Project was approved at KEK and the construction of the Accumulation Ring (AR) started.
- 1982 In March, the linac energy was increased to 2.5 GeV and the PF ring stored 2.5-GeV electron beams.
In July, experiments using synchrotron radiation were commissioned.
The construction of the electron-postron cillider (30 GeV) of TRISTAN project started.
- 1983 The first undulator with 120 poles was commissioned.
The TRISTAN accumulation ring stored electrons and accelerated them to 6 GeV.
- 1983 A superconducting vertical wiggler was commissioned.
- 1984 Dr. T. Sasaki was appointed as the Chief Director.
- 1985 The first SR channel was installed in the AR.
Dr. J. Chikawa was appointed as the Chief Director.
The positron source was completed. The linac accelerated positrons to 2.5 GeV.
The injection of positrons into both the AR and the PF ring was successful.
- 1986 The SR channel of the AR was commissioned.
The scientific cases for the next generation storage ring were discussed.
- 1987 In February, the PF ring started its operation in the low emittance mode.
A PF multipole wiggler/undulator with 26 periods was commissioned.

OUTLINE OF THE PHOTON FACTORY

1. INTRODUCTION

The Photon Factory (PF) is a national synchrotron radiation (SR) research facility affiliated with the National Laboratory for High Energy Physics, or KEK, supervised by the Ministry of Education, Science and Culture. It consists of a 2.5-GeV electron linear accelerator, 2.5-GeV electron storage ring as a dedicated light source, and beam-lines and experimental stations for exploiting synchrotron radiation, in studies involving such fields as physics, chemistry, biology, medical science, pharmacology, geology and lithography. All of the facilities for synchrotron radiation research are open to scientists from universities and research institutes belonging to the government, public organizations, private enterprises and those of foreign countries. Institutions affiliated with the Ministry of Education, Science and Culture are given the highest priority as users. Applications from other organizations are also admitted with or without charge, depending upon the categories of their objectives.

The Photon Factory is located at the northern most end of Tsukuba Science City, about 60 km north-east of Tokyo.

2. HISTORY

On the occasion of coming of the tenth anniversary of the PF foundation and the sixth anniversary of successful operation of the PF ring for the SR experiments, the history of PF is to be briefly summarized.

The PF was founded on April 1st, 1978 at the KEK. The PF project was approved as a four-year construction program and the total cost of the construction was 18.5 BY not including staff salaries.

On January 25th, 1979, the ground breaking ceremony was held, and the construction of the Linac tunnel began. The trial operation of the first sector of the Linac was done and accelerated electrons of 500 MeV with a beam current of 50 mA were obtained in July, 1981. The Ring tunnel and experimental hall, construction was completed in March, 1980. In January, 1982, the construction of the Linac was completed, and beam acceleration was started. In February, 1982, electron beams were injected into the Ring. On March 11th, 1982, 224 hours after the first injection, the energy of the Linac and the Ring reached at 2.5 GeV with a ring current of 6.5 mA. The PF facility was commissioned on the first day of June, 1982. Half of the total ring operation time of 1300 hours in FY 1982 was used for machine improvement and the other half was for adjustments of the experimental apparatus and for the preliminary experiments using SR. The experiments approved by the Program Advisory Committee started from FY 1983. At that time, the average beam current during user's time was more than 100 mA. During the 6 year operation of the PF, many improvements and developments were achieved both for the Linac, the Ring and the experimental apparatus, and were reported in the former volumes of the Photon Factory Activity Report.

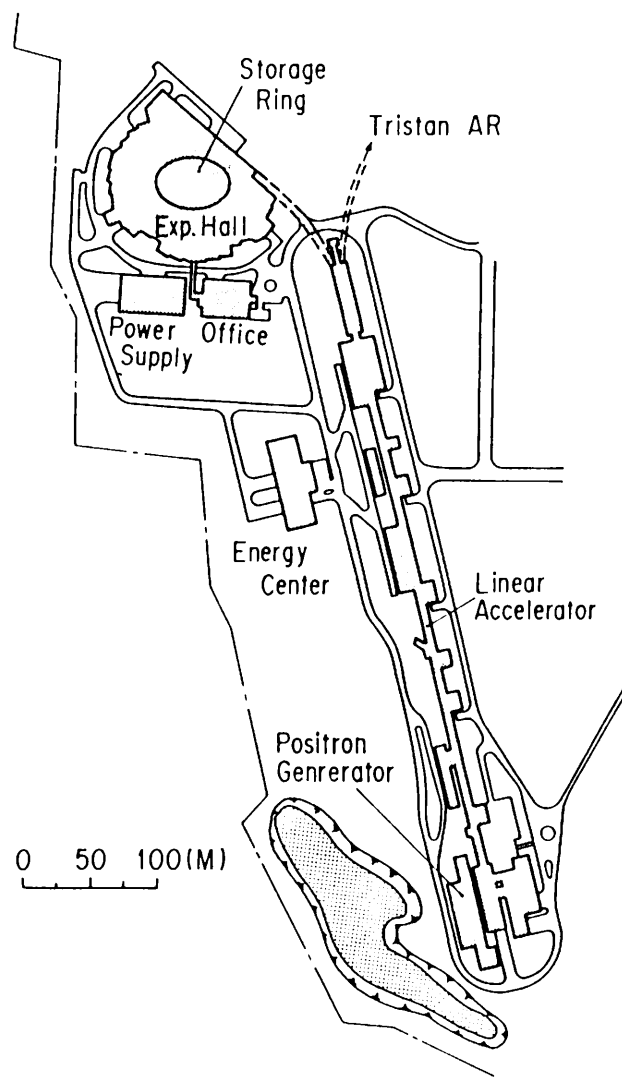


Fig. 1 Plan of the Photon Factory.

Table 1 Yearly account of beam channels

Period	Number of Beam Channels			Total
	PF	Institute	Industry	
FY1981	6	0	0	6
FY1982	8	0	0	8
FY1983	8	0	1	9
FY1984	8	1	2	11
FY1985	10	1	4	15
FY1986	12	1	4	17
FY1987	13	3	4	20

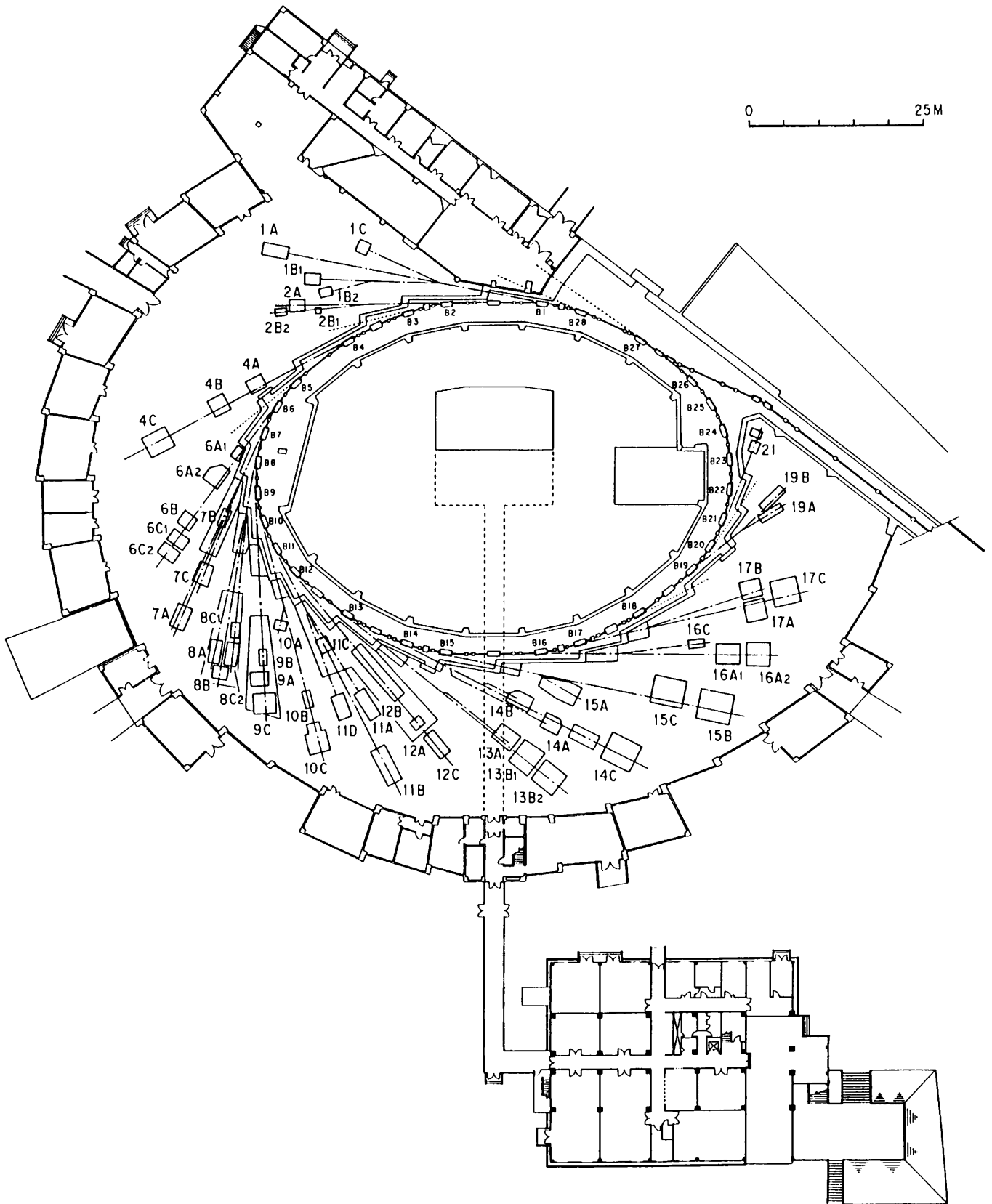


Fig. 2 Diagram of the experimental hall and the storage ring.

Table 2 Experimental stations of the Photon Factory

* under construction

BL-1 (NTT)	11C	VUV spectroscopy (solid state) (1 m Seya-Namioka)
1A Solid surface analyses	11D	Angle-resolved photoelectron spectroscopy (Constant Deviation)
1B X-ray lithography		
1C Photo-chemical reaction		
BL-2 Undulator	BL-12	
2A Soft X-ray high resolution experiment	12A	VUV spectroscopy (gas) (1 m Seya-Namioka)
2B Fresnel zone plate Soft X-ray spectroscopy (10 m Grazing incidence)	12B	VUV high resolution absorption spectroscopy (6 VOPE)
	12C	Photo-chemical reaction
BL-4	BL-13*	Multipole wiggler (National Research Institute)
4A Dispersive EXAFS Trace element analysis Radiation effects on living cells	13A	Accurate lattice parameter measurement
4B Liquid/melt structure analysis Powder diffraction	13B1	Surface analysis
4C X-ray diffuse scattering Fluorescent EXAFS	13B2	X-ray diffraction at high pressures
BL-6	BL-14	Vertical wiggler
6A1 Ultra small angle X-ray scattering	14A	Crystal structure analysis of proteins EXAFS at high photon energy
6A2 Macromolecular crystallography by Weissenberg camera	14B	High precision X-ray optics
6B X-ray spectroscopy and diffraction	14C	High speed X-ray topography X-ray radiography X-ray magnetic scattering Compton scattering
6C1 X-ray diffraction at low temperatures		
6C2 Accurate lattice parameter measurement	BL-15	
BL-7 (University of Tokyo)	15A	Small-angle X-ray scattering of muscle and alloys
7A Soft X-ray photoemission spectroscopy	15B	X-ray topography X-ray interferometry
7B Surface photo-chemical reaction	15C	High resolution X-ray diffraction
7C X-ray spectroscopy and diffraction (PF)		
BL-8 (Hitachi)	BL-16	Multipole wiggler/Undulator
8A Soft X-ray spectroscopy	16A	Hard X-ray experiment
8B EXAFS	16B	VUV experiment
8C1 X-ray lithography		
8C2 X-ray tomography	BL-17	(Fujitsu)
BL-9 (NEC)	17A*	Characterization of crystals
9A X-ray lithography	17B*	EXAFS
9B* Photo-chemical vapor deposition	17C	X-ray lithography
9C EXAFS and X-ray topography/diffraction	BL-19*	(University of Tokyo)
BL-10	19A	Spin-polarized photoelectron spectroscopy
10A Crystal structure analysis of minerals	19B	Photoelectron spectroscopy at variable temperatures
10B EXAFS		
10C Small-angle X-ray scattering of enzymes Surface diffraction	BL-21	(Light source department) Beam position monitor
BL-11		
11A Soft X-ray spectroscopy (2 m Grasshopper)		
11B Surface EXAFS Soft X-ray standing wave method		

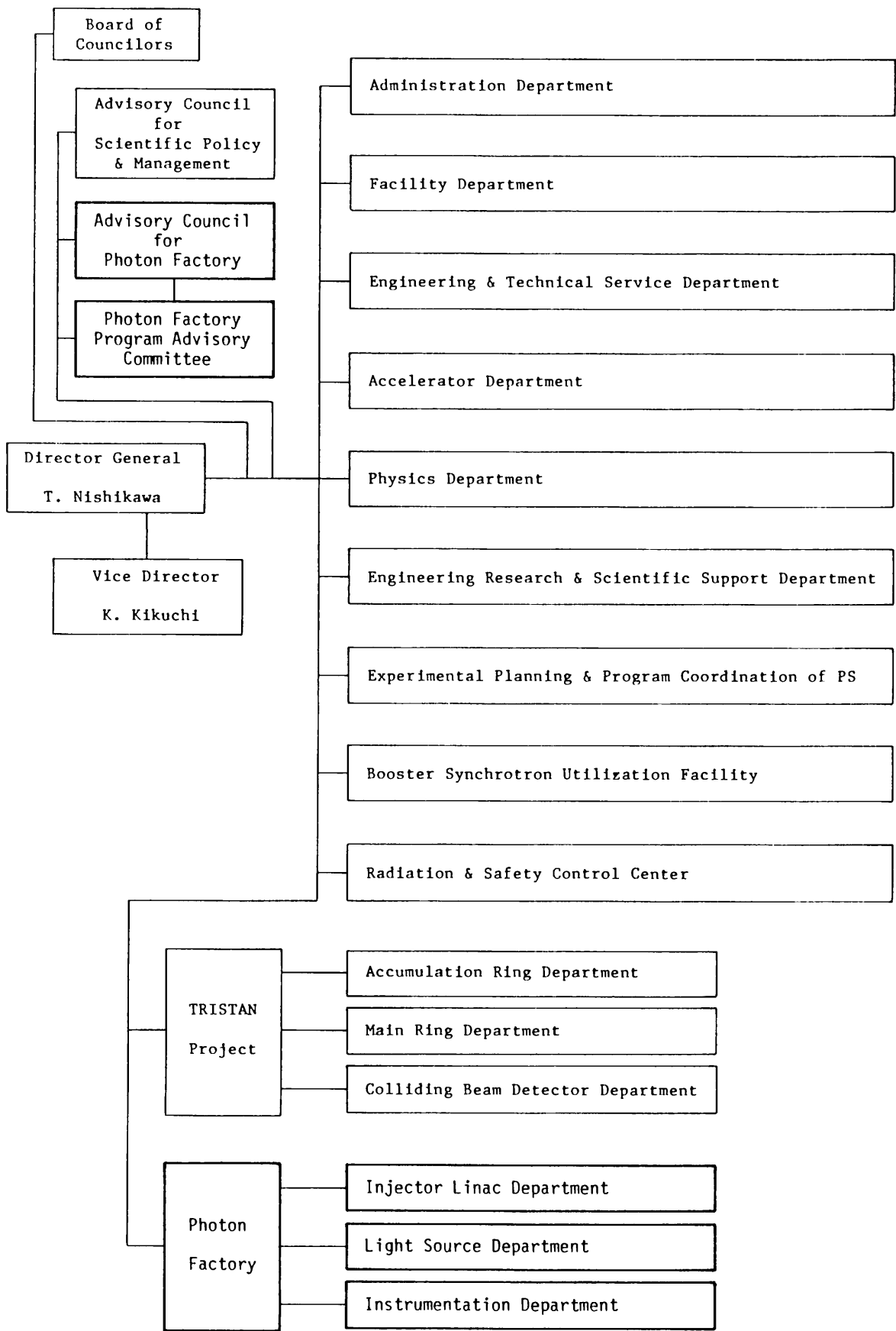


Fig. 3 Organization of KEK

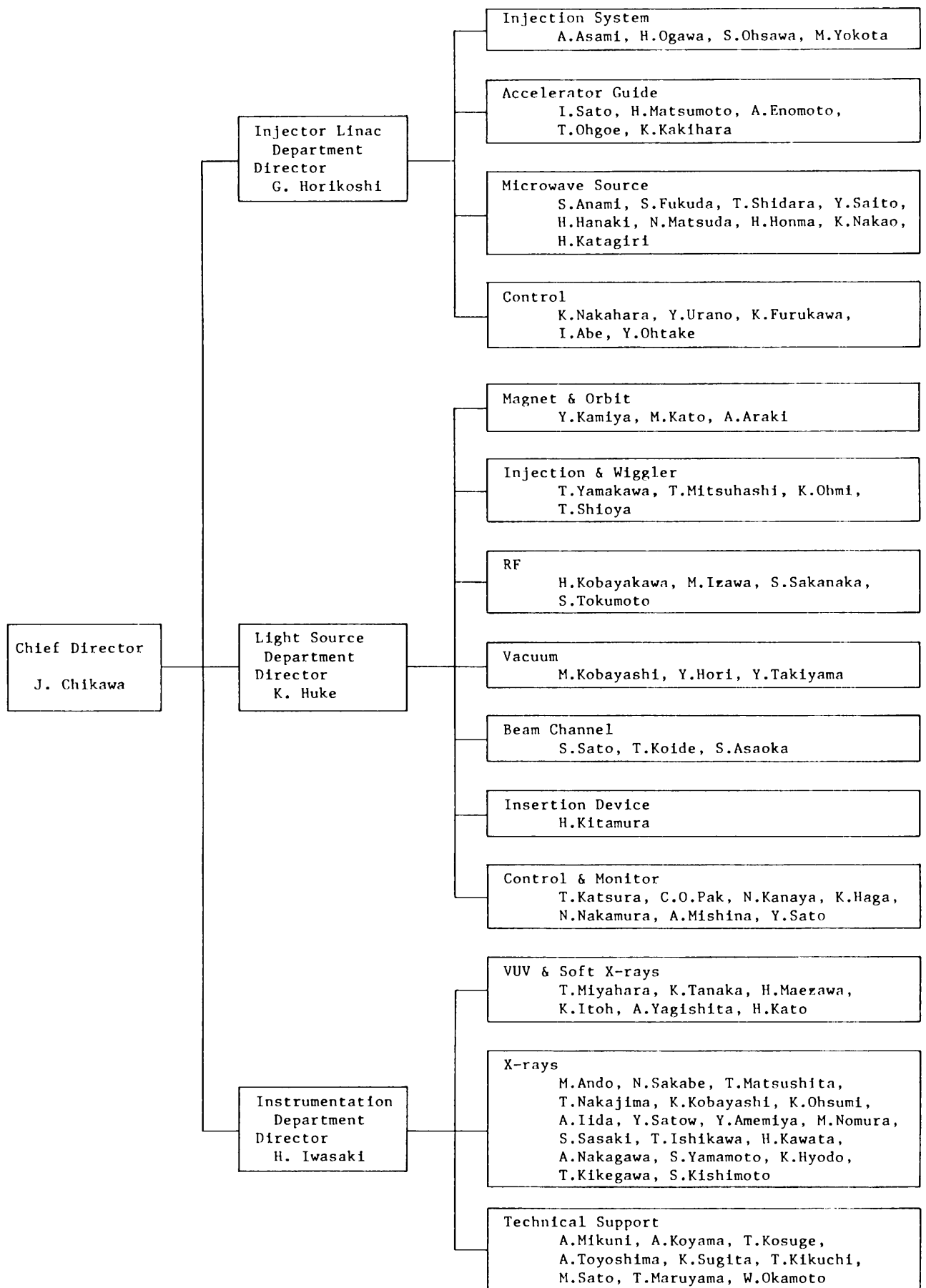


Fig. 4 Organization and Members of Photon Factory

3. PLAN OF THE FACILITY

A plan which includes the accelerator complex is shown in Fig. 1. A long housing for the 450-m linear accelerator is connected to the storage ring building through a 150-m underground beam-transport tunnel. A view of the experimental hall is shown in Fig. 2, including the magnet arrangement of the ring. The yearly increases in the number of beam channels from the beginning of the PF are listed in Table 1. Table 2 shows the status of beam channels and experimental stations.

Beam lines BL1, BL8, BL9 and BL17 were constructed by Nippon Telephone and Telegram (NTT), Hitachi Corporation, Nippon Electric Company (NEC) and Fujitsu Corporation LABS, respectively, in collaboration with KEK. BL7A and BL7B were built by the Research Center for Spectrochemistry (RCS), the University of Tokyo. BL13 (the Science and Technology Agency) and BL19 (the Institute for Solid State Physics, the University of Tokyo) are now under construction in collaboration with KEK. The other beam lines were constructed by the PF's own funding.

4. ORGANIZATION AND STAFF

The organizational structure of KEK is shown in Fig. 3. The PF consists of three departments: Injector Linac, Light Source and Instrumentation. Details concerning the organizational structure

and the staff of the PF are shown in Fig. 4. Also, the number of staff and visiting scientists from the beginning of the PF are listed in Table 3.

The Advisory Council for the PF was established to discuss scientific programs and management of the PF. This council consists of twenty-one persons of learning and experience; ten members are from outside KEK (Table 4). The term of membership is two years.

The Advisory Council has its own Program Advisory Committee (PAC) for examining experimental proposals with respect to their scientific aspects and technical feasibilities. The PAC (Fig.3) includes the directors of the three departments and twelve or less persons of learning and experience from outside KEK (Table 5). The term of the membership is also two years; half of the outside members are changed every year.

5. BUDGET

The budgets of the Photon Factory during the construction period and after commissioning of the PF facility are shown in Table 6 and 7 respectively. Financial support for the PF is obtained from the government. During FY1987, 27 % of the budget will pay for the construction of the SR beam channel at the accumulation ring and the novel insertion devices.

Table 3 Annual number of staff & visiting scientists

Position	Division	1978	1979	1980	1981	1982	1983	1984	1985	1986	1987
Chief Director		1	1	1	1	1	1	1	1	1	1
Professor	Injector Linac	1	2	3	3	3	3	3	3	4	4
	Light Source	1	4	4	4	4	4	4	3	4	4
	Instrumentation	0	0	0	1	1	1	1	2	3	4
Associate Professor	Injector Linac	0	1	1	1	2	2	2	2	1	2
	Light Source	1	5	4	4	4	3	5	5	3	3
	Instrumentation	0	0	1	3	4	5	5	8	7	9
Research Associate	Injector Linac	1	3	4	6	7	8	9	10	11	10
	Light Source	0	1	4	6	7	7	6	8	9	12
	Instrumentation	0	0	3	2	7	10	10	10	13	13
Technical Staff	Injector Linac	0	0	2	4	5	5	6	6	7	8
	Light Source	3	3	3	4	6	6	6	6	7	7
	Instrumentation	0	0	0	0	1	2	4	4	8	9
Visiting Scientist	Injector Linac	2	2	2	2	2	2	2	2	2	2
	Light Source	2	6	4	4	4	4	4	4	4	4
	Instrumentation	0	0	6	6	6	6	6	6	6	6
Total		12	28	42	51	64	69	74	80	90	97

6. OPERATION TIME AND PROPOSAL

There are three machine operation terms scheduled for 1987 (Table 8). The operation times of each term are summarized in Table 9.

Fig. 5 shows the annual ring operation time of the PF. This figure suggests that the ring operation time has increased remarkably; also, the percentage of user time in the ring operation time has become larger. This means that the efficiency of ring usage has been improving.

About 25 % of the operation time is used for machine studies. Such studies are effective for the improvement of stability, long life time, low emittance configuration, positron accumulation and so on.

There are three routes for use of the PF beam lines. Scientists from universities and their research institutes and research institutes belonging to the government or a public organization can use the beam lines without charge if their proposals are accepted by the PAC. The

deadlines for the applications are January 14th and July 14th every year. We call such accepted scientists "general users" and each subject is effective through two years. The number of proposals approved by the PAC since commissions the PF is listed in Table 10.

The second type is for scientists of private enterprises; these users are charged. Category A is for cooperative experiments with the PF staff; this type must be authorized by the Japanese government if the government supports less than a half of experimental expenses (depending upon the objectives). The deadline for an application is usually January. Category B is for private experiments; proposals can be accepted at any time by the Advisory Council of the PF. The number of the proposals belonging to the above two categories is also listed in Table 11. Last of all, category C is for cooperative experiments with the PF staff; all experimental expenses must be paid by the private enterprises.

Table 4 Members of advisory council

* : Chairman
** : Vice-Chairman

Prof. ANDO, Masami	PF Instrumentation Department, KEK.
Prof. ASAMI, Akira	PF Injector Linac Department, KEK.
Prof. HORIKOSHI, Gen-ichi	Director of PF Injector Linac Department, KEK.
Prof. HUKU, Kazuo*	Director of PF Light Source Department, KEK.
Prof. IIJIMA, Takao	Faculty of Science, Gakushuin University.
Prof. IITAKA, Yoichi	Faculty of Pharmaceutical Sciences, University of Tokyo.
Prof. ISHII, Takehiko	Institute for Solid State Physics, University of Tokyo.
Prof. ITOH, Takashi	College of Arts & Science, University of Tokyo.
Prof. IWASAKI, Hiroshi	Director of PF Instrumentation Department, KEK.
Prof. KASUYA, Tadao	Faculty of Science, Tohoku University
Prof. KOBAYAKAWA, Hisashi	PF Light Source Department, KEK.
Prof. KOMURA, Yukitomo	Faculty of Science, Hiroshima University.
Prof. KURODA, Haruo**	Faculty of Science, University of Tokyo.
Prof. MITSUI, Toshio	Faculty of Engineering Science, Osaka University.
Prof. NAKAHARA, Kazuo	PF Injector Linac Department, KEK.
Prof. SAKABE, Noriyoshi	PF Instrumentation Department, KEK.
Prof. SATO, Isamu	PF Injector Linac Department, KEK.
Prof. SATO, Shigeru	PF Light Source Department, KEK.
Prof. TOKONAMI, Masayasu	Faculty of Science, University of Tokyo.
Prof. UNO, Ryosei	College of Humanities & Sciences, Nihon University,
Prof. YAMAKAWA, Tatsuya	PF Light Source Department, KEK.

Table 5 Members of Program Advisory Committee

* : Chairman

Prof. AKISADA, Masayoshi	Institute of Clinical Medicine, University of Tsukuba.
Prof. GOHSHI, Yohichi	Department of Industrial Chemistry, University of Tokyo.
Prof. HARADA, Jimpei	Department of Applied Physics, Nagoya University.
Prof. HORIKOSHI, Gen-ichi	Director of PF Injector Linac Department, KEK.
Prof. HUKU, Kazuo	Director of PF Light Source Department, KEK.
Prof. IITAKA, Yoichi	Faculty of Pharmaceutical Sciences, University of Tokyo.
Prof. IWASAKI, Hiroshi*	Director of PF Instrumentation Department, KEK.
Prof. KOTANI, Akio	Faculty of Science, Tohoku University.
Prof. KURODA, Haruo	Faculty of Science, University of Tokyo.
Prof. MITSUI, Toshio	Faculty of Engineering Science, Osaka University.
Prof. MOURI, Nobuo	Institute for Solid State Physics, University of Tokyo.
Prof. MURATA, Yoshitada	Institute for Solid State Physics, University of Tokyo.
Prof. OHTA, Toshiaki	Faculty of Science, Hiroshima University.
Prof. SUZUKI, Hiroshi	Faculty of Science and Technology, Sophia University.
Prof. TOKONAMI, Masayasu	Faculty of Science, University of Tokyo.

Table 6 Construction budget (in million yen)

Items	1978	1979	1980	1981	1982
Salary	10	82	179	269	
Injector Linac	245	815	1,456	1,152	
Storage Ring	259	582	792	754	
Instrumentation	30	73	379	822	977
Civil Engineering	868	2,546	4,561	2,529	
Accelerator Operation	0	7	60	177	
Computer Rentals	0	0	34	135	
Cooling Systems & Electric Plant Operation	0	0	0	60	
Electricity	0	1	26	52	
Miscellaneous	29	95	154	223	126
Total	1,441	4,201	7,641	6,173	1,103

Table 7 PF-Budget in each fiscal year

(in million yen)

Items	1982	1983	1984	1985	1986	1987
Salary	402	474	484	491	510	561
Storage Ring (channel, insertion device, etc)	0	0	0	153	131	1,045
PF Experiments	140	153	134	184	190	196
PF Operation & Maintenance	412	477	552	653	820	907
Computer Rentals	136	135	135	135	136	136
Positron Source Operation & Maintenance	0	0	0	41	138	208
Cooling Systems & Electric Plant Operation	120	111	124	180	211	214
Electricity	209	226	257	338	381	331
PF-Industrial Cooperative Experiments	0	94	84	95	185	166
Miscellaneous	115	134	115	127	162	120
Total	1,534	1,804	1,885	2,397	2,864	3,884

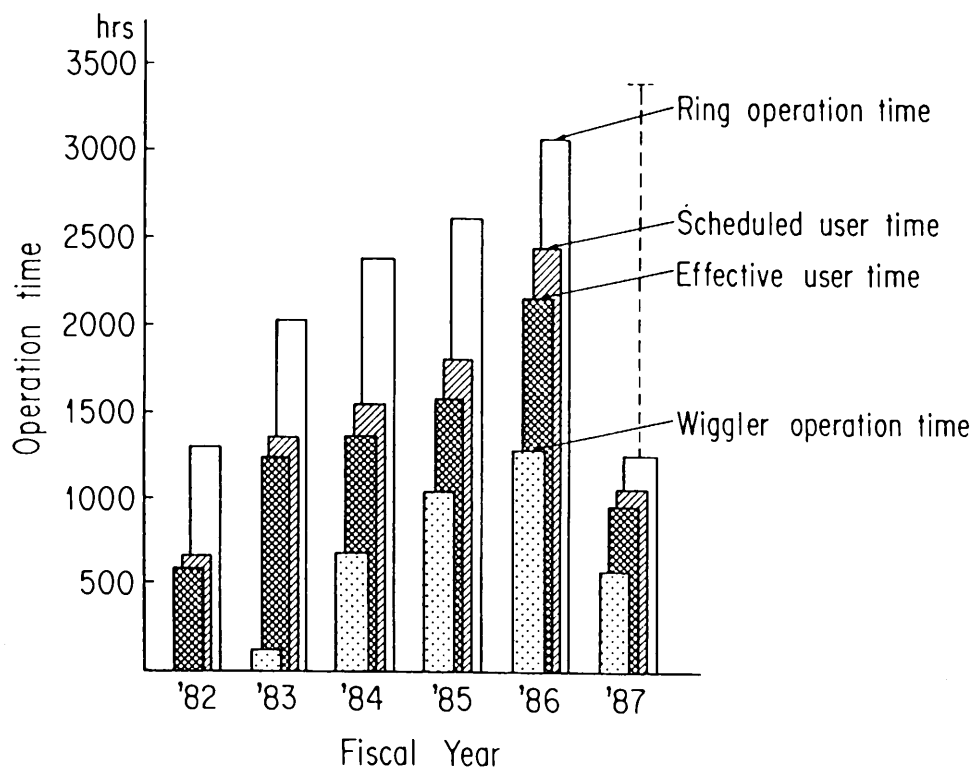


Fig. 5 Ring operation statistics (from the first operation of the PF).

Table 8 Operation schedule in FY 1987

M: Machine study R: PF Ring L: Linac A: Accumulation Ring
 T: Tuning
 U: User's beam time
 The number shown in each column is the number of shifts (8 hours/shift).

Cycle	M	Tu	W	Th	F	Sa	Su	M	Tu	W	Th	F	Sa	Su	M	Tu	W	Th	F	Sa	Su	M	Tu
1-0 1-1	5/4	5	6	7	8	9	10	11	12	13	14	15	16	17	18	19	20	21	22	23	24		
			T (L) 2	T (R) 2	T (A) 2					T (R/A) 1 2			U 12		M (R) 3		U 9		M (L) 3				
1-2	5/25	26	27	28	29	30	31	6/1	2	3	4	5	6	7	8	9	10	11	12	13	14	15	
			T (R/A) 1 2		U 12			M (R) 3	M (L) 3			U 27					U 9		M (R/L) 3		U 6		
1-3	6/22	23	24	25	26	27	28	29	30	7/1	2	3	4	5	6								
			T (L/R) 1 2		U 15			M (R) 3	M (L) 3		U 9			L/AR									
1-4	7/6	7	8	9	10	11	12	13	14	15	16	17	18	19	20	21	22	23	24	25	26		
		T (L/R) 1 2		U 18				M (R) 3		U 12				L/AR		M (L) 3							
2-0	9/28	29	30	10/1	2	3	4	5	6	7	8	9	10	11									
		T (L) 5		T (A) 6				T 1	T (A) 5	T (R) 4	T (A) 6												
2-1	10/12	13	14	15	16	17	18	19	20	21	22	23	24	25	26	27	28	29	30	31			
			T 1	M (R) 5	M (R/L) 6	U 6		M (R) 3	M (L) 3			U 27							M (R/L) 1 1 1	M (R/L) 1 1 1			
2-2	11/2	3	4	5	6	7	8	9	10	11	12	13	14	15	16	17	18	19					
			T (R/A) 1 2		U 12			M (R) 3	M (L) 3		U 9			L/AR		M (L) 3							
2-3	11/23	24	25	26	27	28	29	30	12/1	2	3	4	5	6									
			T (R/A) 1 2		U 12			M (R) 3	M (L) 3		U 9												
2-4	12/7	8	9	10	11	12	13	14	15	16	17	18	19	20	21	22	23						
		T (R/A) 1 2		U 18				M (R) 3		U 21						M (L) 3							
3-0 3-1	1/11	12	13	14	15	16	17	18	19	20	21	22	23	24	25	26	27	28	29	30	31	2/1	2/2
			T (L) 3	T (R) 3	T (L) 3	T (A) 3	L/AR 3	T (R/A) 1 2		U 18					M (R) 3	M (L) 3		U 15				L/AR 6	
3-2	2/8	9	10	11	12	13	14	15	16	17	18	19	20	21	22	23	24	25	26	27	28	29	
		M (R/A) 1 2		U 15				M (R) 3	M (L) 3				U 27						M (R/L) 1 1 1	M (R/L) 1 1 1	L/A 6		
3-3	3/1	2	3	4	5	6	7	8	9	10	11	12	13	14	15	16							
			M (R/A) 1 2		U 9			M (R) 3		U 9		M (L) 3		L/A 12									

Table 9 Summary of operation schedule

Cycle	Linac (h)	PF Ring (h)	User's time (h)
1	1415	1263	952
2	1656	1336	912
3	1320	1192	744
Total	4391	3791	2608

Table 10 Number of proposals by general users since the beginning of the PF

Research Field	Period*	1983	1983	1984	1984	1985	1985	1986	1986	1987	1987	Total
		I	II	I	II	I	II	I	II	I	II	
EXAFS		25	17	16	10	22	13	21	19	31	30	204
X-Ray (Biology)		10	8	11	7	22	6	18	10	25	7	124
X-Ray (Material Sciences)		19	5	8	21	62	13	29	25	49	24	255
Soft X-Ray & VUV		13	6	2	10	12	15	7	19	14	14	112
Total		67	36	37	48	118	47	75	73	119	75	695

* I and II indicate periods when proposals were accepted by the Program Advisory Council (PAC) in March and in September, respectively.

Table 11 Charged beam time used by industries since the beginning of PF

		1983	1984	1985	1986	1987
General Industries	No. of Industries	11	12	11	7	5
	No. of Proposals	20	35	21	10	7
	Beam Time Used (h)	467	905	814	326	194
	Ratio* (h)	42	75	74	46	38
Industries Which Have Their Own Beam Lines	No. of Industries	1	1	3	4	4
	No. of Proposals	1	1	3	4	7
	Beam Time Used (h)	219	217	424	1211	1355
	Ratio* (h)	291	217	141	302	338
Total	No. of Industries	12	13	14	11	9
	No. of Proposals	21	36	24	14	14
	Beam Time Used (h)	686	1122	1238	1537	1549
	Ratio* (h)	57	86	88	139	172

Ratio* Beam Time Used / No. of Industries

7. LIST OF PROPOSALS

7.1 Proposals accepted by Program Advisory Committee

<u>Proposal Number</u>	<u>Spokesperson</u>	<u>Title</u>
87-001	T. Yokokawa Faculty of Science, Hokkaido Univ.	EXAFS Investigation about the Role and the Structure of Tl Ion in $Tl_2O-B_2O_3$ Glass
87-002	M. Ichikawa Research Institute for Catalysis, Hokkaido Univ.	Characterization of Supported Rh-Fe and Pt-Fe Bimetallic Clusters and Their Catalytic Functions
87-003	T. Nasu Faculty of Education, Yamagata Univ.	EXAFS Study on Deformation Inducing Local Structure Change of Cu-Zr Amorphous Alloys
87-004	Y. Shono Research Institute for Iron, Steel & Other Metals, Tohoku Univ.	Local Structure of High Pressure Phases of Vanadium Oxides
87-005	K. Suzuki Research Institute for Iron, Steel & Other Metals, Tohoku Univ.	Structural Analysis of Bi-Zn-Fe-O Amorphous Films by Fluorescence EXAFS
87-006	F. Ito Research Institute for Iron, Steel & Other Metals, Tohoku Univ.	A Study of Amorphous NiZr Hydrides by EXAFS and XANES
87-007	S. Sueno Institute of Geoscience, Univ. of Tsukuba	EXAFS and XANES Experiment under High Pressure and High Temperature Using Diamond Anvil Cell
87-008	T. Kawashima Dept. of Chemistry, Univ. of Tsukuba	EXAFS and XANES Analysis of Reaction Products of Selenium (IV) with Organic Reagents
87-009	S. Nakano Faculty of Science, Chiba Univ.	On the Possibility of Metal-insulator Transition in Metallic Nb Films
87-010	H. Kuroda Faculty of Science, Univ. of Tokyo	Morphology Changes in Ultra Fine Particles of Supported Metals by the Metal Additives and Their Catalysis
87-011	Y. Iwasawa Faculty of Science, Univ. of Tokyo	Dynamic of Supported Rh Dimer Carbene Complex Catalyst under Reaction Condition
87-012	Y. Iwasawa Faculty of Science, Univ. of Tokyo	EXAFS Studies on the Structures of TiO_2 and V_2O_5 Super Thin Layer Catalysts
87-013	Y. Iwasawa Faculty of Science, Univ. of Tokyo	EXAFS Study on the Structures of Supported Selenium Catalysts
87-014	Y. Iwasawa Faculty of Science, Univ. of Tokyo	EXAFS Studies on the Structure of Zeolite-supported $Mo(CO)_6$ Catalysts
87-015	K. Asakura Faculty of Science, Univ. of Tokyo	EXAFS Studies on the Structure of Rare Earth Metal Oxide Super Thin Layer Catalysts

-
1. Ministry of International Trade & Industry
 2. Science & Technology Agency
 3. Ministry of Agriculture, Forestry & Fisheries

87-016	N. Toshima Faculty of Science, Univ. of Tokyo	Studies on the Structure of Bimetallic Colloidal Catalysts
87-017	K. Shibata Faculty of Engineering, Univ. of Tokyo	Study on Effect of Alloying Elements in Iron Measured by EXAFS
87-018	S. Emura Institute of Scientific and Industrial Research, Osaka Univ.	Interface Structure of Ultra Thin Superlattices on (AlAs) _m (InAs) _n and (GaAs) _m (InAs) _n
87-019	N. Esaki Institute for Chemical Research, Kyoto Univ.	Structure and Reaction Mechanism of Glutathione Peroxidase
87-020	M. Okuno Faculty of Science, Kanazawa Univ.	EXAFS Studies of Ag ₃ AsS ₃ -Ag ₃ SbS ₃ and Ag ₃ AsS ₃ -Ag ₃ AsSe ₃ Crystals and Glasses
87-021	H. Sakurai Faculty of Pharmaceutical Science, Tokushima Univ.	EXAFS Studies on Gold in Animal Organs Treated with Auranofin
87-022	Y. Kidani Faculty of Pharmaceutical Science, Nagoya City Univ.	Interaction of Zinc Ions with Carboxypeptidase A
87-023	T. Yamaguchi Faculty of Science, Fukuoka Univ.	EXAFS and XANES Study of Metal Complexes in Rapidly Frozen Solutions
87-024	A. Nishijima National Chemical Laboratory for Industry ¹	EXAFS Studies on Local Structures of Active Sites on Mo Supported Catalysts for Hydrocracking and Hydrogenation Activities
87-025	J.B. Parise Sydney Univ. Australia	An EXAFS Study of Crystallizing Gels
87-026	Hua Zhong-yi Fudan Univ. China	The EXAFS and SEXAFS Analysis of Amorphous Alloys
87-027	T. Matsushita Photon Factory, National Laboratory for High Energy Physics	Stopped Flow X-Ray Absorption Spectroscopy in Dispersive Mode
87-028	N. Sakabe Photon Factory, National Laboratory for High Energy Physics	Crystallographic Studies of Molecular Biology by Film Methods
87-029	N. Sakabe Photon Factory, National Laboratory for High Energy Physics	Intensity Data Collection of DPI Using Weissenberg Camera
87-030	H.A. Yonath MPG for Structural Molecular Biology, Israel	Crystal Structure Analysis of Ribosomal Particles from Bacterial Sources
87-031	T. Ueki Faculty of Engineering Science, Osaka Univ.	Improvement of "SAXES" and Development of Data Treatment Software
87-032	T. Ueki Faculty of Engineering Science, Osaka Univ.	Structural Analysis of Oligomeric Proteins in Solutions

87-033	T. Ueki Faculty of Engineering Science, Osaka Univ.	Structural Behavior of Troponin-c upon Ca^{++} Ions Binding
87-035	Y. Mitsui Faculty of Pharmaceutical Sciences, Univ. of Tokyo	X-Ray Crystal Structure Analyses of Calmodulin-ligand Complexes
87-036	F. Tokunaga Faculty of Science, Tohoku Univ.	Study on Photointermediate M by Low Temperature X-Ray Diffraction under Illumination
87-037	I. Matsubara Tohoku Univ. School of Medicine	Fast X-Ray Diffraction of Perfused Heart Muscle
87-038	N. Yagi Tohoku Univ. School of Medicine	Structural Changes in the Thin Filament Induced by Calcium Ions
87-039	I. Hatta Faculty of Engineering, Nagoya Univ.	Studies on Phase Transition in Phospholipids- Cholesterol Bilayers by X-Ray Diffraction
87-040	T. Hamanaka Faculty of Engineering Science, Osaka Univ.	Structural Studies of Visual Cell Membrane by X-Ray Diffraction
87-041	K. Wakabayashi Faculty of Engineering Science, Osaka Univ.	Fast X-Ray Diffraction Studies on Structural Changes of the Actin Containing Filament during Muscle Contraction
87-042	T. Yamada National Institute of Radiological Science ²	Analysis of the Initial Events Leading to Radiation Carcinogenesis by Monochromatic Synchrotron Radiation
87-043	Y. Saeki Dept. of Physiology, Faculty of Dentistry, Tsurumi Univ.	X-Ray Diffraction of Skinned Heart Muscle
87-044	H. Sugi School of Medicine, Teikyo Univ.	Dynamic X-Ray Diffraction Studies on the Molecular Mechanism of Contraction in Striated Muscle
87-045	K. Horiuti Jikei Univ. School of Medicine	X-Ray Diffraction of Skeletal Muscle under the Inhibitory Action of 2,3-butanedione-2-monoxime
87-046	S. Hasegawa Department of Electronics, Univ. of Electronics-Communication	Development of Imaging System for Medical Diagnosis Using PF
87-047	F. Toyofuku Department of Dental Radiology, Kyushu Univ.	An Application of the SR Excited Characteristic X-Rays to Dichromography
87-048	Y. Sugishita Institute of Clinical Medicine, Univ. of Tsukuba	Fundamental Studies on K-edge Subtraction for Medical Application of Synchrotron Radiation
87-049	I. Anno Institute of Clinical Medicine, Univ. of Tsukuba	SR Diagnosis of Lymphography and Soft Tissue Tumors
87-050	M. Ando Photon Factory, National Laboratory for High Energy Physics	Development of X-Ray Monochromator System for Clinical Application of Synchrotron Radiation

87-051	K. Kobayashi Photon Factory, National Laboratory for High Energy Physics	Development of the Evaluating Methods for the Absorbed Dose in the Body of Monochromatic X-Rays
87-052	K. Hyodo Photon Factory, National Laboratory for High Energy Physics	Fundamental Studies on Energy Subtraction for Medical Application
87-053	A. Iida Photon Factory, National Laboratory for High Energy Physics	Chemical Speciation by SR Excited X-Ray Fluorescence Using Chemical Shift of Absorption Edge
87-054	A. Iida Photon Factory, National Laboratory for High Energy Physics	Trace Element Analysis by Wavelength Dispersive X-Ray Fluorescence
87-055	A. Iida Photon Factory, National Laboratory for High Energy Physics	Quantitative Analysis by SR Excited X-Ray Fluorescence
87-056	I. Nakai Dept. of Chemistry, Univ. of Tsukuba	Nondestructive X-Ray Fluorescence and Absorption Spectroscopic Imaging of Archaeological and Geological Samples
87-057	Y. Gohshi Faculty of Engineering, Univ. of Tokyo	X-Ray Fluorescence of Hair Analysis by SR Micro-beam
87-058	Y. Gohshi Faculty of Engineering, Univ. of Tokyo	SR Micro Beam X-Ray Analysis
87-059	K. Ohsumi Photon Factory, National Laboratory for High Energy Physics	Development of the System for Micro-crystal Structure Analysis
87-060	M. Ohmasa Institute of Materials Science, Univ. of Tsukuba	Studies on Structures of Very Fine Sialon Crystals
87-061	R. Uno College of Humanities and Science, Nihon Univ.	Analysis of Orientational Distribution of Powder in Powder Diffractometry Using Synchrotron Radiation
87-062	T. Yamanaka Faculty of Science, Univ. of Tokyo	Structure Analysis of Powder Samples by Energy and Angular Dispersion
87-063	A. Nukui National Institute for Research in Inorganic Materials ²	Study on Amorphous Materials by RDF Employing Anomalous Dispersion Effect; Especially for Chalcogenide Glass
87-064	H. Nasu Faculty of Engineering, Hiroshima Univ.	Temperature Dependence of RDF of Glass-forming Halide or Chalcogenide Melts
87-065	H. Oyanagi Electrotechnical Laboratory ¹	Development of Fluorescence EXAFS Techniques for Surface, Interface and Dilute Systems
87-066	Y. Udagawa Institute for Molecular Science	A Study of X-Ray Raman Scattering

87-067	K. Kashiwase College of General Education, Nagoya Univ.	Diffraction of Thermally Scattered X-Ray Waves in Crystal II
87-068	S. W. Wilkins CSIRO, Division of Chemical Physics, Australia	High-resolution Triple-crystal Studies of Ion-implanted Silicon and Other Samples
87-069	T. Matsushita Photon Factory, National Laboratory for High Energy Physics	Study of Two Dimensional Structure of Langmuir and Langmuir-Blodgett Films
87-070	T. Mukoyama Institute for Chemical Research, Kyoto univ.	One-photon Multi-electron Excitation Process in X-Ray Absorption Spectra
87-071	T. Fukamachi Saitama Institute of Technology	A Study of Intensity Anomaly near Absorption Edge Caused by X-Ray Resonant Scattering
87-072	B. Okai National Institute for Research in Inorganic Materials ²	Measurement of Forerunners Prior to Phase Transition
87-073	K. Ohsumi Photon Factory, National Laboratory for High Energy Physics	Determination of Site Occupancies (Bi/Pb) of Bi/Pb Sulfide Minerals
87-074	K. Ohshima Institute of Applied Physics, Univ. of Tsukuba	Study on the Local Atomic Arrangement in the Noble Metal Based Alloys Containing 3d Transition Metals
87-075	M. Kimata Institute of Geoscience, Univ. of Tsukuba	Crystal Structure of Micro-minerals and Their Transformation
87-076	H. Iwasaki Photon Factory, National Laboratory for High Energy Physics	Study of Disorder in Alloys and Compounds Using Anomalous Scattering of Synchrotron Radiation
87-077	M. Tokonami Faculty of Science, Univ. of Tokyo	Structure Study of the γ_1' Martensite Phase in a Cu-Al-Ni Alloy
87-079	M. Ohmasa Institute of Materials Science, Univ. of Tsukuba	Studies on the Dehydration Process of Al and Fe Hydroxides
87-080	K. Ohtsuka Institute of Materials Science, Univ. of Tsukuba	Study of Rubber-like Behavior in a Au-Cd Alloy by X-Ray Diffraction and Topography
87-081	S. Sasaki Photon Factory, National Laboratory for High Energy Physics	Study on the Stable Phase of Al-Mn Quasicrystal
87-082	Y. Izumi Faculty of Science, Hokkaido Univ.	Tertiary Structure of Calmodulin in Solution
87-083	Y. Izumi Faculty of Science, Hokkaido Univ.	Structural Study of Gelation of Branched Polyethylene in Solution
87-084	H. Urakawa Faculty of Engineering and Design, Kyoto Institute of Technology	Micelle Structure of Polyethylene Glycol Monoether Liquid Crystal

87-085	S. Kikuta Faculty of Engineering, Univ. of Tokyo	Analysis of Crystal Surface Structure by X-Ray Diffraction
87-086	G. Artioli Univ. of Modena Italy	Structural Analysis of Silicate Microcrystals with Synchrotron Radiation
87-087	K. Ishida Faculty of Science & Technology, Science Univ. of Tokyo	Measurement of Anomalous Dispersion of X-Rays
87-088	K. Yoshihara Faculty of Science, Tohoku Univ.	Chemical Effects on X-Ray Intensity Ratios of Nuclei Excited by Synchrotron Orbital Radiation
87-089	S. Kikuta Faculty of Engineering, Univ. of Tokyo	Study of Diffraction and Scattering Phenomena under Laser Irradiation
87-090	S. Kikuta Faculty of Engineering, Univ. of Tokyo	Nuclear Resonant Bragg Scattering by Synchrotron Radiation
87-091	S. Kikuta Faculty of Engineering, Univ. of Tokyo	Structure Analysis of Interfaces by X-Ray Standing Wave Method
87-092	S. Kikuta Faculty of Engineering, Univ. of Tokyo	Characterization of Mixed Crystals and Superlattices Using Highly Monochromatic and Collimated Incident X-Rays
87-093	T. Mukoyama Institute for Chemical Research, Kyoto Univ.	Nuclear Excitation by Synchrotron Radiation
87-094	K. Tsuji Faculty of Science & Technology, Keio Univ.	Structure of Liquid Gallium and Germanium under Pressure
87-095	T. Hondoh Faculty of Engineering, Hokkaido Univ.	Dynamical Behavior of Point Defects at Growing Ice-water Interface
87-096	T. Kino Faculty of Engineering, Hiroshima Univ.	Dynamical Observation of Lattice Defects in Nearly Perfect Aluminum Single Crystals
87-097	K. Namikawa Tokyo Gakugei Univ.	Simultaneous Observation of Micro Magnetic Properties by Means of X-Ray Magnetic Scattering
87-098	K. Namikawa Tokyo Gakugei Univ.	X-Ray Parametric Frequency Conversion
87-099	T. Yamasaki Department of Material Science Himeji Institute of Technology	Compositional Dependence of Temper Embrittlement of Fe-based Amorphous Alloys
87-100	T. Ishikawa Photon Factory, National Laboratory for High Energy Physics	Ultra Plane Wave X-Ray Topography
87-101	T. Sekine National Institute for Research in Inorganic Materials ²	In-situ Measurement of the Lattice Constant of Wüstite Solid Solution under High Pressure
87-102	D. Rubie Univ. of Manchester U.K.	Investigation of the Mechanisms and Kinetics of the Olivine-Spinel Transformation

- 87-103 S. Aoki
Institute of Applied Physics,
Univ. of Tsukuba Study of Sub-1000 Å Imaging with Soft X-Ray
Microscope
- 87-104 H. Maezawa
Photon Factory,
National Laboratory for
High Energy Physics Investigation of Soft X-Ray Optics and Technology
for Undulator Radiation Utilization
- 87-105 Y. Sato
Research Institute for
Scientific Measurement,
Tohoku Univ. Dissociative Photoionization of $\text{Ge}(\text{CH}_3)_4$,
 $\text{Sn}(\text{CH}_3)_4$, $\text{Pb}(\text{CH}_3)_4$ by Soft X-Ray Excitation
- 87-106 M. Yanagihara
Research Institute for
Scientific Measurement,
Tohoku Univ. Studies on the Soft X-Ray Multilayer Coatings
- 87-107 T. Nagata
Department of Science and
Technology, Meisei Univ. Multiple-photoionization of Metal Atoms
- 87-108 Y. Nihei
Institute of Industrial Science,
Univ. of Tokyo Rapid Acquisition of Two-dimensional
Photoelectron Diffraction Patterns by Utilizing
Wavelength Tunability
- 87-109 S. Suzuki
Faculty of Science,
Tohoku Univ. X-Ray Photoemission Study of 3d Levels in Heavy
Rare Earth Valence Fluctuation Compounds
- 87-110 T. Takizawa
College of Humanities and Science,
Nihon Univ. Electronic Structure of Ternary and Multinary
Crystals
- 87-111 T. Koide
Photon Factory,
National Laboratory for
High Energy Physics Magnetic-circular-dichroism Study of the
Electronic States of Transition Metals and
Their Compounds
- 87-112 S. Kono
Faculty of Science,
Tohoku Univ. A Trial to Measure Surface Core-level Shift
Photoelectron Diffraction
- 87-113 Y. Hatano
Faculty of Science,
Tokyo Institute of Technology Dissociation of Superexcited States of Simple
Polyatomic Molecules
- 87-114 T. Namioka
Research Institute for Scientific
Measurement, Tohoku Univ. High-resolution Spectroscopy of Atoms and
Molecules in the VUV Region
- 87-115 S. Aoki
Institute of Applied Physics,
Univ. of Tsukuba Study of Soft X-Ray Holographic Interferometry
- 87-116 S. Yoshida
Faculty of Engineering,
Kyoto Univ. Characterization of Structures of Highly
Dispersed Vanadium Oxides Prepared by Chemical
Vapor Deposition
- 87-117 H. Ino
Faculty of Engineering,
Univ. of Tokyo Study of N and C in Iron Using EXAFS
- 87-118 H. Ino
Faculty of Engineering,
Univ. of Tokyo Study of Al-Mn Quasi-Crystal by EXAFS
- 87-119 M. Miyake
Faculty of Engineering,
Yamanashi Univ. Study on Bonding Structure of Iodine and Bromine
Atoms Intercalated into Carbon

- 87-120 T. Yamamura
Faculty of Science,
Science University of Tokyo EXAFS and XANES Study of the Coordination of Nickel-Thiolate Complexes in Terms of the Abnormally High Valent Nickel Site in Uptake Hydrogenases
- 87-121 T. Onishi
Research Laboratory of Resources Utilization, Tokyo Institute of Technology The Study on the Structure of Intercalated Metals within Layered $K_4Nb_6O_{17}$
- 87-122 T. Yoshida
Faculty of Engineering,
Univ. of Tokyo A Study on the Correlation between the Local Structure and Photo-catalytic Activity by Supported Niobium Oxides Catalysts
- 87-123 H. Yamazaki
Faculty of Science,
Okayama Univ. Structure of Oxide Superconductors
- 87-124 H. Endo
Faculty of Science,
Kyoto Univ. Chemical Short Range Order in Liquid Rb-Se Alloys
- 87-126 Y. Noda
Faculty of Engineering Science,
Osaka Univ. Local Distortion Associated with Cooperative Jahn-Teller Phase Transitions
- 87-127 T. Yokokawa
Faculty of Science,
Hokkaido Univ. EXAFS Study on Sodium Borate and Sodium Silicate Glasses Containing Nickel Oxide
- 87-128 Y. Saito
Institute of Industrial Sciences,
Univ. of Tokyo EXAFS Characterization of Binary Metal Oxides Produced in Zeolite Matrix
- 87-129 K. Oki
Interdisciplinary Graduate School of Engineering Sciences,
Kyushu Univ. Valence Fluctuation of Ce in Pd-Ce Alloys
- 87-130 K. Koto
Institute of Scientific & Industrial Research,
Osaka Univ. Structure of Liquid State Bismuth Sesquioxide
- 87-131 M. Ichikawa
Research Institute for Catalysis,
Hokkaido Univ. Characterization of Zeolite-encapsulated Metal Phthalocyanin Catalysts
- 87-132 H. Kuroda
Faculty of Science,
Univ. of Tokyo Cu 1S+3d XANES and Valency of Superconductors: La-Sr(Ba)-Cu-O and A-Ba-Cu-O (A=Y, RE)
- 87-133 H. Kuroda
Faculty of Science,
Univ. of Tokyo EXAFS Studies on Rh-, Ru- and Fe-supported on the Layer Surfaces of Synthetic Clay Mineral and Other Layer Compounds
- 87-134 K. Kai
Research Institute for Iron, Steel & Other Metals,
Tohoku Univ. Electronic States of Cu in $YBa_2Cu_3O_{7-x}$ (X=0~1)
- 87-135 T. Yokoyama
Faculty of Science,
Hiroshima Univ. Temperature Dependence of the EXAFS Spectra for Ultra Fine Metal Particles
- 87-136 M. Niwa
Faculty of Engineering,
Nagoya Univ. An EXAFS Study on the Structure of Metal Oxide on Zeolites Prepared by CVD Method

- 87-137 M. Sano Systematic Studies of XANES Spectra for Platinite
College of General Education, Complexes and Their Rules
Nagoya Univ.
- 87-138 M. Sano Structural Studies of Ga-substituted Zeolite Gel
College of General Education,
Nagoya Univ.
- 87-139 A. Tomita Studies on the Local Structures of the Catalysts
Chemical Research Institute of for Coal Gasification
Non-Aqueous Solutions, Tohoku Univ.
- 87-140 N. Kamijo Dynamical Study on EXAFS and XANES in Metal Oxide
Government Industrial Research Super Ionic Compounds
Institute, Osaka¹
- 87-141 I. Nakai Studies on Precipitation Reactions in Analytical
Department of Chemistry, Chemistry by EXAFS and XANES Techniques
Univ. of Tsukuba
- 87-142 H. Kuroda Evaluation of the Fluorescent X-Ray Detector for
Faculty of Science, Surface EXAFS Experiments
Univ. of Tokyo
- 87-143 Y. Satow Development of EXAFS Instrumentation at High
Photon Factory, Photon Energy above 30 keV
National Laboratory for
High Energy Physics
- 87-144 M. Nomura Fluorescent EXAFS Study of Solute Structure
Photon Factory,
National Laboratory for
High Energy Physics
- 87-145 F. Ito Amorphization Process of the Mechanical Alloying
Research Institute for Iron, and Grinding for Ni-Zr Alloys by Means of EXAFS
Steel & Other Metals, Tohoku Univ.
- 87-146 K. Kajiwara Sol-Gel Transition of k-Carrageenan
Institute for Chemical Research,
Kyoto Univ.
- 87-147 K. Kajiwara Characterization of Thermotropic Liquid
Institute for Chemical Research, Crystalline Cellulose Derivatives
Kyoto Univ.
- 87-148 T. Yamane Structure Changes in Bowman-Birk Type Protease
Faculty of Engineering, Inhibitors Studied by X-Ray Solution Scattering
Nagoya Univ.
- 87-149 T. Hirai Structure Formation of Amylose and Synthetic
Faculty of Textile Science Polymer Induced by the Complexation with Iodine
and Technology, Shinshu Univ.
- 87-150 Lu Kunquan Extended X-ray Absorption Fine Structure (EXAFS)
Institute of Physics Academia for Mixed-phase System and Mixed-coordination
Sinica, China System
- 87-151 A. Itai Crystallographic Studies of Enzyme-inhibitor
Faculty of Pharmaceutical Complexes and Molecular Design of Inhibitors
Science, Univ. of Tokyo
- 87-152 W.A. Hendrickson Development of Methodology for Multiwavelength
Columbia Univ. Anomalous Diffraction Analysis of Protein
USA Structure
- 87-153 H. Inoue The Reconstitution Process of Tobacco Mosaic
National Institute of Virus from Different Mutant Components Measured
Agrobiological Resources³ by the Time-resolved X-Ray Solution Scattering

87-154	K. Kihara Faculty of Science, Kanazawa Univ.	Structure Determination of Superstructure Minerals on the Basis of Powder Diffraction Profile Analyses
87-155	Y. Gohshi Faculty of Engineering, Univ. of Tokyo	Chemical State Imaging by XRF Image Reconstruction
87-156	M. Mori College of General Education, Nagoya Univ.	Direct Observation of Charge Density Wave in Chromium
87-157	Y. Fujii Faculty of Engineering Science, Osaka Univ.	P-T Phase Diagram Associated with Pressure-induced Molecular Dissociation in Solid Iodine
87-158	K. Kamigaki Research Institute for Iron, Steel & Other Metals, Tohoku Univ.	Spontaneous Distortion in Antiferromagnetic Compounds
87-159	M. Ando Photon Factory, National Laboratory for High Energy Physics	X-Ray Optical Characterization of Nearly Perfect Single Crystals for Development of X-Ray Optical Elements
87-160	M. Morinaga Toyohashi Univ. of Technology, School of Production Systems Engineering	Analysis of Diffuse X-Ray Scattering from the Omega Phase in Titanium Alloys
87-161	H. Iwasaki Photon Factory, National Laboratory for High Energy Physics	Effect of Pressure on the Molecule Orientational Disorder in Crystals
87-162	S. Sueno Institute of Geoscience, Univ. of Tsukuba	A Study of New and Earth Interior Materials Based on the X-Ray Structure Analysis of Micro-single Crystal and Twinned Crystal
87-163	T. Chikaura Faculty of Engineering, Kyushu Univ.	Observation of Thermal Behavior of Microdefects in Thin Silicon Wafers by Means of Highly-plane-wave SR Topography
87-164	N. Yamaguchi Plasma Research Center, Univ. of Tsukuba	X-Ray Detection Characteristics of Microchannel Plates for Plasma Diagnostics
87-165	S. Takeuchi College of Integrated Science, Univ. of Osaka Prefecture	Magnetic X-Ray Scattering Studies of γ Mn-Ni Alloys
87-166	M. Wakabayashi Institute of Materials Science, Univ. of Tsukuba	Experimental Determination of the Compression Curve for Graphite at High Temperatures for Accurate Calculation of the Graphite/Diamond Equilibrium Relation
87-167	K. Tsuji Faculty of Science & Technology, Keio Univ.	Structure of Liquid and Crystalline Bismuth under Pressure
87-168	Y. Noda Faculty of Engineering Science, Osaka Univ.	Relationship between High Pressure Phase and ω -Phase of Zr Based Alloys
87-169	Y.S. Sorensen Univ. of Washington USA	Accurate Powder Diffraction Measurements under Uniaxial Stress

87-170	H. Arashi Research Institute for Scientific Measurement, Tohoku Univ.	Phase Transition of HfO_2 High Temperatures and High Pressures
87-171	H. Sawamoto Faculty of Science, Univ. of Nagoya	Measurement of Compressibility of Silicate and Fe-O-S Melt in the Earth and Planetary Interior
87-172	H. Sawamoto Faculty of Science, Univ. of Nagoya	Measurement of Compressibility of β - and γ - Mg_2SiO_4 at High Temperatures
87-173	O. Shimomura National Institute for Research in Inorganic Materials ²	High Pressure X-Ray Diffraction Study Using Imaging Plate
87-174	J. Chikawa Photon Factory, National Laboratory for High Energy Physics	Development of New Methods in Synchrotron Radiation Research Using Imaging Plate
87-175	S. Yasumi Teikyo Univ.	Studies on the M-Shell of the Dysprosium Atom Using Monochromatic X-Rays for Determining the Mass of the Electron Neutrino
87-176	T. Miyahara Photon Factory, National Laboratory for High Energy Physics	3d and 3p XPS of Intermetallic Compounds with Light Rare-Earths and 3p Resonant XPS of Heavy Rare Earths
87-177	S. Nakai Faculty of Engineering, Utsunomiya Univ.	X-Ray Emission Spectroscopy of Rare-Earth Compounds Excited by Monochromatized SR
87-178	T. Ohta Faculty of Science, Hiroshima Univ.	Study of Inner Shell Polarized Spectra of Oriented Polymer Films
87-179	T. Koide Photon Factory, National Laboratory for High Energy Physics	Study of the Surface-roughness Effect on Grating Efficiencies in the Soft X-Ray Region
87-180	N. Miyamoto Research Institute of Electrical Communication, Tohoku Univ.	Photo-chemical Reaction of SiH_2Cl_2 , SiH_4 , CH_4 , and NH_3 Chemisorbed on Si Surface
87-181	H. Fukutani Institute of Physics, Univ. of Tsukuba	Piezoreflectance Spectra of Alkali and Alkaline-Earth Halides
87-182	H. Fukutani Institute of Physics, Univ. of Tsukuba	Angle-resolved Photoelectron Spectroscopy of O-covered Pd(110) Surface
87-183	T. Miyahara Photon Factory, National Laboratory for High Energy Physics	Absorption and Near-normal Reflectance Measurements on Rare-Earth Compounds and Alloys
87-184	H. Sugawara Faculty of Education, Gunma Univ.	Photoelectron Spectroscopy of the Intermediate Valence Systems $\text{Sm}_{1-x}\text{La}_x\text{B}_6$ and $\text{Sm}_{1-y}\text{Yb}_y\text{B}_6$
87-185	H. Takeuchi Japan Atomic Energy Research Institute ²	Characteristics of Flat Field Spectrometers for Fusion Plasma Diagnostics

87-186	K. Ito Photon Factory, National Laboratory for High Energy Physics	Study on the Dissociative Photoionization of Simple Molecules
87-187	Y. Morioka Institute of Physics, Univ. of Tsukuba	The Study of High Resolution Absorption Spectra of H_2O and D_2O
87-188	Y. Sugitani Dept. of Chemistry, Univ. of Tsukuba	Depth Analysis of Layered Materials by Correlation Photoacoustics
87-189	I. Anno Institute of Clinical Medicine, Univ. of Tsukuba	Angiography of Small Animals Using High Speed Energy Subtraction
87-190	S. Kikuta Faculty of Engineering, Univ. of Tokyo	Analysis of Crystal Surface and Interface Structures by Soft-X-Ray Diffraction
87-191	Y. Murata The Institute for Solid State Physics, Univ. of Tokyo	Study of Alkali Halide Overlayer on Semiconductors I
87-U001	T. Takahashi Faculty of Science, Tohoku Univ.	Photoemission Study of High-Tc Superconductive Oxides
87-U002	H. Kuroda Faculty of Science, Univ. of Tokyo	XANES and EXAFS of High Tc Superconductive Ceramics
87-U003	H. Oyanagi Electrotechnical Laboratory ¹	Structural Studies of High Tc Oxide Superconductors by EXAFS and X-Ray Diffraction
87-U004	R. Yoshizaki Institute of Applied Physics, Univ. of Tsukuba	High Temperature XANES and EXAFS Studies of the High-Tc Superconductor
87-U005	H. Ihara Electrotechnical Laboratory ¹	Structural Study of Oxide Superconductors under High Temperature and High Pressure by X-ray Diffraction
87-U006	Y. Endoh Faculty of Science, Tohoku Univ.	Correlation between the Crystal Structure and Oxygen Deficiency in $La_2CuO_{4-\delta}$

7.2 Proposals accepted for charged Beam time assignment

<u>Proposal Number</u>	<u>Spokesperson</u>	<u>Title</u>
87-Y001	D. Shinoda R & D Group, NEC Co.	X-Ray Optics, X-Ray Lithography Experiments
87-Y002	N. Ogirima Central Research Laboratory, Hitachi Ltd.	BL-8A; Wavelength Purifying System for Soft X-Rays, B; InSb(111) Monochromator, C; CT Method Using X-Ray Image Sensor
87-Y003	H. Sato NTT Electrical Communications Laboratories	Analysis, Lithography and Photo-reaction Using SOR
87-Y004	K. Yoshida Research Center, Mitsubishi Chemical Industries Ltd.	The EXAFS Study of Catalysts
87-Y005	N. Yamamoto Central Research Laboratory, Idemitsu Kosan Co., Ltd.	EXAFS Study of Ti and Al Complex Catalyst
87-Y006	H. Sato NTT Electrical Communications Laboratories	EXAFS Studies of Superconducting Materials
87-Y007	K. Nagai Research & Development Center, Toshiba Corporation	X-Ray Lithography
87-Y008	Y. Goto R & D Planning and Technical Service Division, NEC Co.	X-Ray Optics, X-Ray Lithography Experiments
87-Y009	B. Oguchi Fujitsu Laboratories Ltd.	Synchrotron Radiation Test for Exposure System in BL-17C

8. PF SEMINARS, MEETINGS AND PUBLICATIONS

PF seminars

- Chehab, R. (ORSAY)
Accelerator Activities in ORSAY
(1) Present Status of ORSAY Accelerators (2.3 GeV Linac, DCI, ACO, Supure ACO),
(2) The LEP Preinjector
October 3, 1986
- Smith, P. (Harvard - Smithsonian Center for Astrophysics)
VUV Rotational Line f-values for Molecules Seen in Diffuse Interstellar Clouds
October 22, 1986
- Bianconi, A. (Univ. of Roma)
X-ray Spectroscopy on Solids and Biological Materials
October 22, 1986
- Hart, M. (Phys. Dept., Manchester Univ.)
Some Latest Synchrotron Radiation Research Topics Using Specially Designed Bragg Reflection
X-ray Optics
December 10, 1986
- Kuriyama, M. (NBS)
The Fundamental of Scattering Processes
December 15, 1986
- Saile, V. (HASYLAB)
Two-photon Photoemission from Molecular Crystals Combining Synchrotron Radiation
with a Laser
February 13, 1987
- Munro, I. (Daresbury)
Time Resolved Fluorescence Anisotropy Studies of Proteins and Membranes and a Review of
the Current and Proposed Research Programme at the Daresbury SRS
April 2, 1987
- Klose, W. (Karlsruhe Nuclear Research Center)
European-Synchrotron-Radiation-Facility
April 10, 1987
- Fontaine, A. (LURE)
X-ray Absorption Spectroscopy in Dispersive Mode: Time-Dependent Electrochemistry,
Solid State Amorphisation and High Pressure Experiment
April 22, 1987
- Kanaya, N. (PF)
Computer Control System and Data Processing System for European Synchrotron Radiation
Facilities
July 7, 1987
- Lagarde, P. (LURE)
Soft X-ray Experiments (Silicon Edge) at ACO.
November 4, 1987
- Williams, C. (LURE)
Recent Developments in Anomalous Small Angle X-ray Scattering (ASAXS) at LURE-Application
in Metallurgy and Physical Chemistry
November 18, 1987

Meetings

Meeting on the future plan of synchrotron radiation research	February 6-7, 1987
Workshop on soft X-ray and ultrasoft X-ray radiation biology	June 17-18, 1987
Workshop on high pressure studies with synchrotron radiation at PF	June 25-26, 1987
Workshop on a plan of next generation storage ring in the VUV and SX region	September 21-22, 1987
Workshop on circularly polarized synchrotron radiation and its application	November 16-17, 1987
5th Photon Factory symposium	November 20-21, 1987

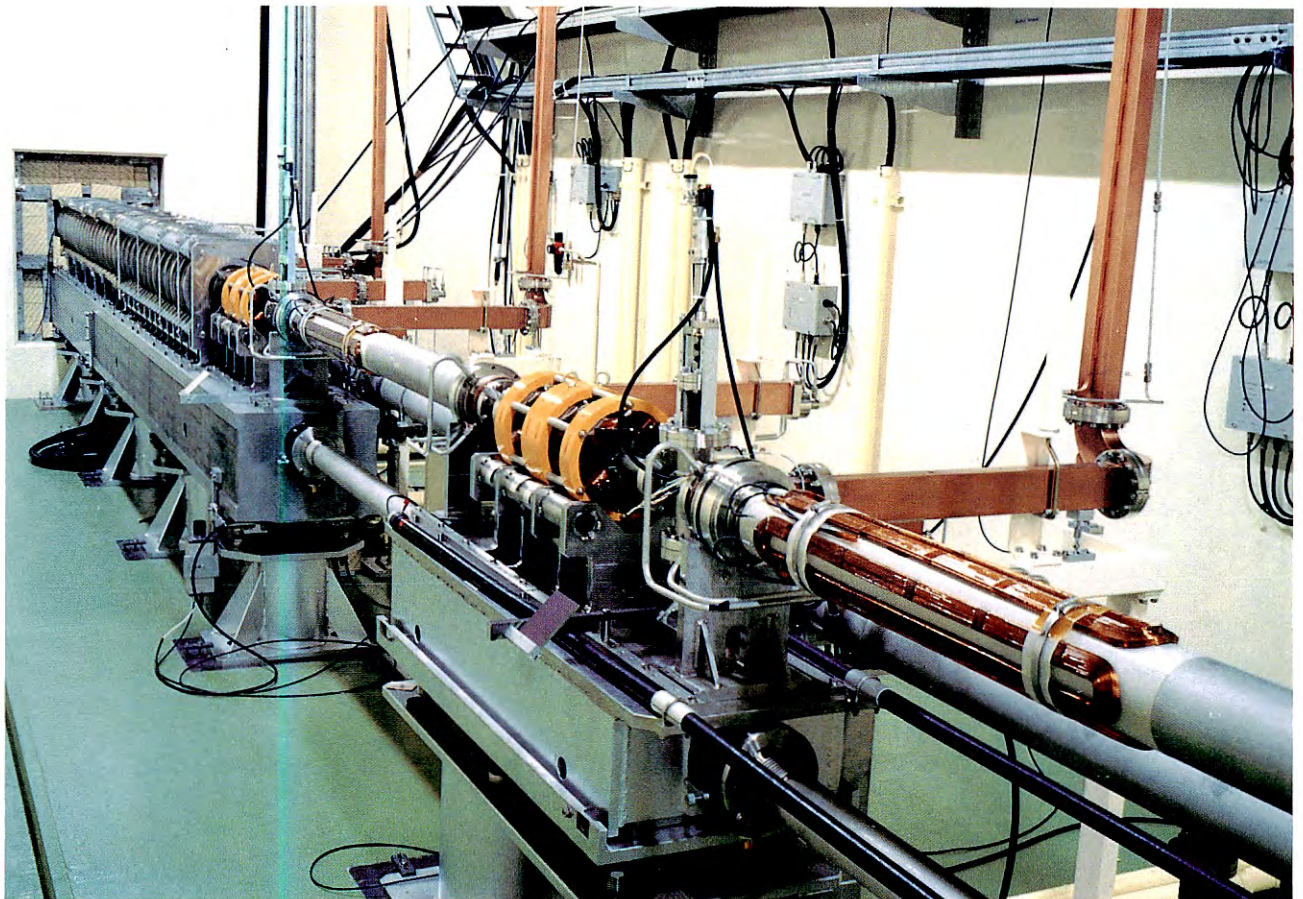
Publications

PF News

ISSN 0288-611X

Vol.5, No.1-5

Injector Linac Department



The injector unit of the positron generator.

To obtain the high beam current, focusing fields are increased and the dividing ratio of rf power is modified.

1 Introduction

During the period from Aug. 1986 to July 1987, the 2.5 GeV electron linac has been supplying electron and positron beams both to the PF ring and to the accumulation ring (AR) in the TRISTAN accelerator complex. In May 1987, TRISTAN began its main experiment to search for the top quark. This theme is one of the main subjects of TRISTAN project. As a result, the total operation time of the linac has increased by more than 40 % compared with the last period. Operation statistics of this period as well as the one of the last period are shown in Table I. It is clear that the operation time has markedly increased since May 1987. In the following, a summary to introduce some of the activities of linac group during this period is given.

In the positron generator, improvements have been done at some points. A new ceramic insulator was introduced in the gun assembly and the voltage to the gun was increased. A new grid pulser utilizing a hybrid IC was also adopted in the gun cathode and the grid pulse voltage was also increased. These modifications have improved total performance of the gun very much. The rf power feeding system to pre-buncher and buncher sections was also modified. In the old system, there were some unbalances in the feeding power ratios among a pre-buncher, a buncher and a regular accelerator guide. In the pre-buncher and buncher sections, the rf power had been not enough to bunch and accelerate the beam properly. By the modification, the pre-buncher and buncher are excited with an enough rf power so as to bunch the beam properly.

A pulsed solenoid coil was inserted immediately after the electron-positron converter to increase the capture efficiency of positrons. Another modification was made in the beam transport line between the positron generator and 2.5 GeV pf linac (so called 30 degree beam

transport line) by adding two sets of quadrupole magnets for the emittance matching. The new optics has increased the beam transfer efficiency. These improvements made the operation of positron generator easy to get positron beam of about 15 mA steadily.

A differential pumping system which is the same as in the electron gun system of the positron generator was also adopted in the electron gun of the pf linac. By this adoption, the vacuum in the cathode space has been much improved and the life time of the gun cathode has been increased correspondingly.

In the rf system, 47 pulsed klystrons of 30 MW output are operating. During operation, the phase adjustment of all klystrons is an important but troublesome procedure. To make the phase adjustment automatically, an adjusting system was planned, constructed and tested. By the end of this period, the system has been almost completed and confirmed that the system operates well in principle. Work to refine the system for continuous operation will follow soon. At the same time, a monitoring system to monitor and display rf output status of all klystrons in detail is under construction.

A preliminary experiment to generate a very large accelerating field was made in Aug. 1987. By means of a recirculation method, an accelerating field of about 60 MV/m has been obtained in a short accelerator guide which was built in the recirculation ring as one of the components.

In the linac, 47 klystrons are operating and about 15 klystrons are purchased in every year. In FY 1986, we purchased 15 klystrons and some of them are installed in the klystron gallery and are operating. It turned out recently that some of the klystrons made in FY 1986 died after a rather short operation time. The reason is not known yet. We are now investigating the reason of such a short life time of klystrons and the best way to overcome this

Table 1.1 Summary of linac operation time

Period	Operation time	Ratio to Last year	Remarks
Period II, FY 1986			
Oct. 6 - Dec. 20	1216	1.09	
Dec. 21, 1986 - Jan. 12, 1987			shut down
Period III, FY 1987			
Jan. 12 - Mar. 20	1128	1.08	
Mar. 21 - Mar. 31			Shut down
Period I, FY 1987			
Apr. 1 - May. 6			Shut down
Apr. 13 - Apr. 28	64		test operation
May 6 - Jul. 26	1544	1.56	
Jul. 27 - Sep. 27			shut down
Aug. 27 - Sep. 22	72		test operation
Total	4024	1.45	

Table 1.2 Operation trouble statistics

	Number of trouble	Lost time (h)	Ratio
Klystral	1	24.0	48.5 %
Modulators	6	4.27	8.6
Gun pulser system	2	11.58	23.4
Beam transport	3	3.38	6.8
Control	4	2.58	5.2
Others	2	3.67	7.5
Total		49.48	

problem.

2 Progress of the positron generator injector

2.1 Electric gun system development

The electron gun system has been improved in several points; a new ceramic insulator, a grid pulser, and a remote control of the emission current. The life time of the cathode was also investigated.

New ceramic insulator

It was confirmed last year that raising the gun voltage improved the characteristics of the emission current of the gun. The ceramic insulator was enclosed by an SF₆-gas-filled capsule in order to supply a cathode-anode voltage of 160 kV to the gun. The maintenance of the SF₆ gas, however, was troublesome so that the ceramic insulator was replaced by a new large one as not to use the SF₆-gas-filled capsule. (Fig. 2.1)

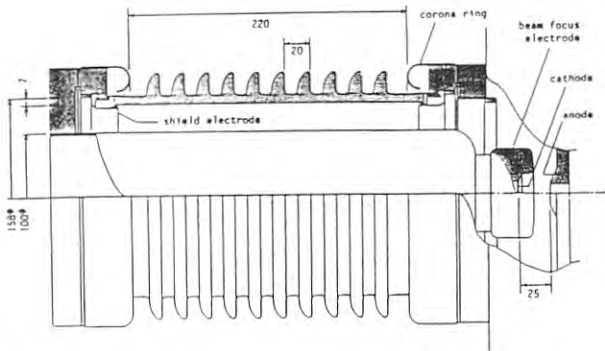


Fig. 2.1 New large ceramic insulator installed in the electron gun.

Development of a grid pulser utilizing a hybrid IC

A grid pulser for a high-intensity and short-pulse electron gun has been under development for several years. It became clear that one of the most important points for a high speed grid pulser was the decrease of the stray capacitance and inductance of the circuit. In this connection, a grid pulser utilizing a hybrid IC made of 2N2222A's was made for a test and a good characteristic was obtained. Figure

2.2 shows a hybrid IC for the pulser which is one-fourth of the can-type transistor circuit in size and has the small stray capacitance and inductance. The output voltage waveforms of the pulser with a can-type transistor and a hybrid IC are shown in Fig. 2.3. The emission current from the gun using both circuits are shown Fig. 2.4. It is expected that by making a hybrid IC with transistors of a higher slew rate (2N5551), the output voltage of the grid pulser will increase by a factor of 1.4 and as a result the emission current of the gun will increase correspondingly.

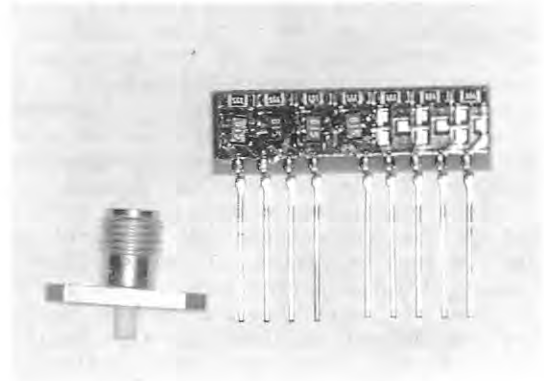


Fig. 2.2 Hybrid IC of 2N2222A developed for the grid pulser.

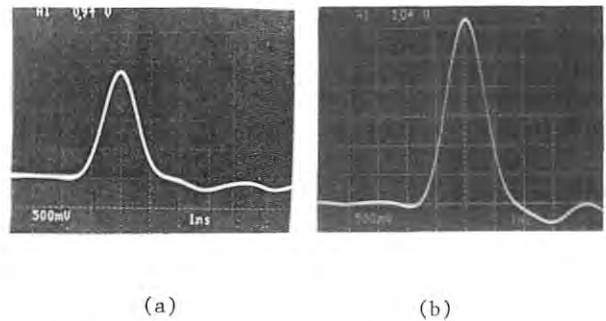


Fig. 2.3 Output waveforms of the grid pulsers in two cases; (a) can-type transistor, (b) hybrid IC.

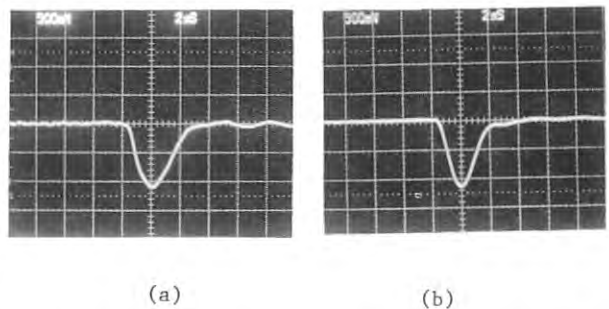


Fig. 2.4 Beam waveforms of the electron gun in two cases; (a) can-type transistor, (b) hybrid IC.

Remote control of an emission current

As the grid pulser is using avalanche transistors to produce a short pulse, the output voltage cannot be varied. A general way to vary the output pulse height is accomplished by applying a variable dc-bias-voltage to the cathode-grid gap. However a bias power supply had not had an enough range to examine the beam characteristics of the positron generator. This time by applying a pulsed bias voltage (1 μ sec) to the cathode-grid gap, the emission current was able to be varied without any distortion of the waveform. (Fig. 2.5)

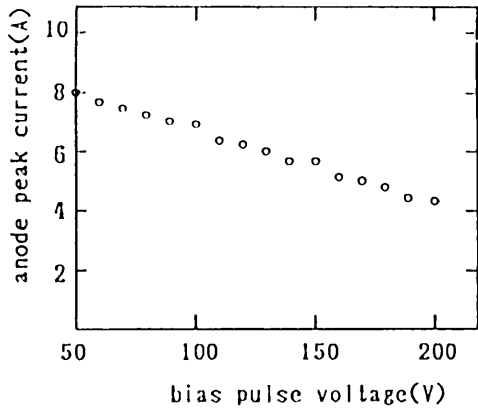


Fig. 2.5 Remote control of the emission current of the electron gun.

Emission characteristics

Typical emission characteristics are shown in Fig. 2.6 and Fig. 2.7. It seems that the cathode-anode voltage of 160 kV is appropriate for the present gun system (Fig. 2.7), and the possibility remains that the emission current increases with the output voltage of the grid pulser (see Fig. 2.5).

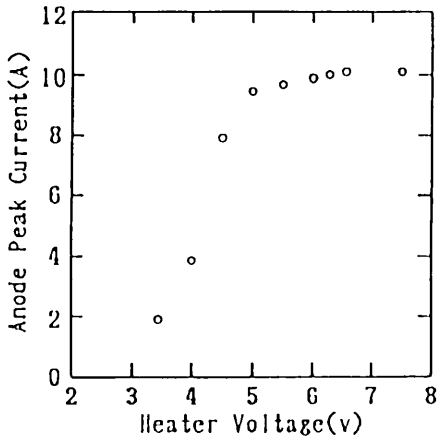


Fig. 2.6 Emission characteristics of the electron gun (1).

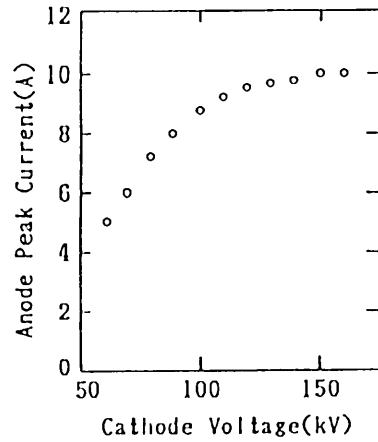


Fig. 2.7 Emission characteristics of the electron gun (2).

Cathode life

The cathode life is one of the most important problems in the operation of the gun system. For a quantitative analysis, the time variation of the characteristics of the heater voltage vs. anode peak current has been followed for a three-month operation period (Fig. 2.8). The cathode degradation for first 48 hours (corresponding to beam-on time) is predominant compared with later times. The exchange of the cathode is not necessary for three months and the current is enough for the present TRISTAN operating mode.

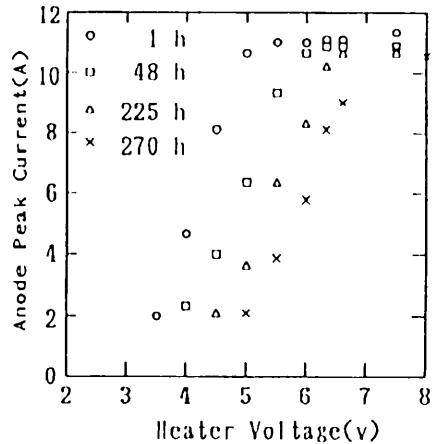


Fig. 2.8 Time variation of the emission characteristics of the electron gun. Estimated beam ON times are shown where a pulse repetition rate is 10 pps.

2.2 Modification of the waveguide system

With the increase of the injection current from the gun as mentioned in previous section, it turned out that the rf power to the buncher

was not enough to accelerate the injected electrons effectively. To solve this problem the waveguide system of the injector was modified from the one shown in Fig. 2.9(a) to that in Fig. 2.9(b). In Fig. 2.9(a) only a quarter of the total rf power is fed into the buncher, whereas in Fig. 2.9(b), the rf power of the buncher is half of the total power. On the other hand the rf power to the second accelerator guide is reduced to half power in the case of Fig. 2.9(a). With this configuration of the waveguide, a beam test was carried out, and its result is shown in Fig. 2.10. Accelerator currents measured at the end of the injector (monitor 1) and at the end of the acceleration unit 3, i.e. the last unit upstream of the target (monitor 3E), are plotted as a function of the rf power to the buncher. This figure shows saturation, i.e., sufficient rf power is now available for acceleration. It is to be noted, however, that positron yield decreased a little due to this waveguide modification. This is probably because the energy of electrons bombarding the target decreases owing to the rf power reduction at the second accelerator.

Another significant improvement was a modification of the transport system of the electron accelerator part, which made tuning of the accelerator appreciably easier. Details of this improvement are described elsewhere.

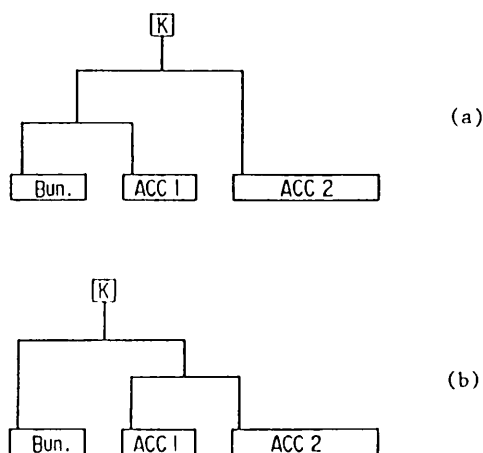


Fig. 2.9 Modification of rf waveguide.
(a) previous configuration
(b) present configuration

2.3 Acceleration characteristics of the positron generator injector

Relation between the accelerated current and the injection current.

In the course of development of the injector, it was sometimes experienced that exhaustive tuning to increase the injection current did not increase the accelerated current or positron current. This is probably due to the following reasons; the beam quality deterio-

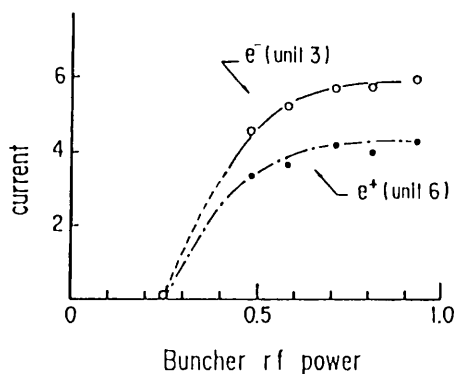


Fig. 2.10 Accelerated currents vs. the buncher rf power.

rated by a space charge effect, the transmission of the beam became bad, the beam emittance was too large at the target, etc.

To check this problem systematically, the relationship between the injection current and the accelerated currents at various positions of the accelerator was studied.

When the injection current is varied, it is necessary to adjust the beam transport elements, and to tune the rf phases, if necessary. The result is shown in Fig. 2.11. The ordinate shows several points along the generator, where beam currents are measured with wall-current monitors (WMP); WMP-6E is at the end of acceleration unit 6 (the last unit of the positron generator). From the figure, the currents at various positions seem to change in a reasonable way with the change of the injection current. This relation is more clearly shown in Fig. 2.12, where the accelerated currents are plotted as a function of the injection currents. In the figure, two other wall-current monitors WMP-S11B, WMP-2E are added; these are at the end of S11B and of the unit 2, respectively. From Fig. 2.12, the accelerated currents change linearly with changes of the injection current, therefore they can be increased further if the injection current is increased.

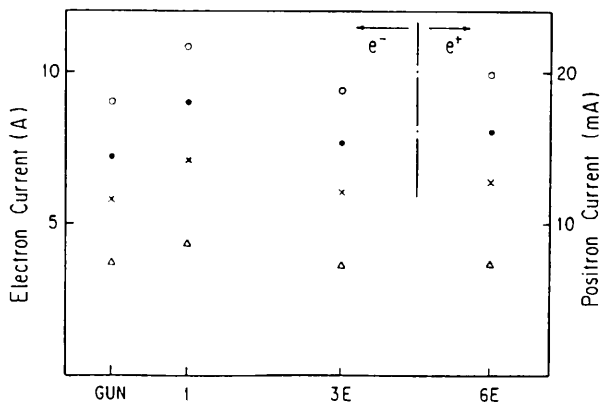


Fig. 2.11 Beam currents measured at several points along the generator.

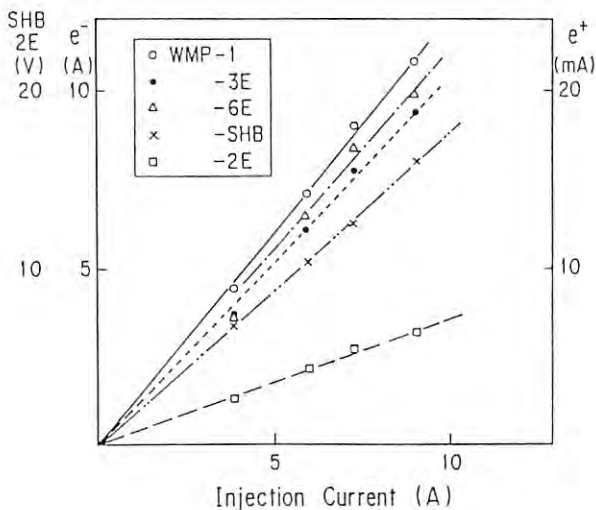


Fig. 2.12 Relation between the injection current and the accelerated currents.

Relation between the accelerated current and the SHB rf power

The rf power of the SHB has been 2 kW, which was determined from operating experience and a simple estimation. When the beam width is very narrow like 2 ns, it is difficult to produce an exact beam waveform for a monitor such as a wall current detection type. Recently a streak camera became available for measuring the beam waveform, so that the relation between the accelerated beam and the SHB rf power was investigated.

When the SHB power was varied from 2 kW to 5.5 kW, the accelerated currents were measured with a current monitor and the beam bunch was observed with the streak camera at the end of the generator. When the SHB power was varied, some of the transport elements had to be readjusted to obtain the maximum beam currents. A typical example of the beam waveform is shown in Fig. 2.13, where the SHB rf power was 4 kW. The pulse width of the grid pulser was ~ 4 ns, the injection current was 8.4 A, and the electron current was 10.3 A

Some results of the experiment is shown in Fig. 2.14 and Fig. 2.15, where the rf power is 3 and 5 kW, respectively. Figure 2.14(a) and 2.15(a) are waveforms measured with WCM-6E, and Fig. 2.14(b) and 2.15(b) are beam bunches measured with the streak camera. The streak camera output had a fairly large fluctuation at the present stage; a direct quantitative comparison between different rf powers was not adequate, however, shapes of different powers can be compared. When the rf power is raised, it is clearly seen that the beam width becomes shorter. Comparing the waveforms of WCM-6E with the streak camera, the rise time of WCM waveform corresponding to the time interval from the first to the last bunches, that is, the peak value of the WCM waveform, represents most likely not the peak current but the total charge of the beam pulse. On the other hand, peak values of the WCM for different rf powers were nearly the same, therefore, the peak value of the actual positron beam possibly became larger

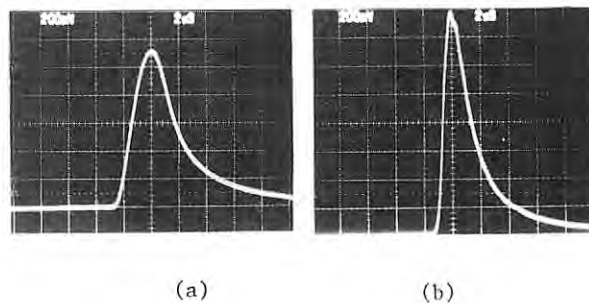


Fig. 2.13 Example of the beam waveform at SHB rf power of 4 kW.

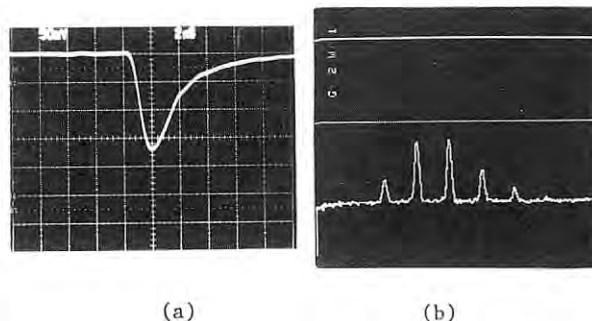


Fig. 2.14 Positron waveform (a) and its bunches (b) at SHB rf power of 3 kW.

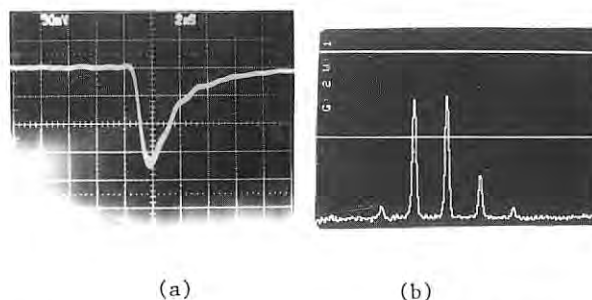


Fig. 2.15 Positron waveform (a) and its buncher (b) at SHB rf power of 5 kW.

with increase of the SHB rf power. After this experiment the SHB power was changed from 2 kW to 5 kW for the scheduled operation of the generator.

3 Improvement of the PF linac injector

3.1 The electron gun system

Overall modifications have been made in the electron gun system up to the prebuncher: the vacuum system, the vacuum control system, the focusing system, and beam monitors. Improvement of the vacuum system was, however, the main purpose in these modifications. As a result, the emission current became considerably stable over a long period of time and noticeably increased.

Vacuum system

In the PF linac electron gun, a planner triode grid-cathode assembly is used. It has an advantage that because of the short grid-cathode distance (0.18 mm), the relatively low grid pulse voltage makes possible to draw a high current. While it has a disadvantage that the emission current is sensitive to residual gases because the cathode is an oxide-coated type. Actually, the emission current decreased rapidly when a downstream gate valve was opened after activating the cathode.

For improving this situation, major modifications in the vacuum system have been made to decrease the residual gas pressure in the gun chamber. Figures 3.1(a) and 3.1(b) show the layout of the new gun system. In order to isolate the gun chamber from the prebuncher, the same differential pumping method is adopted as in the positron generator. The gun and the prebuncher are connected with 30 mm diameter thin pipes to give low conductance. The pipes are differentially pumped with 4 ion pumps of which the pumping speed is 4 l/s each. The gun chamber is pumped by 2 ion pumps (60 l/s) and a turbo molecular pump (300 l/s) as a roughing pump.

After baking out the whole system in the temperature range between 120 to 150 °C, the pressure in the chamber became in the range of 10^{-9} Torr and the emission current became stable over a long period of time and, as a result, the current increased noticeably as indicated in Fig. 3.2 Before this modification, the emission current decreased with time and heater current of the cathode would be raised in order to maintain the emission current in the desired range.

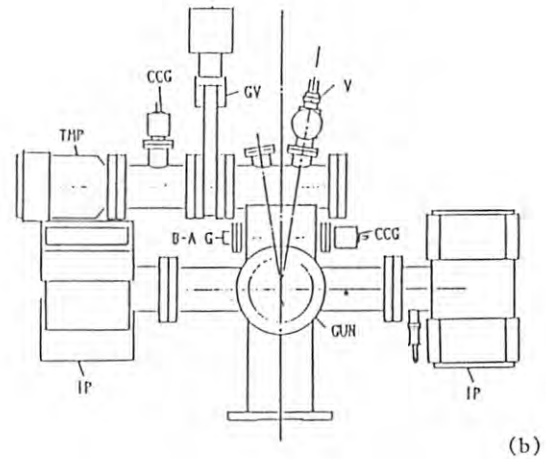
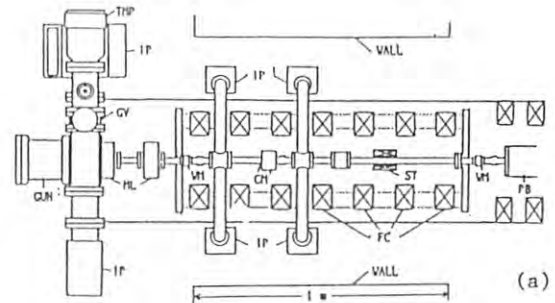


Fig. 3.1 (a), (b) Layout of the new bun system
GV: Gate valve. IP: ion pump, TMP: Turbo molecular pump, ML: Magnetic lens, WM: Wall current monitor, CM: Core monitor, ST: Steering coil, FC: Focus coil, PB: Prebuncher, B-A G: A gauge, CCG: Cold cathode gauge.

Control and monitoring system of vacuum

The control and monitor system of the electron gun vacuum system was also improved. A new control unit was made. It controls on/off switches of vacuum valves, vacuum gauges and a rotary pump locally, or remotely. It makes possible to keep the cathode safe by closing a vacuum valve (V1) when accidents happen such as a failure or an emergency in the turbo molecular pump, etc.. The circuit has also a logic as the following; If an electric power supply stops, all auto valves are closed, and even if a power supply recovers, all valves maintain the states before the recovery of power supply.

Focusing system and beam monitors

Although the improvement of the vacuum system is the main purpose in this modification, it was necessary to replace magnetic coils, focusing lenses and beam monitors with new ones since beam pipes between the gun and prebuncher should be thinner and longer than before owing to the differential pumping.

The focusing system consists of 2 magnetic lenses and 7 focusing lenses. An end plate of the focusing lenses support is made of iron so as to shield from magnetic fields and decrease

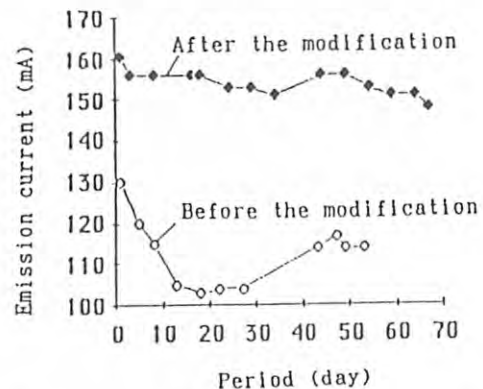


Fig. 3.2 Change of the emission current in the long range of time.

the leakage magnetic field around the cathode and the angle of the beam entering the first focusing coil. This time 2 magnetic lenses are used instead of one. Three beam monitors are placed between the gun and the prebuncher. Two of them are located between the gun and the first gate valve so as to make it possible to measure emission currents even when the valve is closed. One is a wall current monitor using lumped resistors for short beams and the other

is a core monitor for long beams. The third one is also a wall current monitor.

3.2 The rf control system for the prebuncher and buncher

The control system for changing rf phases and powers in the prebuncher and buncher was modified from a hard wired one to a one with a single board computer (SBC), which enables control from the main control console.

Main Components

The main components of the whole system is shown in Fig. 3.3. Both the prebuncher and buncher have the phase shifter and an attenuator, which have the same DC motor (DC 24 V, 4 W). In the system the SBC is utilized for the control of the driving motors through an interface board. The voltage at each potentiometer is converted to a digital signal by an ADC and displayed on a CRT in the main control room as a phase shift or an attenuation after calibration. This system is connected to the main control system of the linac through Loop-III. With this system not only fine adjustment of the rf phase and power in the prebuncher and buncher is made possible, but also any values stored in the computer can be set automatically and quickly from the console.

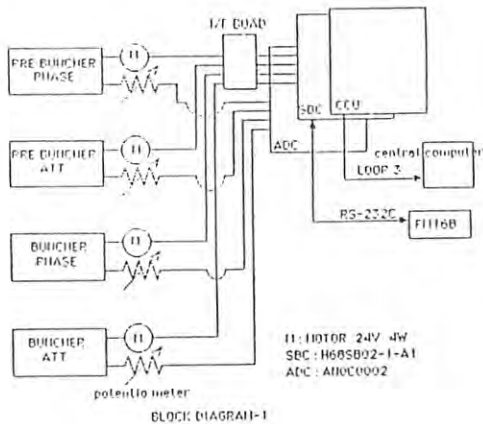


Fig. 3.3 Main components of the rf control system for the prebuncher and buncher.

SBC

The SBC is composed of a microprocessor (MC6800), ACIA (asynchronous communication interface adapter) and an I/O port (RS-232C), which can communicate with a local operator's console (a personal computer FM-11 manufactured by Fujitsu). The program is written in assembler and is less than 2 k bytes.

4. Improvements of the positron focussing system

4.1 The modification of the beam transport of the primary electron beam

Quadrupole triplets were added to the #2 and #3 acceleration units in the positron generator in April 1986. The design value of the beam emittance in these units was $P\epsilon=0.015$ π MeV/c \cdot cm, which in actual operation the beam size at the #2 and #3 acceleration units was larger and adjustments of the beam transport system there were not so easy. The addition of electromagnets solved this problem and transmission was greatly improved.

4.2 Modification of the positron target

In April 1986, the positron target and pulse coil system were modified. The main purpose was to put the water cooled pulsed-solenoid out of the vacuum chamber in order to avoid vacuum trouble. The pulsed-solenoid was operated at a maximum of 5000 A, half-sine-wave current and its power supply was a pulser using a SCR as a switching element, of which the maximum voltage was 1000 V. The pulse width was 100 μ sec, which was limited by self-inductance of the pulsed-solenoid; 5 μ H. The heat loss of this solenoid was estimated as 200 W and water-cooling was adopted. The old type solenoid was installed in the vacuum chamber using a current feedthrough, and the connecting part between the solenoid and the terminal adapter was brazed in the chamber. So there was worry that some trouble with this brazing part would lead to the possibility of vacuum trouble in the accelerator guide.

The another purpose of this modification was to add a bridge dc-solenoid between the pulsed-solenoid and the dc-solenoid on the accelerator guides in order to fill the empty field. It was pointed out that this magnetic field hole or empty magnetic field has undesired effects on the position focusing.

Figure 4.1 shows the major improvements of

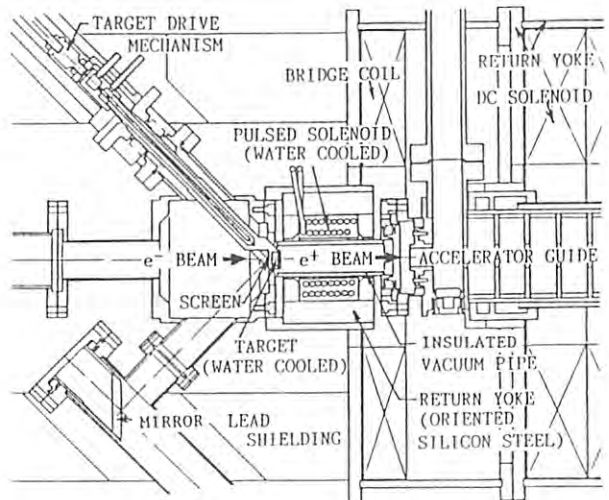


Fig. 4.1 Improved positron source.

the positron source. In this modification the pulsed-solenoid was wound on a vacuum duct made of ceramic and to compensate for a decrease of the magnetic field due to the larger coil diameter, a magnetic yoke composed of a lamination of oriented silicon steel (0.35 mm thick) was covered on the solenoid coil. With this yoke, the resultant magnetic field was almost the same. In this modification the bridge coil was covered only by one-third due to the space limitation of a water cooling pipe. A more complete coil is now under design. The resultant distance between the target and the accelerator guide was shortened from 230 mm to 123 mm. In test operations, it was found that this modified source produced the same amount of positrons as before so the initial purpose of the modification was successfully achieved.

5. High gradient acceleration by recirculator

High gradient acceleration was tentatively attempted by using a conventional short accelerator guide and a waveguide recirculating the microwave power. In this trial an acceleration gain of 18.2 MeV using rf power of 26 MW was achieved. The average accelerating electric field was estimated to be about 60 MV/m.

5.1 The recirculating accelerator structure

This system consists of an accelerator guide, and some waveguides with an input directional coupler. When the rf power is fed to the system through the directional coupler and then the rf wave circulates periodically in the system, the power is accumulated gradually and increases the amplitude of the forward wave in the guide. To resonate in this ring it is necessary to have a proper phase relation along the ring. This is achieved by adjusting the total length by putting in a spacer. The layout of the system is shown in Fig. 5.1 and the details of the accelerator guide are shown in Fig. 5.2.

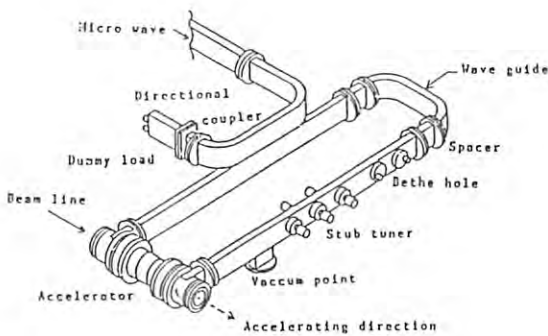


Fig. 5.1 High gradient acceleration system of recirculator type.

For making a compact accelerator practical, both a high accelerating field and large energy gain are necessary. Under the limitation of a

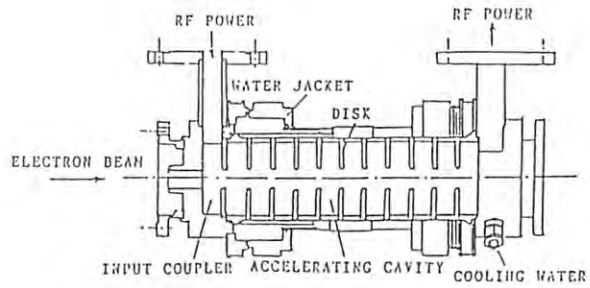


Fig. 5.2 Crosssection of the traveling wave diskloaded accelerator guide of the $\pi/2$ phase shift type.

constant power, the increase of a electric field leads to the decrease of energy gain. Under the limitation of a constant rf pulse width, the increase of the accumulated accelerating field requires shortening of the filling time of the accelerator guide. This is realized by using the short accelerator guide. On the other hand, if it is required to increase the energy gain, it is necessary to make the accelerator guide long. For satisfying of these contradictory requirements, it is necessary for the accelerator guide to have such characteristics as a high shunt impedance and a high group velocity. The accelerator guide in this experiment is designed with a $\pi/2$ phase shift mode so it has the highest group velocity and a comparatively high shunt impedance. Specifications and parameters of the accelerator guide are shown in Table 5.1. The energy gain and the accelerating field strength when 25 MW rf power is supplied are shown in Table 5.2.

Table 5.1 Specification of acceleration system Accelerator guide

Type	constant impedance
Phase shift	$\pi/2$
Operating frequency (Mhz)	2856
Accelerating cavity	13
Length of accelerator guide (cm)	30.4
Aperture of diskhole (mm)	20.0
Shunt impedance (Mohm/m)	50.0
Group velocity (Vg/c)	0.0098
Factor of merit Q	11000
Field attenuation (neper/m)	0.277
Power attenuation (dB)	0.822
Filling time (nS)	116.1
Recirculator	
Total length of waveguide (m)	2.9
Power attenuation of waveguide (dB)	0.06
Total power attenuation (dB)	0.882
Field coupling factor for directional coupler (dB)	14.7
Power amplitude (dB)	7.35
Recirculating time (nS)	130.2

Table 5.2 Specification for energy gain and accelerating field strength

supplying power (MW)	25.0
Energy gain (MeV)	19.0
Accelerating field strength (MV/m)	58.5

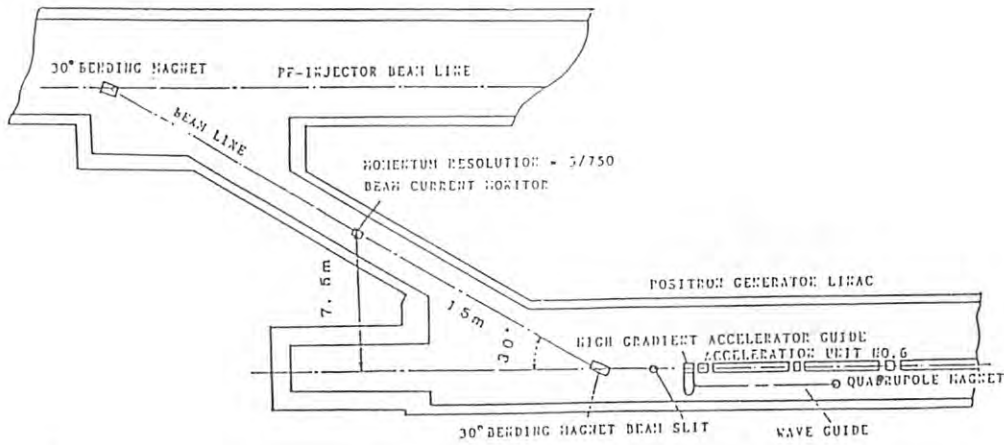


Fig. 5.3 Layout of the high gradient acceleration experiment.

5.2 Test of the high gradient acceleration

The high gradient acceleration system was set at the end of the positron generator and the microwave power to this system was fed through a waveguide from a RF source (P6 unit klystron). The test arrangement of the high gradient acceleration system is shown in Fig. 5.3.

The electron beam in this test was a short pulse of 4 nsec and a beam current of 2.2 A. The energy spectrum of the accelerated electron beam was measured by a bending magnet downstream. To increase the measuring accuracy, both the energy spectrum of the electron beam in the accelerating phase and in the decelerating phase were measured. The energy gain of the accelerator guide was determined by half of the measured energy difference. The accelerating field gradient in the guide was calculated by the energy gain and the available length of the guide. The energy gain of the guide is measured three times corresponding to each different rf power. Figures 5.4(a), (b) and (c) are the energy spectrum for the rf power of 18, 24 and 26 MW respectively. Figure 5.5 is a photograph of the output signal of a directional coupler attached to the waveguide of the recirculation

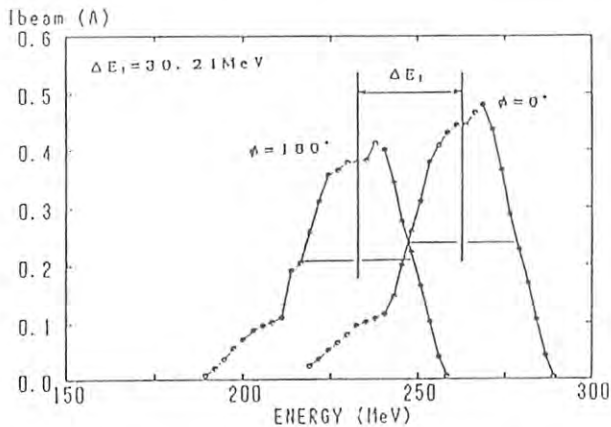


Fig. 5.4(a) Energy spectrum of accelerating electron beam at the given rf power of 18 MW.

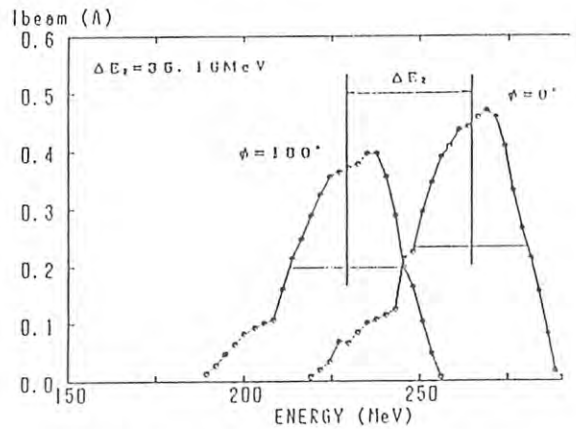


Fig. 5.4(b) Energy spectrum of accelerating electron beam at the given rf power of 22 MW.

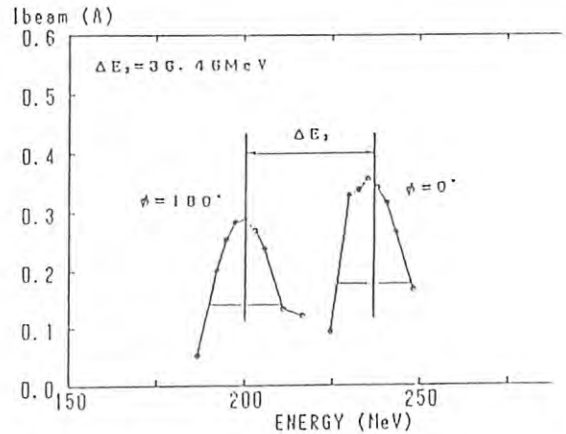


Fig. 5.4(c) Energy spectrum of accelerating electron beam at the given rf power of 26 MW.

ring. This signal shows the build-up of the traveling rf power waveform circulating in the ring. The energy gain and other parameters obtained by this test are summarized in Table 5.3. The accelerating field gradient on the accelerator axis (E_f) and the circulating power (P_a) was calculated as follows,

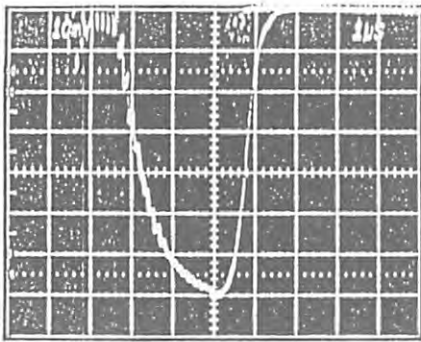


Fig. 5.5 Pulse shape of the traveling wave in the recirculator system. When rf power was supplied about 26 MW, total circulating rf power was about 134 MW and the rounding number is observed about 17 turns.

Table 5.3 Comparison with energy gains and experimental data

Exp.No	Pk (MW)	Pac (MW)	Eac (MeV)	Ef (MV/m)	Eacx/Eacl	(Pkx/Pk1) ^{1/2}
1	18	91.8	15.11	50.35	1.000	1.000
2	24	124.2	17.58	58.60	1.164	1.155
3	26	133.7	18.23	60.77	1.207	1.202

Pk; rf power from klystron
 Pac; circulating power in the system
 Eac; energy gain of the accelerating guide in the system
 Ef; accelerating field on axis in the accelerating field strength

$$Ef(MV/m) = 5.27 Pa \frac{1}{2}$$

From this result, the energy gain and the accelerating field gradient was in fairly good agreement with the design value. The available length of the accelerator guide is estimated to be 30 cm because the input and output cavities of the accelerator guide are off-tuned due to manufacturing trouble. The measured energy spectrum was broad as shown in Fig. 5.4. The reason for this is considered to be that the beam bunch width was too wide due to insufficient adjustment of the prebuncher and buncher, and the beam slit of the energy analyzer opened too wide. This experiment gave the first tentative data for the high gradient acceleration. There were many problems to be improved such as the miss-adjustment of the input and output couplers, a vacuum leak, an insufficient conditioning etc.. In near future, a test using an improved accelerator will be performed.

6. The microwave source

6.1 Operational status

In the period between August 1986 and July 1987, the microwave system has been stably operated with a total operating time of about 4,200 hours.

The high-power klystron modulators have operated stably except for a few problems. In this period, all of the TRIGII thyratrons were replaced with SCR's. Some of them produced a trigger pulse with a large jitter, therefore the circuit parameters of the SCR's input were checked and changed to the proper value. They have been working satisfactory so far. The circuits of the sample/hold units were modified to work normally under a large noise level. This is very important because these units produces interlock signals by detecting the klystron arcing status. In this period 25 PFN capacitors of the improved type were tentatively manufactured and have been tested. A further program to improve the PFN capacitors is being developed.

Twenty-three microwave ceramic windows of the waveguide system were replaced by new TiN coated windows in this period.

Fourteen high-power klystron assemblies were replaced during this period. The details are as follows: One of them was replaced because of problem with a filament transformer in the pulse transformer assembly. The others were klystron failures. One of them was the failure due to the emission degradation and the others (12 tubes) were internal arcing.

Table 6.1 shows the operational performance of the tubes during the past six years (up to the July 1987). One hundred and two tubes have been used since 1982. Fifty-two tubes failed during these periods and their MTBF (Mean Time Before Failures) was 13,600 h. The mean age of living tubes is 4,400 h.

Table 6.1 Cumulative usage hours during the past 6 years

Period	Total Tubes	Failed Tubes		Living Tubes		MTBF
		No.	Mean Age (h)	No.	Mean Age (h)	
1982/4 - 1983/3	53	11	1,300	42	2,900	12,500
1983/4 - 1984/3	63	20	2,300	43	4,200	11,200
1984/4 - 1985/3	70	25	3,100	45	5,800	13,600
1985/4 - 1986/3	77	32	4,000	45	7,500	14,400
1986/4 - 1987/3	93	47	4,300	50	8,600	13,400
1987/4 - 1987/7	102	52	4,400	50	9,600	13,600

Table 6.2 shows a more detailed analysis of the operational status corresponding to the respective tube production years. This table also shows that the main causes of the tube failures were internal arcing and window puncturing. In this period it was predominant that the rather new tubes, i. e., ones of product years of 1985 and 1986, failed due to internal arcing. The failures happened suddenly after the HV operating hours reached between 1,500 h and 2,000 h inspite that the initial operating status were fairly good. These tubes were all manufactured using a new vacuum furnace in the factory process. The causes of the failures are not clear up to now and the efforts to solve them are under way.

An important factor concerning linac operation is the klystron fault rate, since the faults lead to interruptions of beam injection into the PF ring or the TRISTAN accumulation

ring. Table 6.2 also shows the fault rate corresponding to each production year. Table 6.3 shows the fault rates and the applied voltages from October 1982 to July 1987.

The development of an impregnated cathode has been continued this year. Three barium scandate cathodes were purchased this year to install them to the klystrons. They have been used for cathodes of the 50 MW high power pulsed klystrons in SLAC and it was reported that their performances were satisfactory. Manufacturing the tubes using them will be planned in November 1987. Development of a domestic impregnated cathode has been continued. Main features of the development are as follows; (1) Hi-potting of the alumina ceramic in a filament wire was studied and improved. (2) Non-inductive winding of a filament wire was established. (3) Thermal shielding of a cathode was improved. The results of tube performance using them will be obtained in next period.

Table 6.3 Klystron fault rate data

Period		Fault rate (per hour per 41 tubes)	Averaged applied Voltage (kV)
Year	Month		
1982	10 - 12	3.5	236
1983	1 - 3	4.4	238
	5 - 7	4.6	239
	10 - 12	3.3	241
1984	1 - 3	2.6	243
	5 - 7	2.4	242
	10 - 12	2.6	241
1985	1 - 3	2.1	239
	5 - 7	1.5	241
	10 - 12	1.6	238
1986	1 - 3	1.6	237
	5 - 7	1.9	240
	10 - 12	1.9	241
1987	1 - 3	1.2	240
	5 - 7	1.9	236

6.2 Phase control

The KEK linac has an automatic system which controls phases of the klystrons in order to maximize beam energy and to minimize momentum spread. The software for this phasing system was improved, so that execution time of the phasing was reduced and drifts of the phases can be measured anytime according to request.

Phase stabilization of the rf components is also important to maintain stable beam of the linac during long-term operation. For the first time a phase locked loop (PLL) technique was introduced into the main-booster amplifier and the SHB amplifier in order to reduce phase drifts.

Automatic phasing

The automatic phasing is executed based on the beam induction method, which measures the phase difference between the beam induced wave and the acceleration rf by a phase detector. As a matter of fact the phase difference cannot be known directly, so a cw reference wave is required for the phase comparison between both rf waves.

The linac has 6 phasing units which control all of the klystron phase shifters divided into 6 sectors. The phasing system consists of a phasing unit, which has a phase detector and a phase shifter for the reference rf wave, and a phasing unit controller connected with a personal computer.

The procedure for the automatic phasing is installed in the computer and written in BASIC language in order to enable easy improvement of the program. The present automatic phasing has the following three modes;

- (1) Normal phasing: The procedure is started with adjustment of the reference phase shifter as the phase difference between the beam-induced wave from a selected acceleration guide and the reference rf one becomes $\pm 90^\circ$. Then the relative phase of beam can be known. The phase shifter for the

Table 6.2 Status corresponding to the year of production. "Standby" tubes are those waiting for retesting. "Unused" tubes are those which have not been used in the klystron gallery at all.

Year	No. of Total Tubes	Living Tube				Fault rate perday	Voltage (kV)	Failed Tubes			Mean Age (h)		MTBF	
		No. of Working Tubes		No. of Nonworking Tubes				No. of Total Tubes	Cause		Failed Tubes	Living Tubes		
		PF	Positron	Standby	Unused				Arcing	Window				Others
1979	4	0	0	0	0	—	—	4	2	1	1	3902	0	3902
1980	20	5	0	1	0	1.5	240	14	7	5	2	4672	14682	10965
1981	20	9	0	1	0	0.8	243	10	6	2	2	4663	15948	20611
1982	9	2	0	1	0	0.8	247	6	5	1	0	5785	10464	11017
1983	13	8	2	0	0	1.4	241	3	3	0	0	6019	11464	44232
1984	13	1	3	0	2	0.5	262	7	7	0	0	3971	7011	7978
1985	12	7	0	0	1	1.2	240	4	4	0	0	3349	5354	12718
1986	14	9	1	0	0	1.9	234	4	4	0	0	1388	2212	6918

related klystron is adjusted as the phase of the acceleration rf is $\pm 90^\circ$ away from the phase of the reference one. After the adjustment, the accelerating wave has a complete reverse phase compared with the beam-induced one and this means that beam bunches are exactly on the crests of the accelerating rf waves.

(2) Easy phasing: The reference phase shifter is adjusted without measurement of the phase signal at the value which was memorized at the past phasing in mode (1). The phase adjustment of the acceleration wave, however, is executed according to the same way in mode (1).

(3) Phase drift measurement: In mode (2) phasing the last adjustment of the klystron phase shifter is not carried out but the phase drift is estimated from the output signal of the phase detector.

The mode (1) phasing is usually requested at the start of the linac operation for accurate phasing. But it should be noticed that a long pulse ($> 0.6 \mu\text{s}$) beam is indispensable to get a strong enough phase signal of the beam-induced wave. The adjusting time for one klystron is less than one minute and almost of the time is spent for rotating the both phase shifters. Mode (2) is useful to compensate phase shifts of the klystron rf caused by a change of the klystron applied voltage for example. The adjustment is completed within 30 sec in this mode. An advantage of this phasing is that a beam-induced wave is not necessary, so that the phasing is executable at anytime even during injection of a short pulse beam into a ring. Mode (3) is prepared for watching phase drifts of the klystrons and is helpful for judging whether phasing should be requested.

The phasing error is evaluated within about $\pm 3^\circ$ after the phasing.

Phase Stabilization

Since the SHB system for the positron generator had unacceptable phase drift over a long term, a phase stabilizing system was required to get a stable beam and good reliability. This time PLL feedback systems were introduced into the SHB amplifier and also into the main-booster.

The block diagram of the system for the SHB is illustrated in Fig. 6.1. The source of phase drift is not only the amplifier but also a transmission line or the SHB cavity, so the phase detector compares the pulsed rf signal (50 pps) picked up at the cavity with the 119-MHz cw input rf and outputs the phase error signal into the next sample hold amplifier. The amplifier generates a very slow compensation signal through an integration circuit and controls a solid state phase shifter to zero the phase error. The time constant of the circuit is adjusted at about 4 sec to prevent a self-excited oscillation of the feedback system, but this also limits response time against rapid drift. Figure 6.2 indicates that the PLL system is

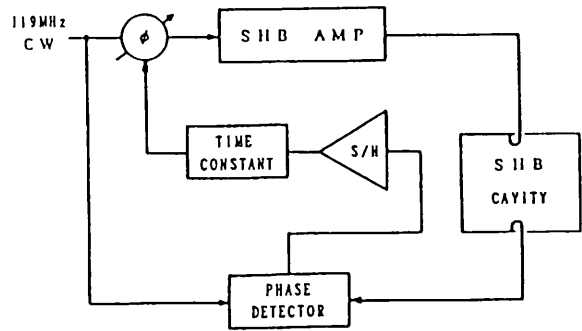


Fig. 6.1 PLL for the SHB amplifier.

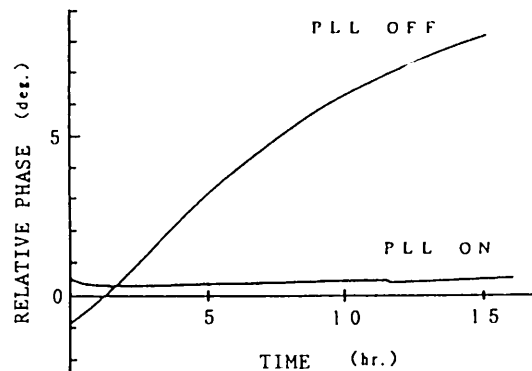


Fig. 6.2 Phase variation of the SHB amplifier.

effective enough for the reduction of phase drift.

The PLL system for the main-booster has more simple construction without a sample/hold circuit because the compared two rf signals are both cw. The phase error of the total system is evaluated at less than $\pm 0.2^\circ$ and the response time is about 40 msec.

7. Control system

7.1 Display system for control console

The control system for the PF 2.5 GeV electron linac, which was based on a distributed computer system interconnected through a network, has been used since 1987. In this system, CAMAC modules were used as CRT drivers for the operator's console. The CRT drivers have been upgraded as shown in Table 7.1. Recently new needs were required since many programs had been developed for console display: faster and more intelligent display, better program developed environment, etc.. To meet these requirements a new display system shown in Fig. 7.1 was introduced: personal computers interconnected via a local area network (DS-Link). It was strictly taken into account that this new network system should be capable of executing most of the application programs already developed.

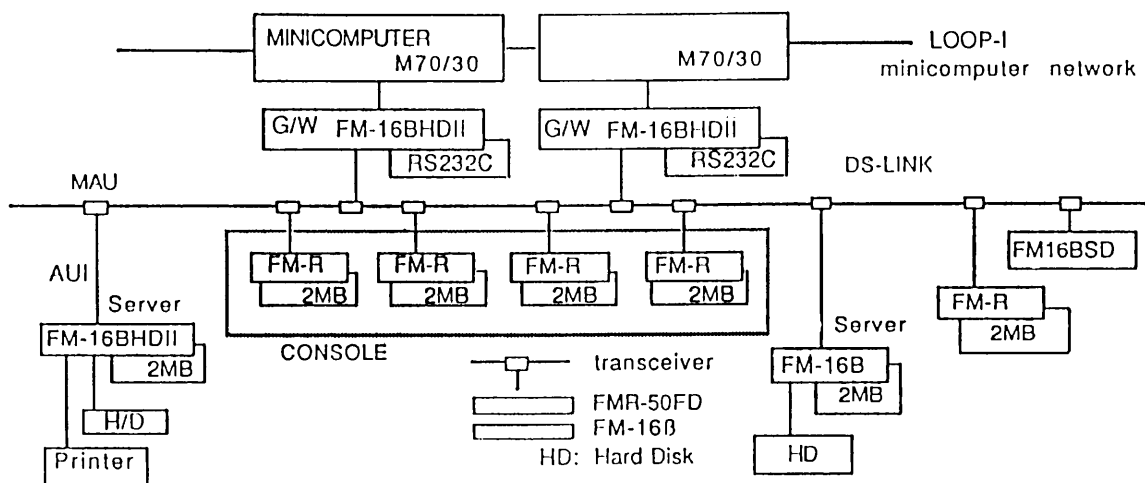


Fig. 7.1 Console display system.

System Description

As shown in Fig. 7.1, the console display system is composed of several microcomputers which are connected to the DS-Link network. The system receives linac device data from the center minicomputers and processes them for display.

The system consists of gateways (G/W), file servers, workstations (WS), coaxial cable, and transceivers. The operator's console has four 20 inch CRT's for display with transparent touch panels. Most of the information about the linac status are displayed on them except for picture of screen monitors and some others. The touch panel (TP) is a device of a resistive plate type and used to input operator's commands. It is Elographics Co. made. Touch panel controllers (NPV 6800) were laboratory made and have been used without any trouble. Response time of the TP (from touching by a finger to picture changing) is almost determined by firmware. So as to get more quick response when the TP is touched, the firmware built in the TP controller was upgraded; its response time was changed from 350 ms to 150 ms.

The FMR-50 has a 512 kB VRAM (2 color screens), 80286 CPU, 1 MB main memory and optional 2 MB. It supports HG (High grade) BASIC, C, and assembler under MS/DOS V3.1 L20a.

DS-Link (Local Area Network)

The DS-Link is a baseband local area network for communication between microcomputers. It is made by FUJITSU on the basis of the Ethernet (Xerox) and MS-network. It consists of a transceiver controller, two file servers, a print server, and workstations. Collision detection and recovery during normal operation is unnecessary. The protocol admits server-remote and remote-remote communication in full-duplex.

The features of Ethernet are well known as follows:

- (1) Coaxial cable bus and transceiver are easy to install.
- (2) Flexibility is good.
- (3) The effective communication speed becomes slow when traffic is heavy.
- (4) System trouble in any workstation does not affect the others.

Gateway

A personal computer is used as a gateway for communication between the host (LMCOM 70/30) and a remote node or nodes in the console display system. Messages from the microcomputer is distributed over the entire nodes or a selected node of which a flag is set. The gateway provides the following functions:

- (1) protocol conversion (MELCOM 70 - DS-Link)
- (2) mailing, broad cast (G/W - any WS)
- (3) data processing

A compiler language is used in the gateway.

Server

The file server is very important in this system. Graphics data, operational information, control programs and linac device data file are all stored in the 2MB RAM disk or 60MB Hard Disk of the server. These files are called as common files and available at random from every workstation, but only operation programs are protected against rewriting. The system provides two servers and printers.

Workstations for Console Display, Maintenance & Development

There are four 20 inch color CRT's on the

console which have been used since 1982. The workstations are connected to these CRT's and the touch panels. The touch position on the touch panel is sent from its controller to the associated workstation through an RS232C interface (4800 baud).

Each workstation is able to receive data selected from G/W by setting a corresponding flag. Operator's commands can be input by the TP only; there is no keyboard on the operator's console. Since each workstation of the console has a 2MB optional RAM on which most of the programs reside, programs do not have to be reloaded every time. Their execution can be initiated quickly.

There are several workstations for program development and maintenance; they are distributed in different rooms and connected to the DS-Link. They are always accessible by any programmer even when the accelerator is running.

Software

Workstation : The interpreter language is useful for development. Each application program is made as a subprogram and the size is almost under 9 k bytes. Basic and machine language modules are used on the workstation.

Gateway : At the first stage Basic and assembler were used for developing programs. Each function was tested and then converted to a compiler language (C and assembler language) for improving the executing speed. One of the programs and data file configurations is shown in Fig. 7.2 and Fig. 7.3.

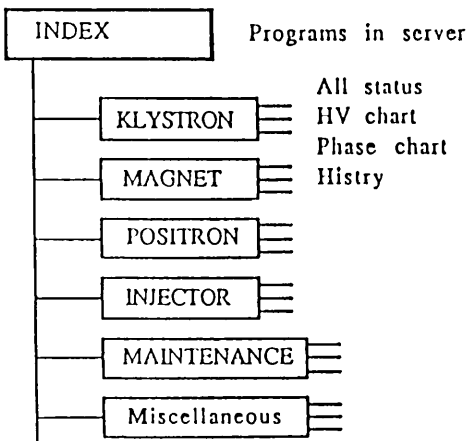


Fig. 7.2 Common program file in server.

7.2 Monitoring system for klystron RF outputs

In order to improve stability of an accelerator, characteristics of active components must be improved. For an electron linac these are electron guns, beam transport magnets and klystrons. Among them klystrons tend to lose their stability because of their complexity.

So far in the KEK electron/positron linac an operator surveys RF output one by one with an

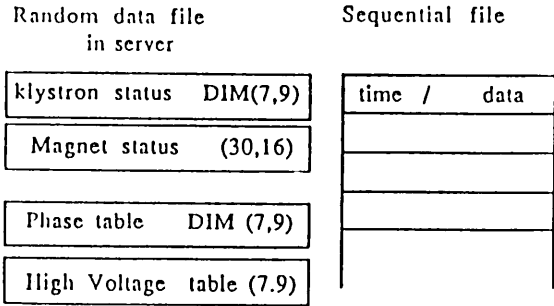


Fig. 7.3 Data file which are stored in server.

oscilloscope on the operator's console. It is difficult however to detect long term stability or small fluctuations. So it is needed to build a computerized monitoring system of the RF output from klystrons for early diagnosis.

The control system of the KEK electron/positron linac is composed of two console stations, seven sub-stations, many device controllers and network system among them. The RF monitoring system works on three sub-stations, each of which monitors 16 klystrons. The network system is used for communications of monitoring data and warning messages.

Each RF output is taken from the directional coupler at the end of an accelerator tube through a wave detector. This is the common source for this monitoring system, the operator's monitoring oscilloscope and the automatic phasing controller. Isolators and buffer amplifiers are employed to avoid cross talk.

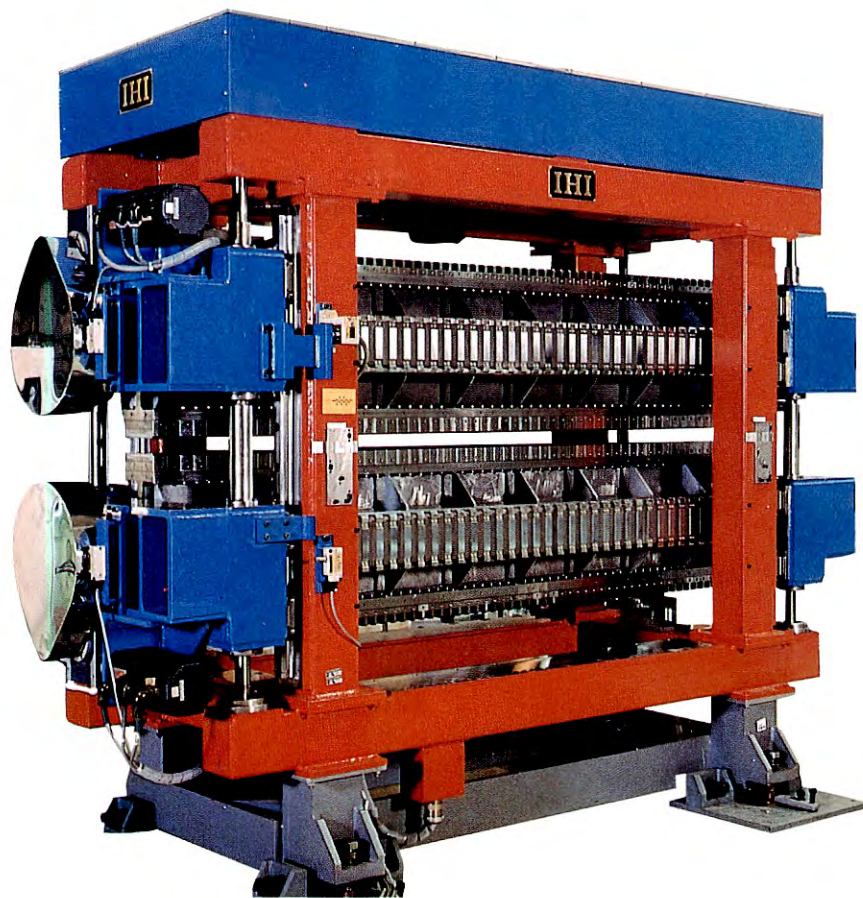
The RF wave forms are digitized by transient digitizers (Tektronix 390AD) and processed by sub-control-stations (MELCOM70/30) through GPIB interfaces. The sampling frequency and number of data points are chosen to be 10 MHz and 512 points (51 μ s). Analog multiplexers select one of 16 RF outputs. In order to reduce noise from RF switching modulators, low pass filters and 20 dB buffer amplifiers are inserted.

The monitoring system checks stability of RF outputs. The standard deviation of raw data are examined against a reference. This method is sensitive to noise and it is difficult to tell how raw data changes if the standard deviation is large. So the computer program is coded to compare the representative values such as position, height, width and area of the RF wave form.

If the ratio of these values to a reference exceeds some extent, a warning message is sent to the console station. This message is displayed on the operator's console and recorded on a printer and disk file.

It is suggested that small fluctuations of RF output means the end of the life span for the klystron. So this monitoring system is important for an early diagnosis of the RF system and the accelerator.

Light Source Department



ISSP-KEK Revolver (Multi undulator)

The period lengths of the four magnet arrays are 5 cm (93 poles, $K_{max}=1.3$), 7.2 cm (65 poles, $K_{max}=2.7$), 10 cm (47 poles, $K_{max}=5.0$) and 16.4 cm (29 poles, $K_{max}=9.3$).

1. INTRODUCTION

The 2.5 GeV electron storage ring constructed at the Photon Factory, KEK, is fully dedicated to the research work with synchrotron radiation. The ring was commissioned in March, 1982, and since then it has been operated quite stably for over five years. The principal parameters of the ring are listed in Table 1.1.

The highlight of the ring in FY 1986 was the successful ring operation in the low emittance mode. During the summer shutdown in 1986, four newly fabricated quadrupole magnets were installed into the ring and four power supplies which excited twenty four quadrupole magnets were reinforced. On February 3, 1987, the operation in the low emittance mode was started. The betatron numbers were adjusted, so that the number in the horizontal direction was changed to 8.38 from the old value of 5.38 and, in the vertical direction, to 3.14 from 4.18. The betatron functions were also measured and adjusted. The horizontal emittance was reduced to 130 nm·rad. from the old value of 400 nm·rad. The brilliance of SR was expected to increase 2 ~ 20 times depending on each beam channel.

Since February 1986, we had continuously measured the position of the light axis at the point 12 m away from the light source in beam line No.21. To our surprise, the light axis suddenly began to move violently after the low emittance mode started. The short term deviation was about 0.15 mm, however, the long term shift which had one day period reached 1 mm. Some users asked that the low emittance operation be stopped. Then, the ring was again operated in the normal emittance for one week. During this week, the light source group had prepared a feedback system to stabilize the closed orbit, details of which are described later. The feedback system functioned well enough to satisfy the user's requirement. Since then, the ring has been operated in the low emittance mode.

An interesting vacuum problem occurred in

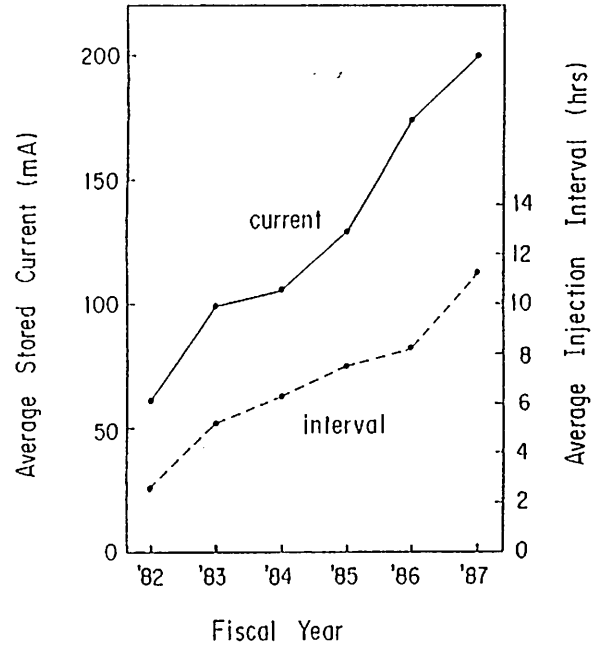


Fig. 1 The average stored current and the average injection interval during user time

September 1986. During the summer shutdown, several parts of the vacuum chamber had been improved for installing four quadrupole magnets as previously described. After the improvement was completed, the vacuum was again evacuated. But the one side of the chamber opening was not connected to the gate valve and covered with a cap made of polyethylene, so that the cap was sucked into the chamber and ran through for 40 meters. To take out polyethylene fragments and powder from the chamber, the chamber wall was cleaned with a vacuum cleaner. Again the chamber was evacuated. After forty hours baking at the

Table 1.1 Principal parameters of the storage ring

Energy	2.5 GeV Achieved; 1.6 GeV ~ 3.0 GeV
Initial stored current	300 mA 250 mA with wiggler. Maximum achieved 360 mA.
Bending magnet	28 Radius of curvature 8.66 m. Circumference 187 m.
Other magnets	Quadrupole 58, Sextupole 22, Octupole 8, Skew 6, Vertical steering 42.
Betatron frequency	Horizontal 5.38 + 8.38*. Vertical 4.18 + 3.14.
Emittance	Horizontal 400 + 130* nm·rad. Vertical 6 + 2* nm·rad.
RF acceleration system	Frequency 500 MHz. Harmonic number 312. Single cell cavity 4. Klystron(160 kW) 2. Radiation loss 400 keV/Turn.
Injection	Linac 2.5 GeV. Repetition rate 1 Hz. Beam storing rate 0.5 ~ 3 mA/sec.
Vacuum pressure	No beam 3×10^{-11} torr. 150 mA operation 4×10^{-10} torr.
Beam lifetime	15 hrs at I=300 mA. 30 hrs at I=150 mA.
Insertion devices	Superconducting vertical wiggler 5T 60 period undulator K=1.78 ~ 0.1 26 period multipole wiggler/undulator 1.5 T ~ 0.04 T Four way revolver type undulator (under testing) 14 period multipole wiggler (under construction) Circular polarized undulator (in construction)
SR Channel	SR experiment 20 (4 under construction) Beam diagnosis 3

* : in the low emittance mode of operation

temperature of 150°C , the vacuum pressure went down to 2×10^{-11} torr. On October 14, the ring operation for cleaning up the vacuum chamber started. It took 120 hours to get a good vacuum of 8×10^{-9} torr at the stored current of 150 mA and the time-integrated stored current was 16 ampere hours. The user's run were than started.

Though the vacuum pressure was not so bad, deterioration of the beam lifetime occurred frequently. Using lead glass γ -ray detectors, we had observed bremsstrahlung at two points, which was generated by collisions between stored electrons and residual gases or other things. One point A was the place just downstream where the polyethylene cap ran and stopped. Another point B was thirty meters downstream from point A. Every γ -ray burst at point A was accompanied by deterioration of the beam lifetime. Every γ -ray burst at point B was coincident with that at point A and the yield of the burst at point B was much smaller than that at point A. These facts suggested to us that polyethylene dust from the wall of the vacuum chamber is irradiated by synchrotron radiation to be heavily positively charged by ejecting many photoelectrons and is trapped into the electron beam. The trapped dust received a force caused by E cross B fields in a bending magnet and drifts along electron beams. When trapped dust runs into the next bending magnet, some of them is reflected by the E cross B fields depending on the initial condition of its motion. Details are described later.

2. STORAGE RING

2.1 OPERATION

During FY 1986, the storage ring was operated for 3076 hours. Normally, the ring operation was in the two weeks mode, that is, the ring was operated from Wednesday morning through Saturday morning of the following week. After the successful operation of the TRISTAN Main Ring in November, 1986, the PF ring operation became irregular, because the injector linac has to supply electrons and positrons to the TRISTAN Ring for a longer term. Because of this, a three- or four-week mode of the PF ring operation was started.

The average stored current during the user time has been increasing year by year as is seen in Fig. 1, and now it is 200 mA which is 3.3 times larger than that in FY 1983. Until summer 1985, the initial current was limited to 150 mA, because a part of the water cooling system of the vacuum chamber was not satisfactory. Now the initial current is 300 mA when the wiggler is not in operation and is 250 mA during the wiggler operation. The limitation is due to the lack of RF power. The average injection interval during the user time has been also increasing. Now it exceeds over 11 hours. This progress was mainly attributed to improvement of the ring vacuum system.

The user time percentage of the total ring time has increased to 79 % for the injector linac, the PF ring. The TRISTAN accumulation ring which has its own time is 10 % of the total ring time and is used for machine studies.

During the linac study time, the ring can maintain its stored current without any reinjection for one day long and supplied SR to users.

Though the machine failure time is about 1 % of the scheduled user time, it took much more time for the injection when the vertical wiggler was operating. The wiggler has super-conducting coils with a narrow magnetic gap, so that the wiggler operation must take many complex procedures before and after reinjections. As the result, the effective user time remained 90 % of the scheduled user time.

2.2 LOW EMITTANCE OPERATION

At the early stage of the construction of the PF-RING, four alternatives of the optics including a low-emittance configuration had been designed⁽¹⁾. However, the optics used in operation until recently was almost the same as the one used for the ring commissioning, except the small changes in tunes. The venerable operation with this optics is called the normal-emittance mode. Because of financial defect, the ring was unable to operate in any other mode, which demanded to reinforce the power supplies of the ring quads.

After enjoying a comfortable optical configuration with a rather high emittance for several years, the ring was prepared to test a new low-emittance mode⁽²⁾ through fiscal year 1986 without cutting down the user time, in order to respond to the increasing demand for higher brilliance.

The outline of the PR-RING is shown in Fig. 2.2.1 with four additional quads named "QA" that are needed to obtain a new optics with an emittance of about one third of the normal-emittance. The low emittance is attained by increasing the horizontal phase-advance in a normal cell from $\pi/2$ to $4\pi/5$, and by making up the triplet sections together with two bends into achromatic ones; these sections are near the centers of the insertion sections. In addition, to get a good optical matching between the end of the normal-cell section and the insertion section, it was necessary to add a new quad in-between. With the additional quads, we can decrease the β -functions at the RF- and VW-sections, and also make these sections dispersionless.

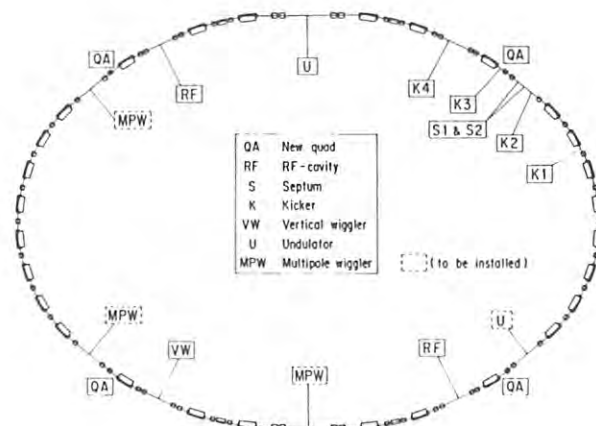


Fig. 2.2.1 Outline of the PF-RING.

Smaller β -functions at the RF-sections are generally desirable to avoid transverse instabilities due to the higher modes of cavities. In the PF RING two horizontal transverse were found to be dangerous, so that the smaller the horizontal β -function in RF-section is, the more beam current we could get. A smaller β -function is also desirable at the VW, the vertical superconducting wiggler with a strength of 5 T and a narrow horizontal gap, in order to reduce their influence on the orbit parameters. On the other hand, the space available to a kicker called K3 was found to be insufficient for the old air-core kicker. It was then decided that the kicker should be replaced with a smaller ferrite-core kicker.

The principal parameters of the new low-emittance optics are listed in Table 2.2.1 and compared with the parameters of the normal-emittance mode. Figure 2.2.2 shows the β - and η -functions in one quadrant of the ring as well as the beam sizes for the new optics. The horizontal β -function at the RF- and VW-sections for the new optics is shown in Fig. 2.2.3 along with those for some other optics. As seen in the figure, the β -function is much smaller than that of the old low-emittance option, but still larger than the β -function of the normal-emittance mode. Therefore the transverse instabilities were anticipated to become more troublesome. However, this problem have been almost resolved by installing damping antennas in the RF-cavities. The brilliances were expected to be improved about twenty times at two beam lines, about five to ten times at several ones, and about twice at the others.

The design of the additional quads had to be chosen so as to accommodate the outside of a magnet yoke to one of the existing beam-lines at its place of installation. It turned out that the bore radius of the quads was to be smaller than that of the existing quads, and the outer shape of the magnet yoke to be in a polygonal form rather than a circular one as adopted for the existing quads. The parameters of the new quads are given in Table 2.2.2 and an octant of the magnet pole is shown in Fig. 2.2.4. The end core shimming to get a good integral gradient was empirically determined in much the same way as in the case of the existing ones by attaching rectangular iron blocks to the end core. A part of the results of the field measurement are shown in Fig. 2.2.5. These four new quads were fabricated by HITACHI, Ltd.

Table 2.2.1 Parameters of the low-emittance and the normal-emittance mode.

	normal-emittance	low-emittance
V_x	5.40	8.38
V_y	4.16	3.14
α	0.037	0.015
ζ_x	-6.8	-15.8
ζ_y	-4.7	-8.6
ϵ_x (nm·rad)	404	127
ϵ_y (nm·rad)	~ 6	~ 2
σ_z (cm)	2.1	1.3

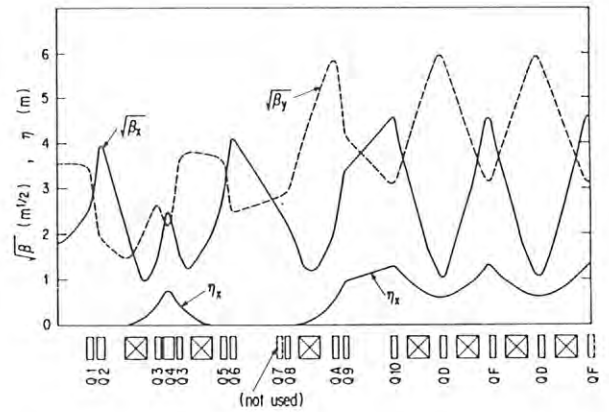


Fig. 2.2.2(a) β - and η -functions in one quadrant.

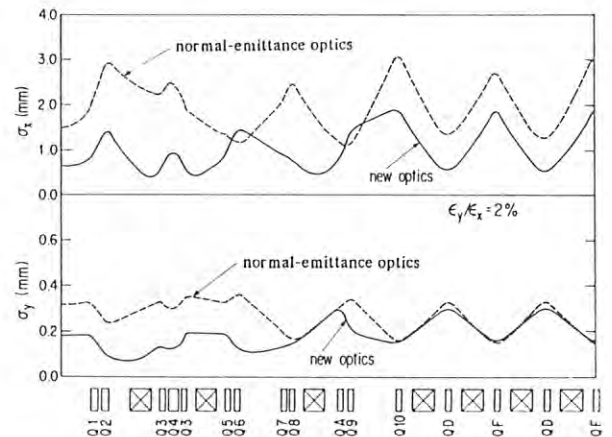


Fig. 2.2.2(b) The beam sizes in one quadrant.

The new quads are excited by adjusting one of the existing transistor-type power supplies. Four new power supplies were purchased from the HITACHI company to increase the currents of some of the existing quads. Further, the other three power supplies were reinforced and adjusted to drive some other quad-currents needed for realization of the new optics. The rearrangement of the cablings between the power supplies and the quads families was also made. It is possible to resume its original arrangement quickly. All existing power supplies as well as the ring bend

Table 2.2.2 Parameters of the new quads.

Bore diameter	104 (mm)
Core length	0.5 (m)
Field gradient (B'1)	41.6 (max. 88.0) (kG)
Current	300 (max. 800) (A)
Turn number per pole	26
Resistance	37 (mΩ)
Max. power dissipation	24 (kW)
Water flow rate	2.4 (l/min)

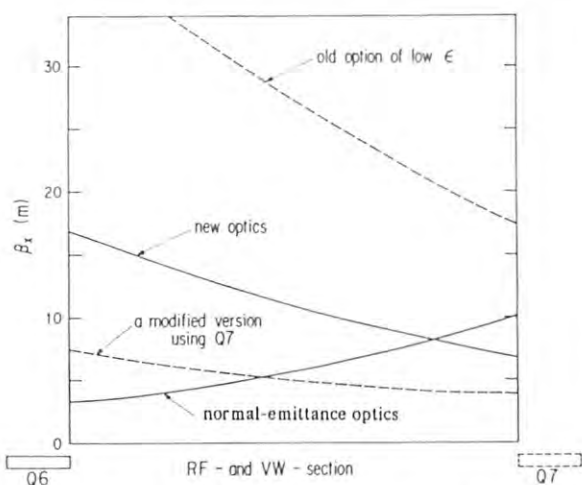


Fig. 2.2.3 Horizontal β -function at the RF- and VW-section.

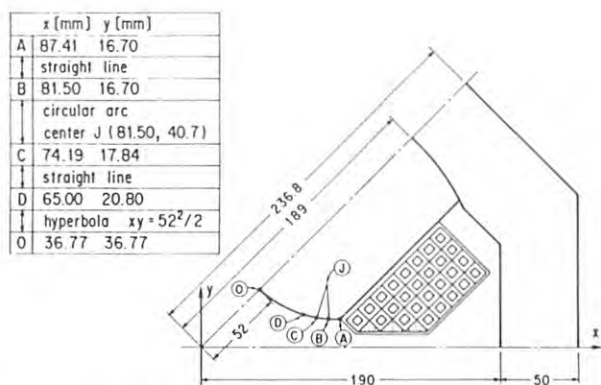


Fig. 2.2.4 An octant of the new quad.

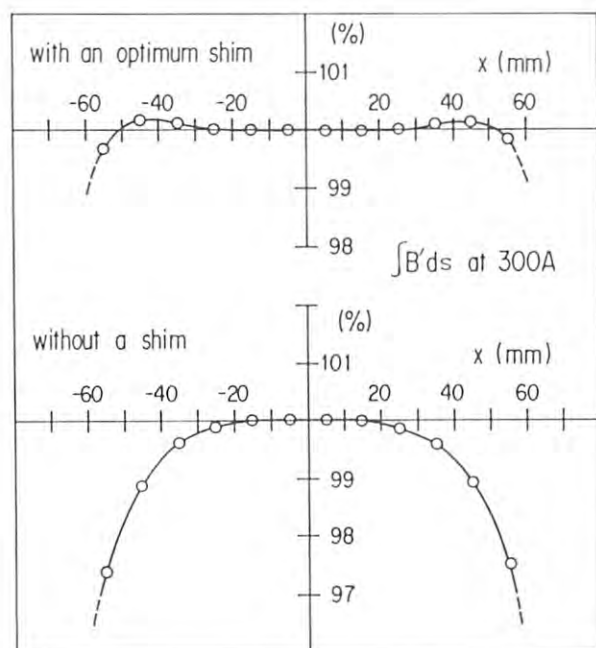


Fig. 2.2.5 Measurement of the magnetic field of a new quad.

power supply have employed transistors into the power regulation circuits. Because of somewhat large powers and also from an economical consideration, four new power supplies were decided to be made up with thyristors and active filters; its design is based on the power supplies of the TRISTAN Main Ring.

In addition, many other improvements were indispensable for commissioning of the new optics; the installation of RF damping antennas, the replacement of an air-core kicker with a new ferrite-core kicker and the installation of a ceramic chamber at the kicker, the other replacements of vacuum chambers for the new quads. Further, the undulator with the narrowest gap around the ring was removed for about one month to make the commissioning easy.

As described in Section 1, the commissioning of the low-emittance mode succeeded on February 3, 1987. Soon after setting up the new optical configuration and slightly adjusting the beam-transport line and the ring magnets, we successfully stored the beam in the ring without using any steering magnet. The injection rate attained so far is around 1 mA/sec with the repetition rate of 1 Hz. The distortion of the horizontal and vertical closed orbits were corrected to less than about 1 mm. The fractional parts of the tunes were changed by adjusting two quad families of QF and QD in the normal cells to bring them almost equal to the values for the normal-emittance mode. Thereafter, the β -functions were measured and then the distortions of β -functions were corrected by adjusting all quad families. Thanks to the accumulated experiences and careful studies on the VW and with a sophisticated method of simultaneous correction of tunes and β -functions⁽³⁾, we immediately succeeded in exciting the VW up to 5 T without any appreciable beam loss.

Through the machine studies during the commissioning, we encountered two problems; (1) there are longitudinal instabilities as seen in the normal-emittance mode. However we can store a beam of more than 300 mA without any trouble, since the growth of the beam size is still small. (2) The vertical closed orbit was found to vary almost periodically from day to day with a maximum deviation of 0.6 mm. It was cured by applying a global and digital correction method of closed orbit (called Digital-Feedback). Though there still remains a small deviation in the closed orbit, the users are now enjoying bright synchrotron light from the low-emittance mode.

References

- (1) PHOTON FACTORY Design Handbook, 1979.
- (2) Y. Kamiya and M. Kihara, KEK Internal 85-10, December, 1985.
- (3) M. Katoh, I. Honjo and Y. Kamiya, KEK Report 86-12, March 1987.

2.3 BEAM DYNAMICS

2.3.1 Insertion of Damping Couplers in the RF Cavities

In the low-emittance optics, the beam orbit becomes sensitive to magnet-field errors etc. Furthermore, small beam sizes (both transverse and longitudinal) lead to difficulties in beam-instability suppression, because of a reduction of the Landau-damping effect. For the high-emittance lattice, the cavity-caused instabilities can be avoided or reduced by controlling the cavity temperature (cooling water temperature for each cavity). However, since the low-emittance operation lower the thresholds of such instabilities by a factor of three, they cannot be suppressed by the existing temperature-control system. Therefore, insertion of damping couplers into the accelerating cavities, in order to reduce the impedance of higher-order-mode resonances, was planned and carried out by taking two steps in 1986:

- (1) On July 19, a damping coupler was inserted in cavity#2 (one of the four single-cell cavities in the Ring, which it was the most detrimental for stable operation). Purposes of this insertion were,
 - (i) to know the influence of rf-fields induced by a high-current beam and single-bunch beam, such as discharging, heating and vacuum problems,
 - (ii) to try a new venting system using dry nitrogen-gas and to check the recovery time back to ultra-high vacuum, and
 - (iii) to see suppression of the instabilities. Details of this insertion were described in Activity Report 1986, in which we presented a remarkable effect on the longitudinal instability "758" (TM011-mode).
- (2) On December 20, two couplers were inserted in cavity#1 and #4. Cavity #3 was left without a coupler, since the existing temperature-control system can avoid #3-caused instabilities.

2.3.2 Instability Thresholds for the High-Emittance Operation

The instability thresholds for "758" after inserting the coupler were compared with that of without couplers for the high-emittance optics, as shown in Fig. 2.3.1. No TM011-problems arose below 300 mA at the operating rf-frequencies.

The spectral peaks characterizing the "758" instability disappeared on the spectrum analyzer. However, another sign of a longitudinal instability was recognized, as shown in Fig. 2.3.2. After continued studies of these peaks, we concluded that they resulted from a longitudinal coupled-bunch instability due to the cavity higher-order-mode TM013, whose resonant frequency is 1707 MHz.

This instability, "1707", causes a fluctuation in the horizontal beam size, as shown in Fig. 2.3.3. It behaves quite similar to the

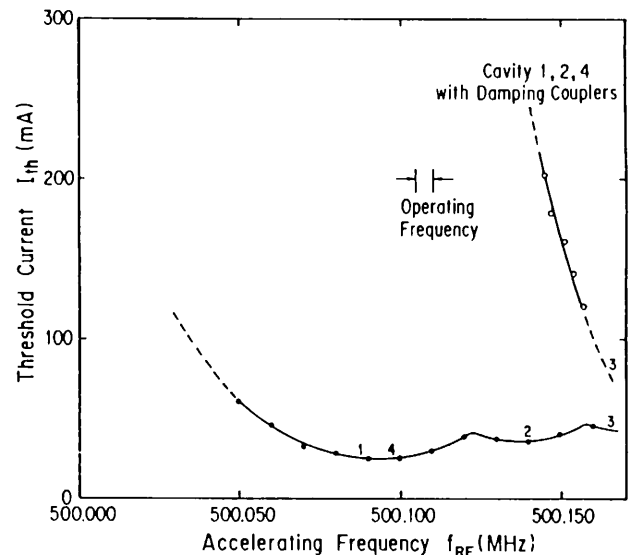


Fig. 2.3.1 Two threshold curves of the longitudinal instability due to the cavity resonance TM011-like mode (758 MHz) for the high-emittance optics, exhibiting a clear effect of the damping couplers. Lower curve is a threshold without damping couplers, and the upper is that after the insertion of couplers into cavities #1, #2 and #4.

Table 2.3.1 Summary of the coupled-bunch instabilities. Observed resonant frequencies, Q-values and coupling impedance of the RF cavity are presented. Units of impedance are $M\Omega$ and $M\Omega/m$ for TMO and TMI modes, respectively.

Cavity mode	Frequency (MHz)	$Q_{exp.}$	R ($M\Omega$ or $M\Omega/m$)	Mode of coupled-bunch	Instability	Problems
"758" TM011-like	758	19,000	3.02	161	Longitudinal	Beam Blowup (H)
"1070" TM111-like	1070	21,000	27±1	268	Horizontal	Beam loss
"830" TM110-like	829	29,000	12±1	103	Horizontal	Beam loss
"1707" TM013-like	1707	50,000	0.85*	129	Longitudinal	Beam Blowup (H)

* Calculation

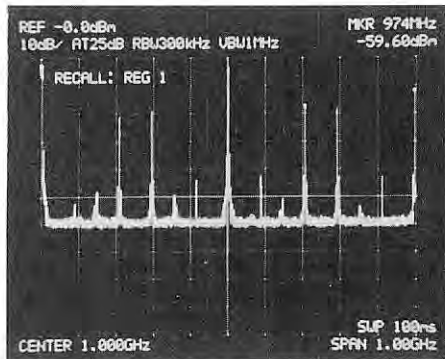


Fig. 2.3.2 An example of the beam spectrum for the newly recognized longitudinal instability at $I = 320.8$ mA and $f_{RF} = 500.080$ MHz. Spectral peaks were assigned as a result of the longitudinal instability due to a cavity mode TM013 at 1707 MHz.

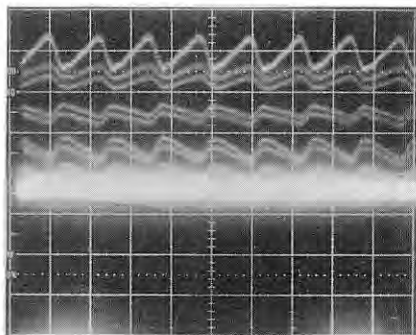


Fig. 2.3.3 A fluctuation in the horizontal beam size taken from the beam profile monitor. $I = 216$ mA. The scan width is 5 ms/division.

instability "758", and that is the reason why "1707" could not be distinguished before the insertion of the damping couplers. The couplers removed "758", but "1707" appeared clearly. Measured threshold currents of "1707" are shown in Fig. 2.3.4, in the high-emittance operation. They depend upon the temperature of cooling water for cavity#3, that is the only the cavity left without a coupler. Characteristics of the observed coupler-bunch instability are summarized in Table 2.3.1, where the newly assigned instability "1707" is presented.

2.3.3 Instability Thresholds for the Low-Emittance Operation

In the low-emittance optics, the natural bunch-length is 1.5 cm (calculated), which is 2/3 of the high-emittance optics, leading to an increase of the longitudinal instabilities, because of a reduction of the Landau damping effect.

After the insertion of the couplers, the thresholds of "758" were above 300 mA in the high-emittance mode. However, thresholds measured in the low-emittance operation were

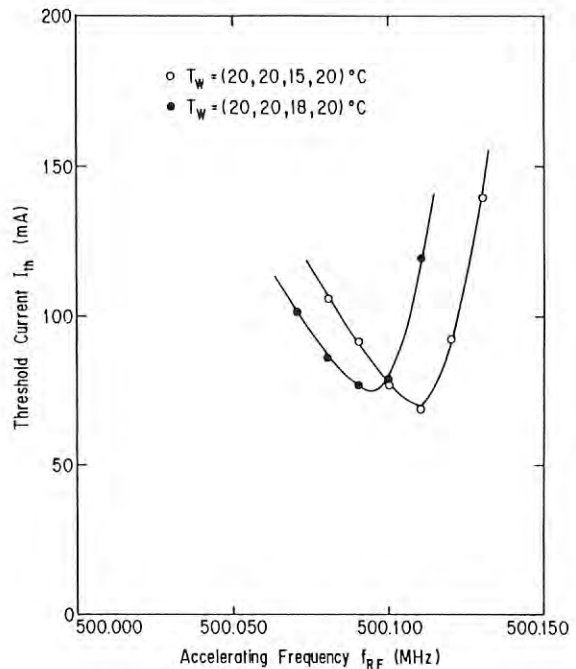


Fig. 2.3.4 Threshold currents of the "1707" instability measured in the high-emittance operation. This instability was recognized after the insertion of the damping couplers.

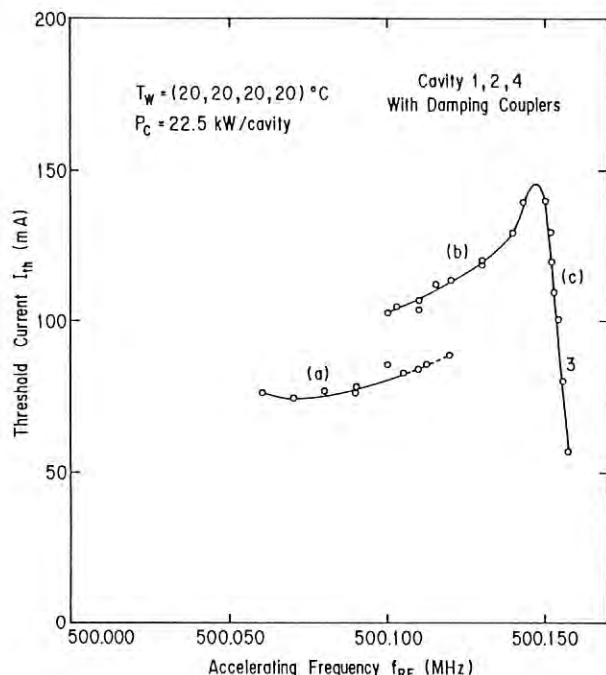


Fig. 2.3.5 Threshold current of the "758" instability for the low-emittance optics measured after the coupler insertion. Smaller bunch length leads to a larger instability effect by a factor of three.

80-100 mA, as shown in Fig. 2.3.5. A discontinuity observed on the threshold curve corresponded to the excitation of the rf-fields in the different cavities. The frequencies excited were (a) $471 \cdot f_r + f_s$ in #1 and #4 cavities, (b) $471 \cdot f_r + f_s$ (#1, #4) and $472 \cdot f_r + f_s$ (#2), (c) $473 \cdot f_r + f_s$ (#3), where f_r is the revolution frequency, f_s the synchrotron frequency.

In the low-emittance operation, the horizontal beam size σ_x (rms), which was observed with the profile monitor at BL21, was reduced from 2.6 mm to 1.7 mm, as shown (c) in Fig. 2.3.6. In the figure, (a) and (b) are the horizontal beam sizes in the high-emittance operation, and before and after the coupler insertion, respectively. Increase of σ_x was observed at (a) above 100 mA, and (b) above 250 mA, corresponding to the excitation of "758" and/or "1707" instabilities.

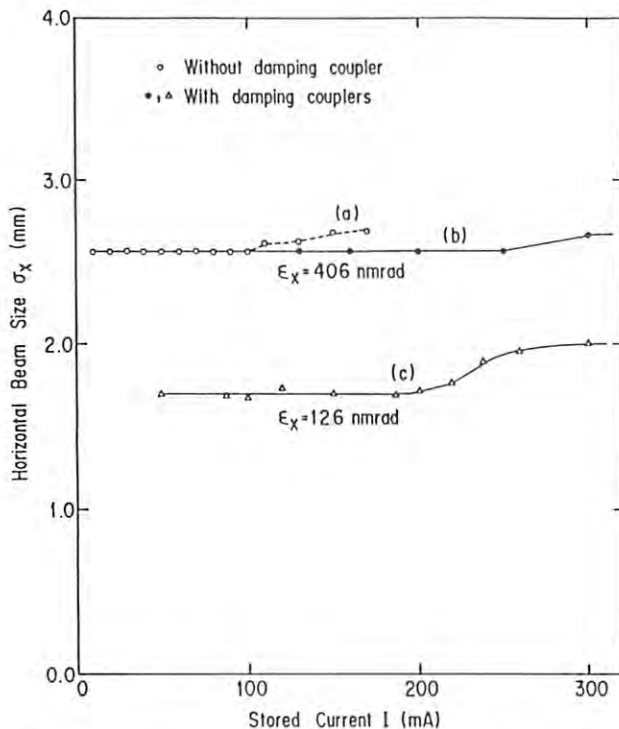


Fig. 2.3.6 Horizontal beam size as a function of the stored current.

- (a) High-emittance optics, and without couplers.
- (b) High-emittance optics, and with couplers in the cavities #1, #2 and #4.
- (c) Low-emittance optics, and with couplers in the cavities #1, #2 and #4.

2.3.4 Study of Ion-Trapping with Bremsstrahlung

Bremsstrahlung from the electron beam perturbed by the rf-knockout field

In electron storage rings, a stored beam ionizes residual gas molecules in the vacuum chamber. Created positive ions can be trapped in the beam by an attractive force. This phenomenon, called ion-trapping, often causes detrimental effects to the beam, such as beam blowup,

emittance growth or beam lifetime shortening.

Though the measurements of tune shift and spread are important methods to study ion-trapping, there are still ambiguities because they are also produced by gradient errors and non-linear elements in the storage ring other than the ion-produced electric field. At the PF ring, we have developed a direct method to observe the ion-trapping, in which bremsstrahlung produced by collisions between the electron beam and trapped-ions are detected.

Figure 2.3.7 is a setup for the present experiment, in which high energy bremsstrahlung penetrated a synchrotron radiation absorber and hit a gamma-ray detector.

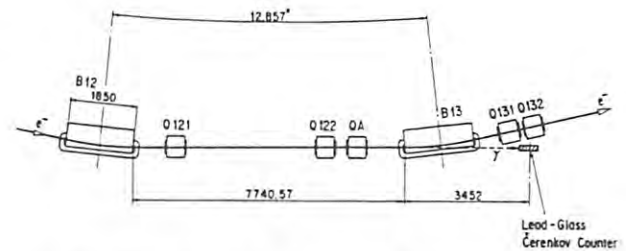


Fig. 2.3.7 Schematic drawing of the experimental system. Bremsstrahlung was detected by a lead glass gamma detector placed at 3452 mm away from the end of the straight section between B12 and B13.

The gamma-ray detector was comprised of a lead-glass Cherenkov counter made of lead-glass blocks (30 cm in length) glued to a photomultiplier and a veto-counter which excluded unwanted charged particles. The veto-counter was made of plastic scintillator glued on a photomultiplier. A lead collimator was set in front of the lead-glass and the other sides were shielded by lead blocks to eliminate background particles. The aperture of the collimator (30 mm in width, 50 mm in height) was wide enough to admit all the bremsstrahlung produced in the straight section even when the beam blew up. The whole detector system was movable horizontally and was located to get a maximum count rate.

Output pulses from the detector were counted by a multichannel analyzer in the MCS (multichannel scaling) mode. The threshold energy for gamma-ray detection was set to 1.9 GeV.

When the beam blew up in its transverse direction, there was a difference between the count-rates from the residual gas and that from the captured-ions. Because residual gas is thought to uniformly populate in the beam chamber, the bremsstrahlung yield does not change by a slight beam blowup. However, the yield from the trapped-ions decreases. Since ions located close to or in the electron beam orbit and their motion is slower than the transverse movement of the electron, the collision-rate decreases at the moment of blowup of the electron beam. Thus the existence of an ion-cloud can be proved by an artificial beam-size blowup.

To produce the beam blowup, we applied an rf knockout field on the beam with a duration of 20 ms in every 100 ms in the vertical direction. Then the time dependent variation of the brems-

strahlung yield was measured by a multichannel analyzer in the MCS mode with a trigger initiated by a gate signal of the rf-knockout. The frequency of the knockout was chosen to be $f \cdot \Delta v$, a fractional betatron frequency. Because the count-rate was small, the data was accumulated with multi-time scanning.

Partial and uniform bunch-fillings

The PF ring is usually operated in the multibunch mode. Since its first operation for synchrotron radiation experiments in May 1982, several problems have occurred by the ion-trapping. They were cured by a partial filling operation in which some of successive RF buckets were not filled with electrons (Activity Report 1982/1983).

We performed measurement of the bremsstrahlung yields in the multibunch operation. Two bunch fillings, shown in Fig. 2.3.8(a) and (b) were used in the present experiment, where (a) and (b) are called uniform and partial fillings, respectively. Measured bremsstrahlung yields are shown in Fig. 2.3.9. Experimental conditions are also presented in Table 2.3.2 together with conditions in a single bunch operation described below. These were all taken in the low-emittance operation.

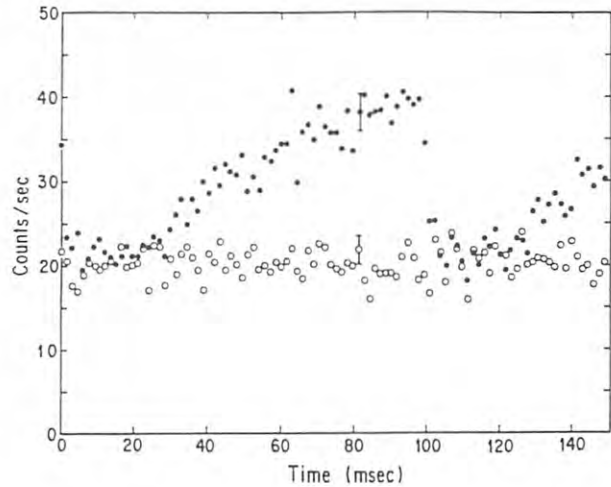


Fig. 2.3.9 Bremsstrahlung yields measured with partial and uniform fillings, corresponding to (a) and (b) in Fig. 2.3.8, respectively. Yields for the uniform filling were always higher than those for the partial filling, because of additional bremsstrahlung from trapped-ions. Dips in the uniform filling correspond to the vertical beam blowup by the rf-knockout field. These data were taken with the low-emittance optics.

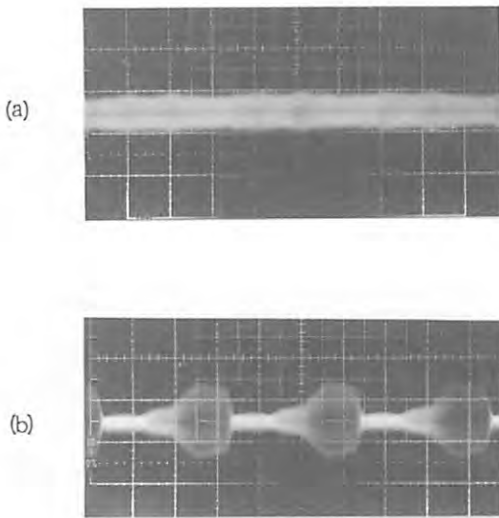


Fig. 2.3.8 Pictures of two bunch fillings used in this experiment. (a) uniform and (b) partial fillings.

With uniform filling, count-rates (solid circles in Fig. 2.3.9) decreased when the beam blew up and increased with no rf-knockout field. This fact indicated the existence of an ion-cloud. On the other hand, there were no decreases in the yields in the partial filling, showing that few or no ions were captured. This result was in good agreement with that obtained in the previous experiment in the high-emittance operation. The aperture of the collimator was set sufficiently wide so that all bremsstrahlung could be detected, even when the beam blew up vertically.

Ion-trapping in the single bunch operation

We also applied this method on the single-bunch beam. The result showed that ions were trapped even in the single-bunch operation with stored current of 38 mA. The theory predicts that ions are more unstable in the single-bunch beam, and harder to be captured than with partial filling mode. Therefore, this phenomenon cannot be explained by the simple ion-trapping theory.

Table 2.3.2 Bunch fillings and storage ring conditions during present experiment.

Case	(a)	(b)	(c)	(d)
Bunch filling	uniform filling	partial filling	single bunch	single bunch
Beam current (mA)	37.2 ~ 36.9	36.8 ~ 36.6	38.0 ~ 36.6	21.1 ~ 20.7
Vacuum pressure (Torr)	3.9×10^{-11}	4.4×10^{-11}	3.5×10^{-10}	3.7×10^{-10}

The measurement was carried out at stored currents of 38 mA and 21 mA, and is shown in (c) and (d) of Table 2.3.2, respectively. The MCS yield is shown in Fig. 2.3.10, where the count-rates obtained from 2000 scannings are plotted. The rf-knockout field was excited in $0 \sim 20$ ms and $100 \sim 120$ ms. The pressure measured at the upstream position of bending magnet B13 was 3.5×10^{-10} Torr in case (c) and 3.7×10^{-10} Torr in case (d).

Figure 2.3.10 exhibits decreases in the bremsstrahlung yields with beam blowup. This behavior indicates the existence of the trapped-ion cloud in the beam even in single-bunch operation.

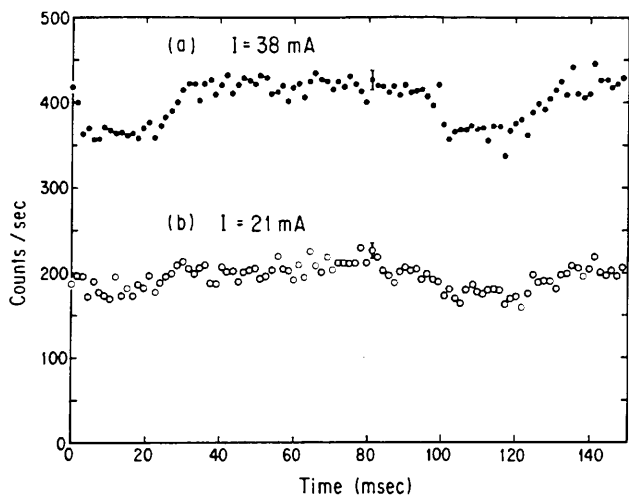


Fig. 2.3.10 Bremsstrahlung yields for the single bunch operation at stored currents of (a) 38 mA and (b) 21 mA. Dips in the yields exhibit an existence of the trapped-ion cloud, even in the single bunch beam, which is difficult to explain by the simple theory applied to the present PF ring.

3. IMPROVEMENTS

3.1 INJECTION

The 2.5-GeV positron beam was injected into the storage ring and stored on December 20, 1985. We obtained a maximum current of 5.5 mA and a beam lifetime of about 120 hours after several hours with the linac beam of 2 mA, 10 nsec and 2 Hz. The linac is supplying a positron beam of 10 mA and 2 nsec at 25 Hz for TRISTAN. In order to accumulate positrons quickly, it is necessary to replace kicker magnets, septum magnets and their power supplies. At present, four new kicker magnets were designed and installed in the storage ring. They are excited by four existing power supplies. The septum magnet and power supplies are now under construction.

3.1.1 New Kicker Magnets for Positron Injection

Four new kicker magnets were designed and constructed for positron beam injection. They are window frame type magnets and are made of ferrite core. A coil of two turns was chosen to

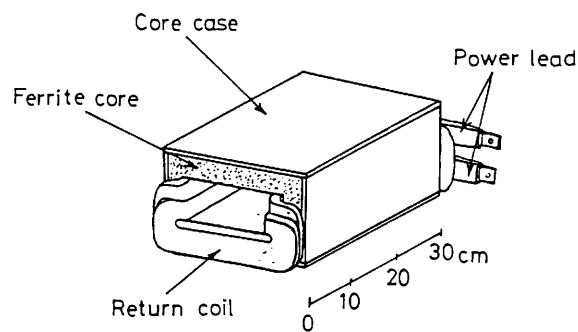


Fig. 3.1.1 Schematic drawing of the kicker magnet.

produce a uniform field with smallest self inductance. The dimensions of ferrite core and location of coil were optimized by using the computer code "TRIM". To enclose the maximum beam excursion estimated by a tracking program, we need two types of magnets, one with wide aperture of $180w \times 80h$ for K1 and K2, and the other with narrow aperture $130w \times 80h$ for K3 and K4. The specifications of the new magnets are listed in Table 3.1.1. A schematic drawing of the magnets is shown in Fig. 3.1.1. Magnetic fields were measured by using a small search coil. One of the results of field measurement is shown in Fig. 3.1.2. The old kicker magnets in the storage ring were replaced with new magnets in August of 1987.

Table 3.1.1 Specifications of the kicker magnets

Type	K1, K2	K3, K4
Core length	300 mm	300 mm
Number of turns	2	2
Dimensions of window	180mm×80mm	140mm×80mm
Maximum current	5000 A	5000 A
Self inductance	5.8 μ H	4.8 μ H

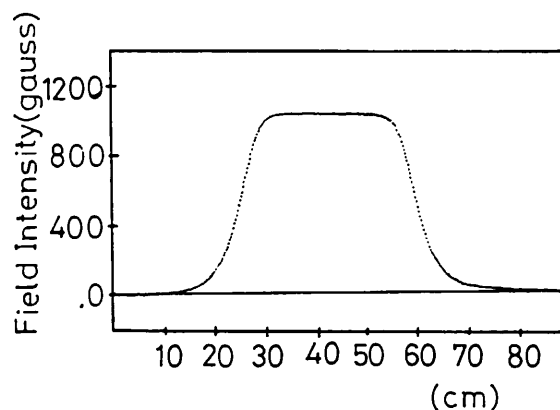


Fig. 3.1.2 A result of the measurement of magnetic field of the kicker magnet.

The new kicker magnets were set outside of their ceramic vacuum ducts. The inner wall of a ceramic duct was coated with titanium of thickness about several microns. This coating did not affect the field penetration through the chamber. The end of ceramic duct was metallized with nickel and soldered to a kovar attachment. The strong fringing field caused spark discharge on the boundary between the nickel and titanium coating. To suppress this discharge, we shielded the boundary of the duct with a permalloy thin sheet.

3.1.2 Electron Beam Injection with the New Kicker System

From October of 1987 electrons were injected with the new set of kicker magnets and ceramic ducts. The parameters of the new kicker are listed in Table 3.1.2. The beam current passing through the BT was measured with current transformers (CT). Fig. 3.1.3 shows the waveforms observed with CT1 placed at the entrance of the beam transport line, and CT7 at the end of the transport line. We observed an electron beam pulse of 23.4 mA and 800 ns at CT1, and 13.7 mA and 300 ns at CT7. Under these conditions, accumulation rate of about 2 mA/sec has been obtained. The accumulation rate was measured as a function of the magnitude of injection bump.

Table 3.1.2 Parameters of the kicker magnets (injection bump of 23 mm and -1 mrad)

	beam deflection (mrad)	peak current (A)	pulse length (μ sec)
kicker 1	2.561	1702	6
kicker 2	2.599	1725	6
kicker 3	2.789	1830	6
kicker 4	2.099	1488	6

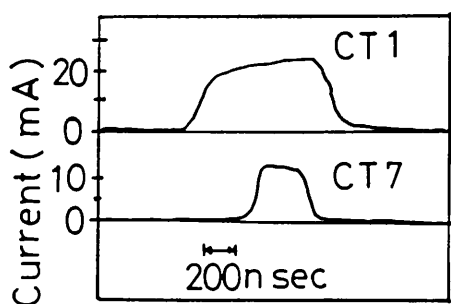


Fig. 3.1.3 The electron beam pulse from the linac. The upper trace is CT1 installed at the entrance of beam transport line i.e. the end of the linac. The lower trace is CT7 installed at the end of beam transport line.

The result is shown in Fig. 3.1.4. With an injection bump magnitude of about 24 mm, we obtained a maximum accumulation rate of about 4 mA/sec. The accumulation efficiency (the ratio of the amount of accumulated charge to that passing through the injection point) divided by the RF capture efficiency is about 50%.

The short pulse beam from the linac was injected to fill a single bunch of the storage ring. Under the condition of the linac beam of 180 mA and 2 ns, an accumulation rate about 0.3 mA/sec was obtained.

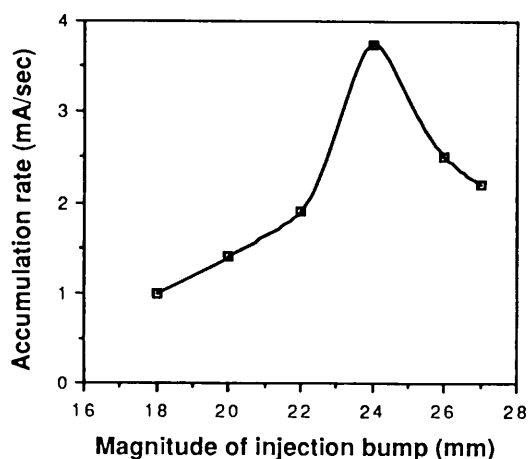


Fig. 3.1.4 Accumulation rate as a function of the magnitude of injection bump.

3.1.3 Measurement of Energy Spectra of the Electron Beam from Linac

The energy spectra of the electron beam from the linac were measured by using the slit which is located in the middle of beam transport line (BT) and CT3₁. Fig. 3.1.5 shows the geometry of the energy analyzing system on BT. The analyzing slit was fixed at an energy resolution of 0.05%. Spectra were taken by changing the current of bending magnet (BTBM). Energy spectra were measured by varying RF phases of injector section of the linac (accelerator guide 0-1).

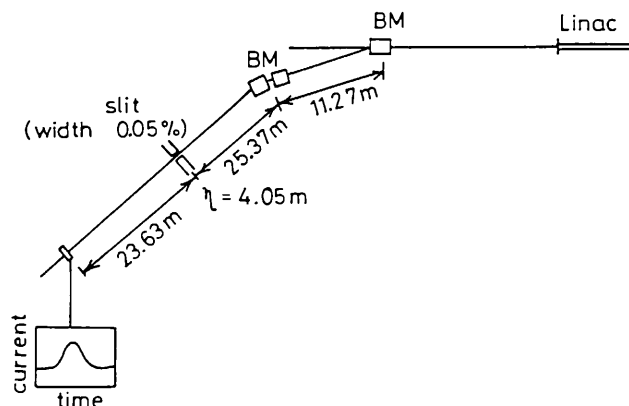


Fig. 3.1.5 Geometry of the energy analyzing system on BT.

Fig. 3.1.6 shows the intensity as a function of time and energy plotted in a 3-dimensional diagram. Three spectra are shown for RF phases of the section, +6, 0 and -6 deg.

To observe the energy spread of the beam profile monitor No.9 was used. The monitor was located just downstream of the slit. An image processing system²⁾ was introduced to minimize the ambiguity of observation. The system consists of a video digitizer and a microcomputer (PC-9801E). A block diagram of the system is shown in Fig. 3.1.7. Fig. 3.1.8 shows the result

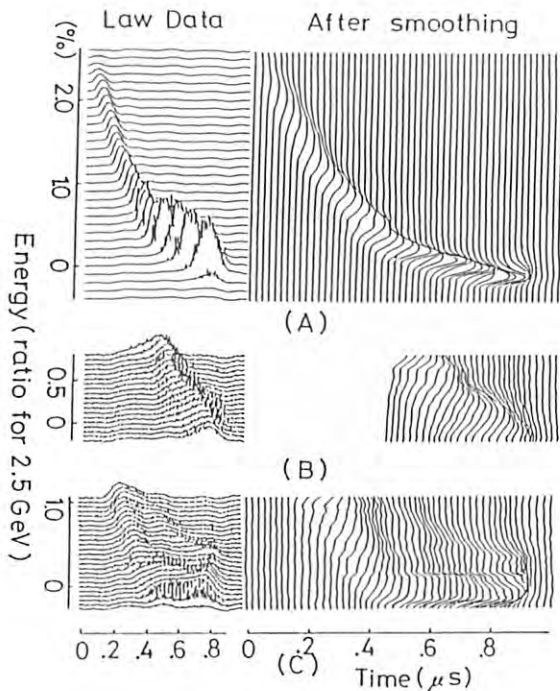


Fig. 3.1.6 Energy spectra of the electron beam from the linac. Relative phases of the accelerator guide 0-1 are (A): -6 deg; (B): 0 deg; (C): +6 deg.

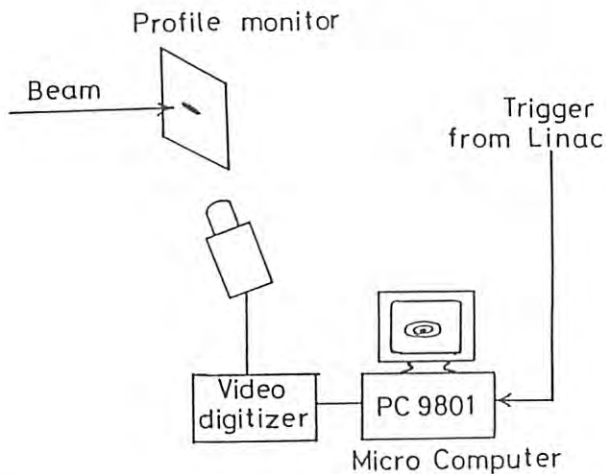


Fig. 3.1.7 A block diagram of the image processing system for the profile monitor No.9.

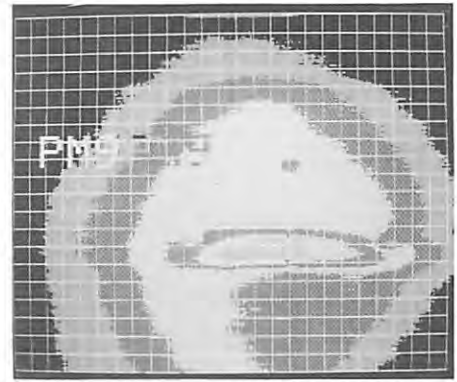


Fig. 3.1.8 An image from profile monitor No.9 after processing.

for a false-colored image of the monitor. The horizontal width of the profile image corresponds to the energy spread of the beam (0.05 %/division).

The energy of the head of the beam pulse is higher than the other part of pulse. This energy variation of 2% in the leading part of the pulse is due to the effect of transient beam loading. Since the energy acceptance of the BT was about 1%, this part of beam pulse is lost through the BT.

References

- (1) T. Mitsuhashi, T. Urano, T. Katsura, K. Haga, A. Enomoto, H. Hanaki and S. Ohsawa, Proceedings of the 12th Linear accelerator meeting in Japan, p. 129, 1987.
- (2) N. Kanaya, Rep. of Sci. Found. by Ministry of Education, Contract #60750033, 1986.

3.2 IMPROVED RF-CAVITIES AND HIGH-POWER TESTS

The accelerating cavities in the Ring (single cell, 500 MHz) are being operated very reliably. Dissipation power for routine operation is 30 kW in each cavity, while the maximum record of power dissipation was 60 kW. This value is already very high for this type of cavity.

Yet, we are attempting to put more power into the cavities by making some improvements in the ports of the cavity for tuning plunger, damping coupler and input coupler. The present maximum power is mainly limited by the following reason. Inner surfaces of these ports were partly made of stainless-steel (Fig. 3.2.1(a)). RF currents heated the ports at high power, and eventually caused melting of finger contactors attached to the surface. By the electron-beam-welding method (Fig. 3.2.1(b)), we then succeeded to attain a high power up to 110 kW into this cavity at the test bench (Fig. 3.2.2). With this success, we have decided to make the same improvement on the cavities in the Ring during this summer shut down. By upgrading the klystron system, it will be possible to store more current

with the improved cavities and the remaining straight section which has been reserved for additional cavities will be utilized for insertion devices.

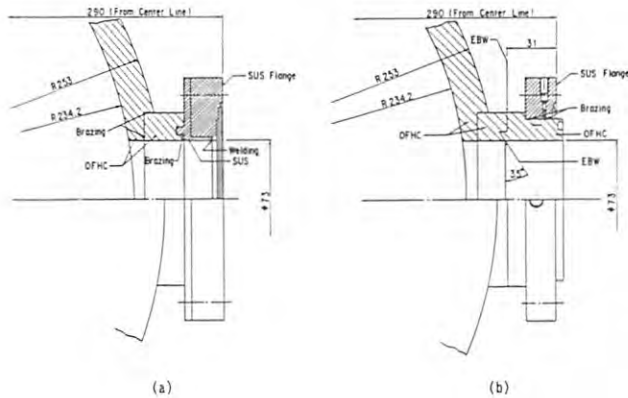


Fig. 3.2.1 Structure of a cavity port for the tuning plunger, (a) before improvements, and (b) after changing the inner-structure by the electron-beam welding method.

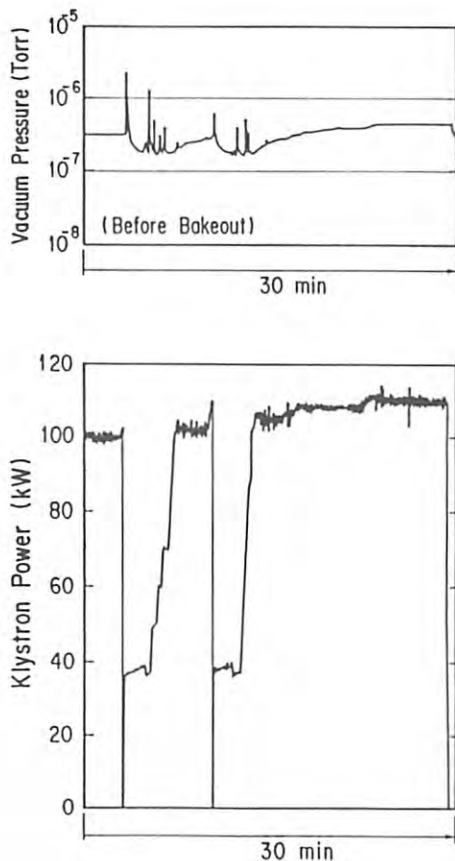


Fig. 3.2.2 High power test for the improved cavity at the test bench. Klystron power of 110 KW were applied to one cavity. Pressure in the cavity (before bakeout) is also plotted.

3.3 VACUUM

3.3.1 Modifications

The ring vacuum system was modified in the summer shutdown of 1986, following the first improvements in the summer of 1985. The improvements were as follows;

- three B-ducts with a light exit port at 0 degree were newly designed to extract SR from an insertion device,
- four new Q-ducts for additional quadrupole magnets were replaced by new ones for low emittance operation, and
- a ceramic duct was installed for a new kicker.

The vacuum duct for in the bending magnet section called B-duct has a synchrotron radiation (SR) exit port, which normally takes out SR from the bending magnet. Some of the B-ducts have ports for SR from insertion devices such as an undulator, a multipole wiggler and a superconducting vertical wiggler. The exit ports of new B-ducts are also able to extract SR from such insertion devices and the flange size of the exit port is 6" (ICF203), the center of which is on a kickerstraight line called the 0 degree line. These new B-ducts were set in the bending magnets B03, B05and B07.

Additional quadrupole magnets were installed at S042, S123, S182 and S263. As the bore radius of them is narrower than those of the ordinary quadrupole magnets, the vacuum ducts in the sections called Q-duct were cut and replaced by newly designed ducts. The new ducts had different cross section from that of the old Q-duct, so that shape-transition pieces were welded on both ends of the new ducts.

The old kicker magnets had four turn coils in their fat vacuum chambers. We intend to inject positrons at 25 Hz in future, so that we have to increase the repetition rate of injection. The kicker called K3, which was set at the downstream of the septum magnet, was replaced with a newly designed one. It was composed of a ceramic duct and a pair of two-turn coils with ferrite cores. The duct was made of highly purified alumina ceramics and the inner surface of the duct was coated with a titanium thin film. The titanium was deposited in vacuum on the inner surface after it was cleaned in ultrahigh vacuum. The thickness of the film was several microns. A short collar made of Kovar was brazed in vacuum on both ends of the duct. The collars were covered by evaporated titanium film, so that the electrical connection between the collars and the film of the duct might be durable through long operation.

3.3.2 Flange Cap Accident

We had a serious experience in the improvement process. The section between B05 and B13 was opened to air, and a new gate valve and new ducts were installed in the section. At an intermission, one end of the ring duct was covered by a polyethylene cap to protect the conflat flange. The work was finished at the

opposite side of the ring duct, about 45 meters away, so evacuation was started for a leak test. The cap was sucked accidentally in the ring duct and went through about 40 meters.

This accident was caused by the following reasons; (1) thickness of the flange cap was thin, (2) we missed to confirm the gate valve to be closed, which was located at the middle of this section, and (3) it was overlooked to check if one had prepared for evacuation at the other end of the long arc. After the accident occurred, we opened and removed some ducts and finally found the cap full of wrinkles. But some small pieces of the brim were missing and could not be found from the opened ducts. We tried to find the broken pieces by using a fiber scope and to take them out by a vacuum cleaner with a long narrow tube. We continued the search for a week until all pieces visible with the scope were removed. The vacuum chamber along the ring was closed, evacuated and baked as usual. The ultimate pressure in the troubled section reached below 2×10^{-10} Torr and this value was comparable to that of other accident free sections, and became ready for injection.

Figure 3.3.1 shows distribution of pressures along the ring. The accident region corresponds to the gauge numbers from 9 to 20. The shadowed bars indicate pressures before beam injection. Though the average pressure around the ring reached the ultrahigh vacuum region of 10^{-11} Torr, it implies that the inner surface of the beam duct in the accident section was covered by some melted polyethylene dust. A kind of dissociated polymer might be desorbed from the surface irradiated by photons and photoelectrons. To confirm this assumption, partial pressure was measured by a mass filter at gauge number 13 but such dissociated high polymer was not observed. Only hydrogen and carbon monoxide were dominant as was the same in the other sections.

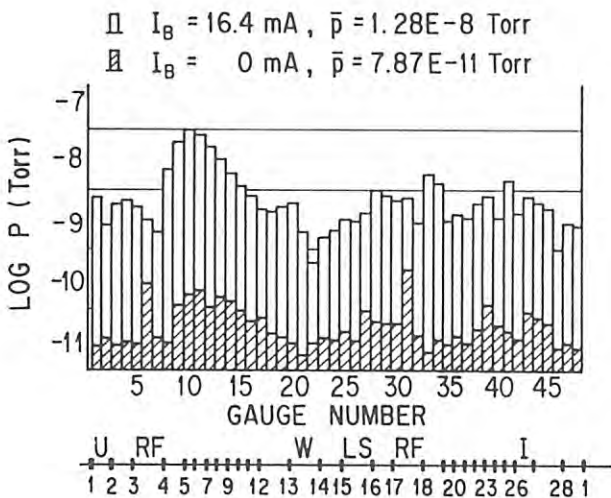


Fig. 3.3.1 Pressures along the electron storage ring. Pressure gauges are numbered from 1 to 48. The lower abscissa shows the locations of bending magnet. Bars (shadowed) indicate the background pressures with no beam. Bars (white) indicate the pressures just after beam storage.

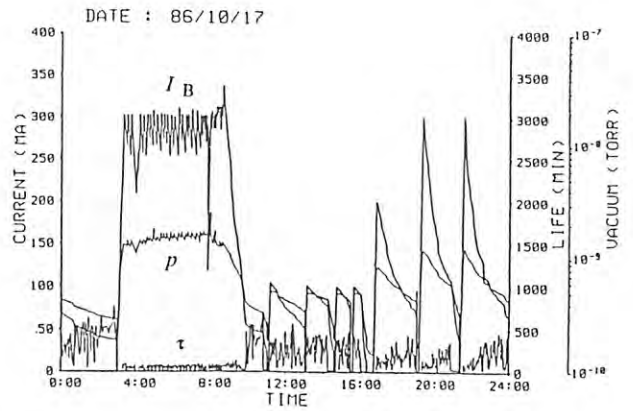


Fig. 3.3.2 Pressure change on October 10 in 1986 after the accident of polyethylene cap. Beam current I_B and beam life time τ are also shown. The beam was injected frequently up to 300 mA in order to clean the vacuum ducts by photons.

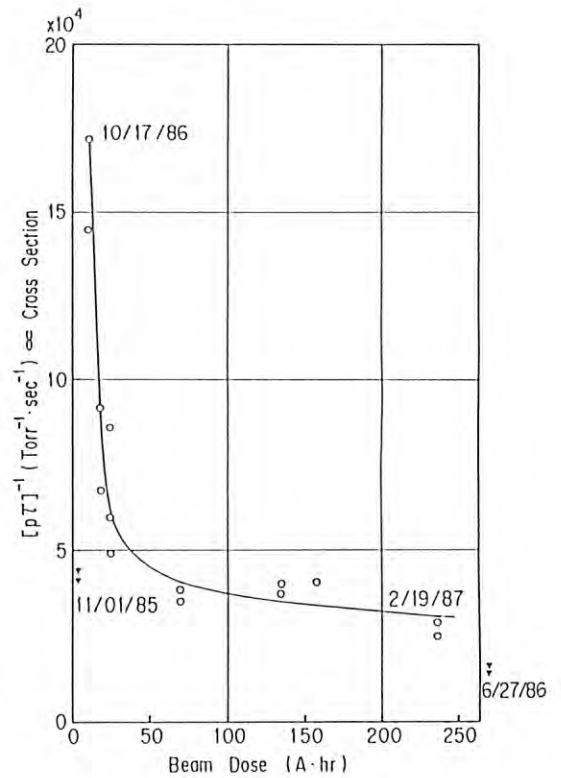


Fig. 3.3.3 Collision cross sections with the residual gas molecules. They were expressed as $1/(p\tau)$ and plotted against the beam dose. Open circles indicate the values after the polyethylene accident in the second shutdown, and filled triangles indicate values after the first shutdown. The short beam life time shown in Fig. 3.3.2 was not caused by the effect of air exposure during the shutdown but by the contamination of polyethylene cap.

Figure 3.3.2 shows the pressures, stored currents and beam lifetimes through a whole day, when the accumulated current was 10 A·hr. The beam lifetime at this early stage after the shutdown was very short compared with that after the shutdown of 1985. Though the pressures in the figure were not so high, but the beam lifetime was very short. These results indicate the beam might have trapped something called "microdust". It might be a minute particle composed of many atoms such as hydrogen and carbon. Or some dusts in the air might enter in the ring ducts when we struggled to take out the small pieces of the cap flakes. The collision cross section between the electron beam and the particles or dusts can be estimated from the inverse of pressure times beam lifetime. Those values are shown in the Fig. 3.3.3 and plotted against the accumulated current. The values in the early stage decreased and reached to the usual cross section after 70 A·hr. The beam lifetime, pressures and stored currents were shown in Fig. 3.3.4, when the accumulated current was 225 A·hr¹). This shows the usual vacuum conditions were resumed.

Bremsstrahlung from the electron beam was measured at the downstream of the accident region. The results indicate that the "microdusts" might run through the ring.

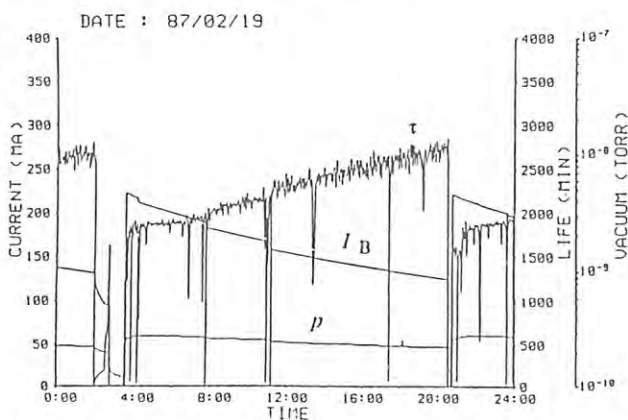


Fig. 3.3.4 Pressure, beam life time and the beam current on February 2 in 1987. The injected beam current was 225 mA, and average pressure of the ring was less than 3×10^{-10} Torr. Beam life time was over 1700 minutes at the beam current of 220 mA, and reached 2700 minutes just before the next injection.

3.3.3 Sensitivity of the Vacuum Gauge

The PF ring has 48 vacuum gauges in the vacuum ducts. The discussions described above were based on the calibrated pressures along the ring. The sensitivities of the vacuum gauges (Bayard-Alpert type ionization gauge) have a nominal value of 25 Torr^{-1} . To confirm this value, we measured and calibrated the sensitivity of every gauge for nitrogen with the gauge envelope standardized at the Photon Factory²⁾. First, one gauge was calibrated against a spinning roter gauge (SRG), then all the other gauges were calibrated against the calibrated gauge. The averaged sensitivity was 24 Torr^{-1}

and 95 % of the gauges had sensitivities between 23.5 and 25.5 Torr⁻¹

3.3.4 Angle-resolved Photodesorption Experiments by a Unidirectional Mass Filter

Photodesorption was observed in the test duct, which was set on the BL21-Vac. line, by using a unidirectional mass filter. The test duct with a diameter of 100 mm was made of aluminum alloy A6063. A collimation slit 5 mm wide and 5 mm high was set at 13 m from the source point. This slit defined the conductance for the molecules desorbed from the test duct. The desorption rate was obtained by the conductance and pressure differences between the ionization gauges set on both sides of the slit. Desorption yield was obtained as a ratio of desorption rate to the number of incident photons which is estimated from the geometrical conditions and the beam current.

The unidirectional mass filter (UDMF) was composed of a multicapillary unidirectional rotatable nose and a mass filter. The nose preferentially accepts the molecules desorbed from a narrow surface of the test duct at which it is aiming. The UDMF can distinguish the gas species at the aimed surface from that of other surfaces. The nose can move at a radius smaller by 5 mm than that of the cylindrical test duct. The results are quite interesting. 1) With a low accumulated current of 200 mA·hr, the desorption rate on the surface directly hit by incident photons is slightly higher than that of the other surfaces, which were irradiated by scattered photons and photoelectrons. 2) With a higher accumulated current of 9200 mA·hr, the desorption rates at the point irradiated by the direct incident photons became lower than those from the other surfaces. It has been widely considered that the directly irradiated point is the main source point of photodesorption. The results indicate that the other surfaces except the directly incident point can be also sources. Thus, beam cleaning of the vacuum duct depends strongly on the cleaning at both the directly irradiated surface and the surfaces indirectly irradiated³⁾ by the scattered photons and photoelectrons.

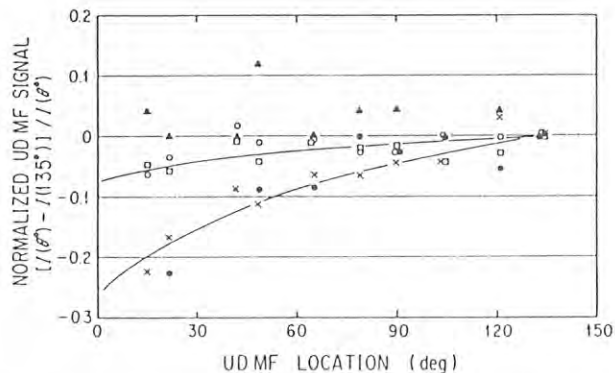


Fig. 3.3.5 Angular distributions of photodesorption at normal incidence for a beam dose of $9.2 \times 10^3 \text{ mA}\cdot\text{hr}$. ○ hydrogen; ● methane; Δ water; □ carbon monoxide; and × carbon dioxide.

Future electron storage rings will demand lower vacuum than that of the present Photon Factory, where the typical vacuum is lower than 1×10^{-11} Torr with no beam and lower than 5×10^{-10} Torr with the beam of 250 mA. It is reported that the structure with an antechamber can get low vacuum by separating the beam space of the duct from the photo-desorption source in the antechamber. On the other hand, the experimental results mentioned above indicate that the antechamber will be cleaned quickly while the beam space will be cleaned slowly. We propose that scattered photons should be constructively utilized for the beam cleaning.

References

- (1) M. Kobayashi, H. Kitamura and Y. Takiyama; Proc. IEEE Particle Accelerator Conf. p. 1614 (March 16, 1987, Washington, D.C. U.S.A.).
- (2) Y. Takiyama, M. Kitahama and M. Kobayashi; Proc. 6th Meeting on Ultrahigh Vacuum Techniques for Accelerators and Storage Rings (Feb. 27, 1987, KEK) KEK Report 87-8, p. 49.
- (3) M. Kobayashi, M. Matsumoto and S. Ueda; J. Vac. Sci. Technol. A5(4), (1987) 2417.

3.4 BEAM ORBIT SHIFT DUE TO CHANGE IN EXCITING CURRENT OF SUPERCONDUCTING VERTICAL WIGGLER

Beam position shift occurring every 5 hrs was found to be strongly correlated to the liquid helium transfer to the superconducting wiggler. Hence we decided to reexamine the power supply circuitry of the wiggler.

Generally, the power supply for superconducting magnet is connected to an external protection resistor in parallel to the superconducting coil to bring the heat energy out of the magnet in case of quenching. When the resistance of the current feedthrough increases, the current in coil decreases or vice versa, because the power supply keeps the total current flowing the coil and resistor to be constant.

In the vertical wiggler, the evaporated helium gas passes through the current feedthrough and carries out the joule heat. But the quantity of the evaporated helium is 5-15 l/sec when liquid helium is transferred while about 1 l/sec when not transferred. When helium is transferred, the temperature decreases at the current feedthrough, which is cooled by the evaporating helium. This will cause the coil resistance to increase.

Figure 3.4.1 shows the movement of the light position measured at 12 m downstream from the source point by changing the exciting current. To suppress the fluctuation, several methods are considered.

- (1) To control the pressure in the cryostat and keep a constant flow of helium gas at the current feedthrough.
- (2) To include a protection resistor inside the feedback loop in the circuit of power supply.
- (3) To add a shunt resistor in series to the superconducting coil for another feedback loop.

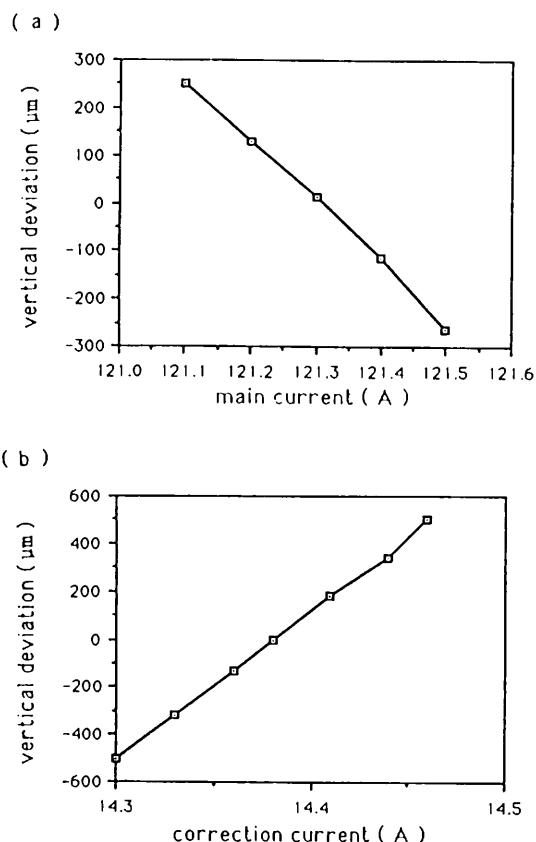


Fig. 3.4.1 Beam movement due to the change in the current of each power supply.
(a) main power supply.
(b) sub-power supply.

We employed the second method. However, since there is only a pure inductance as the external load to the power supply, the power supply system became unstable. Another resistor must be therefore added parallel to the coil during current change. The resistor should be removed after exciting the coil, because it is undesirable as mentioned above. However it should be gradually removed to avoid current oscillation.

In the beginning, the resistors were added by three steps and removed at the end of excitation. But beam was often dumped by the current oscillation and the wiggler was quenched. Presently the resistor is replaced by an electric resistor as shown in Fig. 3.4.2 to reduce a sudden change of the resistance. After exciting the magnet, the resistance increases continuously. Then the resistor circuit is completely opened when the electric resistor value sufficiently large. Finally the electric resistor is decreased. The steps in reversed order are taken in de-excitation.

The wiggler magnet is now operated by the method described above. However, it became sensitivity to noise. A beam fluctuation originating from the change of wiggler current due to external noise is occasionally seen. The third method will be tried as next step.

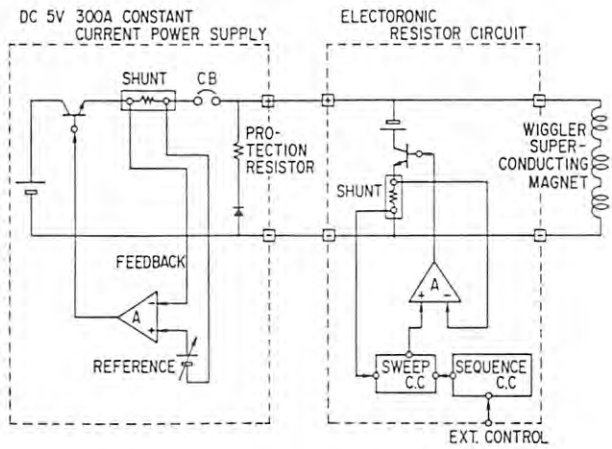


Fig. 3.4.2 Schematic drawing of the power supply for the vertical wiggler.

3.5 PHOTON BEAM STABILIZATIONS

3.5.1 Installation of Photon Beam Position Monitors

We have measured the vertical position and its fluctuation of the synchrotron light by using two position-sensitive detectors at the beam diagnostics line BL-21. Because the detectors had good position accuracy and fast frequency response, they became the powerful tools for beam diagnosis.

After the installation of beam position monitors at BL-21, several beam position monitors were installed at beam lines for SR experiments. Details of the installation are shown in Table 3.5.1. Two photoemission wire monitors (WM) were put into upstream and downstream of the BBS of BL-12B, respectively. A split ion chamber (SIC) was installed in BL-10A.

A split emission chamber (SEC) was newly designed and installed in BL-4C. The SEC consists of a pair of triangular emitters housed in a field chamber. The emitters face the X-rays at an angle of a few degrees. The photocurrent from each emitters is amplified with a current amplifier. Two current signals from current amplifiers are fed into an analog divider to get a position signal proportional to the displacement from the center of the detector.

Table 3.5.1 Details of the types of beam position monitors at several experimental beam lines

Beam line	Type of beam position monitor
BL-21	WM (photoemission wire monitor)
BL-21	SIC (split ion chamber)
BL-12B	WM1, WM2
BL-10A	SIC
BL-4C	SEC (split emission chamber)

3.5.2 Noise-suppression Experiments by an Analog Feedback System

Beam position noise was detected by the position monitors installed in beam lines BL-4, BL-10 and BL-12, and analyzed by using FFT analyzer. The noise spectra at these beam lines have almost the same frequency components as that measured at BL-21. In order to suppress the beam position noise, we had already tested the analog feedback system at BL-21 and succeeded to reduce the noise by a factor of 10 for the frequency region of 10 Hz - 50 Hz.

In Dec. 1986, we applied the analog feedback system to the beam line BL-10A in order to suppress beam noise. Many users cooperated to observe its effect at other beam lines. In the analog feedback system, the beam position signal from the SIC at BL-10A was fed into three steering magnets through a servo controller which can compensate the frequency response of the steering magnets and power supplies, and the effect of the eddy current of the vacuum chamber.

Figure 3.5.1 shows the noise amplitude suppression ratios measured at twelve beam lines. When the feedback loop was closed, the beam noise levels at BL-10A were suppressed by a factor of 2. At the beam lines inside the local bump (BL-8 and BL-9), the noise suppression was also observed but less effective than that at BL-10A.

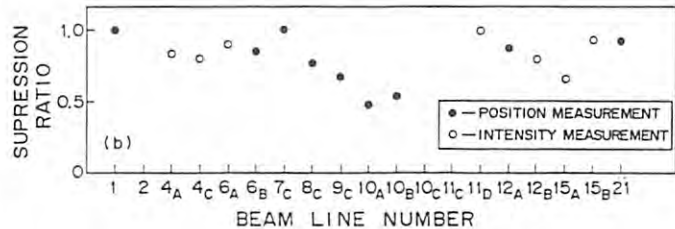


Fig. 3.5.1 Suppression ratio of the noise amplitude taken with closed feedback loop to that taken with open loop. Solid circles denote beam lines where beam position was measured, open circles beam lines where only intensity ratio was measured.

3.5.3 Daily Drift of Beam Position under Low-emittance Operation

Under the normal-emittance operation, the daily movement of the photon beam had the amplitude of 100-200 μm (measured by the beam position monitor placed 10.6 m away from the source point at the BL-21). As soon as the low-emittance operation started in February 1987, the daily drift of the photon beam position became as large as ~ 1 mm at BL-21. The photon beam position at the beam lines for experiments showed the same daily movement and the users asked to stop the low-emittance operation.

Figure 3.5.2 shows the daily drift of beam position measured by two different monitors: (a) a wire monitor at BL-21 (b) a set of two position monitors in the storage ring (PM35 and PM36).

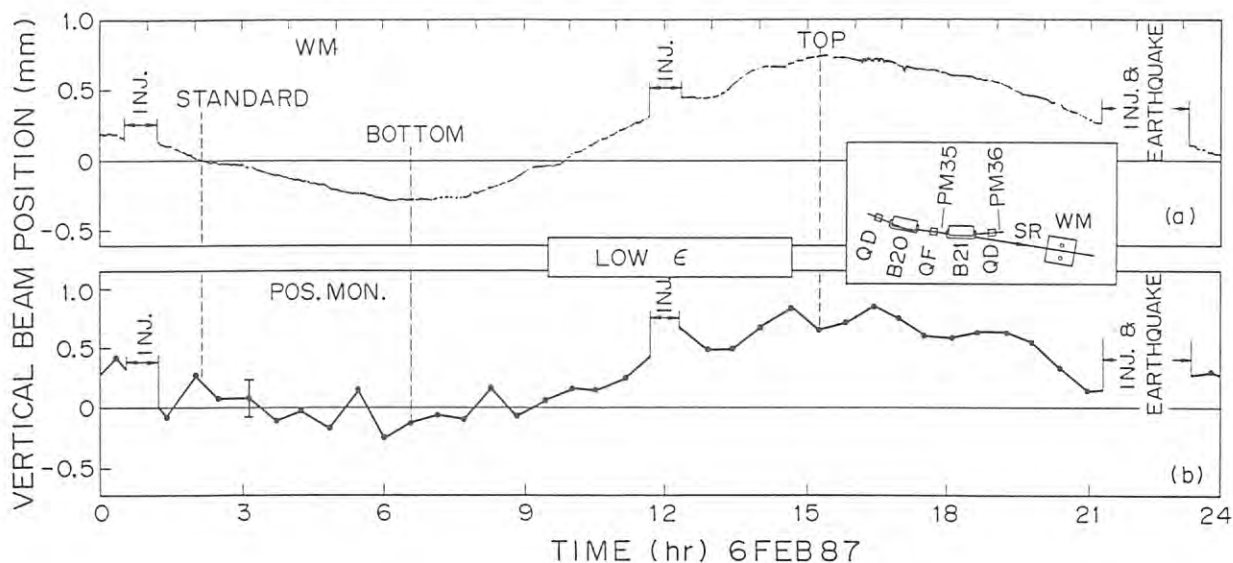


Fig. 3.5.2 Daily beam movement taken with (a) a photoemission wire monitor placed at $l=10.6$ m from the source point of BL-21.

The two PM's give the vertical position y of the stored electron beam and the angle y' at the source point. The vertical photon beam position Y at the wire monitor (WM) is expressed as $Y = y + y'l$ where l is the distance from the source to WM. Vertical beam position moves in correlation with the climatic environment around the light source building such as atmospheric temperature and sunlight. Detailed survey of the mechanism is now under way.

3.5.4 Digital Feedback System to Reduce the Daily Beam Movement

A digital feedback system was developed in order to stabilize the vertical beam position. The beam drifting was suppressed by successively compensating the closed orbit variation from the standard COD. First, we measured COD at two points of time corresponding to "bottom" and "top" shown in Fig. 3.5.2. The difference between the two COD's is the amount of total variation, which is equal to the amount to cancel the total daily drift. Second, whenever the position of the photon beam measured at BL-21 exceeds a preset limit, a command signal is sent to the compensation system, and changes the setting of all the steering magnets by 1 % of the total amounts of variation. The standard COD is then resumed.

Figure 3.5.3 shows vertical beam position measured (a) without and (b) with the digital feedback system. Data of COD measured every 30 minutes are plotted 16 times on a sheet to visualize the drifting motion. The digital feedback system can stabilize the COD within about 0.2 mm throughout the ring.

In order to apply the digital feedback system to the reduction of daily drift effectively, it is necessary to monitor the beam position accurately. It had taken about 5 minutes to measure the electron beam position in the storage

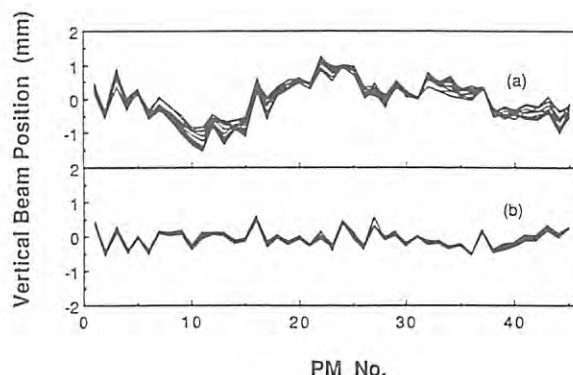


Fig.3.5.3 The vertical beam position measured (a) without and (b) with the digital feedback system. Data are plotted 16 times to visualize the drifting motion.

ring. The signals from 45 position monitors grouped into 8 substations had been switched sequentially by coaxial switches. After changing the data-taking algorithm, the signals are multiplexed in parallel at 8 substations and read by a fast digital voltmeter. It takes now one and half minutes to measure the COD. The shorter measuring time made the measurement more accurate.

The performance of the system meets the users' present requirements. But there remains some refinements to be done. In order to reduce further the beam drift, it is necessary to add smaller magnets which can adjust the amount of deflection finer than the present ones do.

3.6 BEAM CHANNEL

3.6.1 General

Users' experiments started with 8 beamlines (25 experimental stations) in FY 1983. Up until the end of FY 1986, twelve beamlines (BL-1, 2, 4, 7, 8, 9, 10, 11, 12, 14, 15, 21) were in operation. In this year, four beamlines (BL-6, 16, 17, 27) have been commissioned. In addition, constructions and installation of six beamlines (BL-3, 5, 13, 18, 19, 28) are in progress. The summary of beamline status in FY 1987 is shown in Table 3.6.1.

Most of the front ends are fabricated to extract SR of 40 mrad wide from the exit port. Its angular width is limited by the adjacent quadrupole magnet in the next straight section of the ring. The front end includes a vacuum protection system, a radiation safety system and an evacuation system with vacuum gauges and valves.

The vacuum protection system consists of an acoustic delay line (ADL), a fast closing valve (FCV) and pneumatic isolation valves. In addition, a water-cooled SR absorber and a 40 cm-thick stainless steel beam shutter are installed as a radiation safety system. These components are independently controlled by a distributed control system; a computer network with a star topology. The network includes 1) "outlying nodes" with microcomputers and 2) a "central node" computer. Each front end has one outlying node that is connected to the central node (LSI-11/23) via optical fiber links in a star topology.

At the downstream end of a beam channel for VUV experiment, mirrors are installed for VUV spectrometers, made of CVD (chemical vapor deposition) SiC to withstand the high power density of SR. SiC is resistant against thermal deformation and radiation damage. On the other hand, a pair of beryllium windows is attached to the end of the splitting section for X-ray experiment. Degradation in the efficiencies of these optical elements caused by contamination is a serious problem encountered in beam lines. A resuscitation of the contaminated elements is desirable since the deposition rate of contaminated layers is expected to be proportional to the accumulated photon flux at the mirrors. We have studied a recovery of the efficiencies by applying DC oxygen-discharge cleaning of carbon contaminated mirrors and gratings. The results are described in detail in the next section.

3.6.2 New Beam Channels

As shown in Table 3.6.1, the following beam channels were designed and under construction in FY 1987.

BL-3

The beam line BL-3 will be set on the so-called zero-degree line, so that the synchrotron radiation from the two bending magnets B2 and B3 can be extracted to serve for VUV and soft X-ray experiments. Since the BL-3 is set in the vicinity of RF cavities, all components of the front end had to be newly designed not so as to

interfere with the RF cavities. A seven mrad of radiation will be available from B2 and a seventeen mrad from B3.

BL-13

BL-13 is a beam line for the multipole wiggler with 27 poles which provides a total radiation power of 5.5 kW and used for hard X-ray experiments. The construction of this beam line is a joint project of the following national institutes; the Institute of Physics and Chemical Research, National Research Laboratory of Metrology, National Institute of Research for Inorganic Materials, Electrotechnical Laboratory, and National Laboratory for Industrial Chemistry. The beam line is being constructed by the Institute of Physics and Chemical Research while branch lines and experimental apparatus at the experimental hall are arranged by the other four institutes.

BL-18

The beam line BL-18 uses the radiation from the normal bending magnet (B18), and will be served for VUV experiments. The construction of BL-18 started in FY 1987 under a second joint project between ISSP (Institute for Solid State Physics) of University of Tokyo and KEK-PF. The BL-18 is about 10 meters long, and synchrotron radiation of 2.5 mrad is transferred to branch line 18A. Proposed experiments are mainly related to photoemission from surfaces and interfaces.

BL-28

The beam line BL-28 will use synchrotron radiation from a wiggler/undulator with permanent magnets, and will be served for circularly polarized VUV and soft X-ray experiments. This beam line is a unique beam line that can handle both wiggler/undulator radiation with the angular width of 7 mrad \times 3.5 mrad and the bending radiation of 5 mrad wide from B28. The extracted circularly polarized synchrotron radiation is fed to a grazing-incidence grating-monochromator, and synchrotron radiation from B28 to a double crystal monochromator for X-ray experiments.

The total power of the permanent wiggler/undulator is estimated to be 4 kW at the stored current of 500 mA. A special heat absorber made of copper was designed to withstand such high power synchrotron radiation. The absorber is wedge-shaped with an angle of 18.4 degrees to reduce the power density at the surface.

The BL-28 is located near the injection point where the kicker and septum magnets are placed for electron beam injection. Therefore the BL-28 have to pass through the 2.3 m-thick concrete shielding wall near the bending magnet B28 to transport the synchrotron radiation to the experimental hall.

AR-BL-1

The AR-BL-1 is a new beam line to be constructed at 6 GeV TRISTAN Accumulation Ring (AR). This beam line will be operated under parasitic operation of AR, and will be served for

Table 3.6.1 Summary of Beamlines in FY 1987

Beamlines	Affiliation	Source	Spectral range	Status
BL-1	Nippon Telegraph and Telephone Co. (NTT)	bending magnet (B1)	VUV and Soft X-ray	in operation
BL-2	KEK-PF	60-period permanent magnet undulator	Soft X-ray	in operation
BL-3	KEK-PF	bending magnet (B3)	VUV and Soft X-ray	under construction
BL-4	KEK-PF	bending magnet (B4)	X-ray	in operation
BL-5	KEK-PF	permanent magnet wiggler/undulator (under design)	VUV and Soft X-ray	under construction
BL-6	KEK-PF	bending magnet (B6)	X-ray	in operation
BL-7	University of Tokyo	bending magnet (B7)	VUV and X-ray	in operation
BL-8	Hitachi Ltd.	bending magnet (B8)	VUV and X-ray	in operation
BL-9	Nippon Electrical Co. (NEC)	bending magnet (B9)	VUV and X-ray	in operation
BL-10	KEK-PF	bending magnet (B10)	X-ray	in operation
BL-11	KEK-PF	bending magnet (B11)	VUV and Soft X-ray	in operation
BL-12	KEK-PF	bending magnet (B12)	VUV	in operation
BL-13	The Institute of Physics and Chemical Research ^{*)}	27-pole multipole wiggler	Hard X-ray	under construction
BL-14	KEK-PF	superconducting vertical wiggler	Hard X-ray	in operation
BL-15	KEK-PF	bending magnet (B15)	X-ray	in operation
BL-16	KEK-PF	53-pole permanent magnet wiggler/undulator	Soft X-ray	in operation
BL-17	Fujitsu Ltd.	bending magnet (B17)	VUV and X-ray	in operation
BL-18	ISSP and KEK-PF	bending magnet (B18)	VUV and X-ray	under construction
BL-19	ISSP and KEK-PF	permanent magnet multi-undulator	VUV	under installation
BL-21	KEK-PF	bending magnet (B21)	white, visible light and X-ray (branch line)	in operation
BL-27	KEK-PF	bending magnet (B27)	infrared and white	under installation
BL-28	KEK-PF	25-pole permanent magnet wiggler/undulator	circularly polarized VUV and Soft X-ray	under construction
AR Test Port	KEK-PF	bending magnet of Accumulation Ring (AR)	Hard X-ray	under installation
AR-BL-1	KEK-PF	41-pole multipole wiggler	Hard X-ray and Soft X-ray	under construction

*) Branch lines are constructed by following national institutes; National Research Laboratory of Metrology, National Institute of Research for Inorganic Materials, Electrotechnical Laboratory, and National Laboratory for Industrial Chemistry

hard and soft X-ray experiments such as angio-graphy, which use the synchrotron radiation from a 41-pole multipole wiggler, its amount of the total power being 3.7 kW.

3.6.3 Oxygen-discharge Cleaning of Mirrors and Gratings⁽⁴⁾

Mirror

The degradation in optical-element efficiency due to carbon contamination has long been recognized as a serious problem encountered in a synchrotron radiation beam lines. The resuscitations of carbon-contaminated mirrors and gratings were studied by oxygen-discharge cleaning in the Photon Factory. A test piece studied was the mirror which had been used as the first horizontal beam deflector at a 2° glancing angle in the undulator beam line (BL-2B)³⁾. The mirror is Pt-coated and made of CVD-SiC³⁾. Three portions with different degree of contamination before cleaning were shown in Fig. 3.6.1; a highly contaminated, narrow dark stripe along the center line (A), a round contaminated part with light brown (B), and the remaining portion (C). The contamination in (A) had been produced by highly brilliant radiation from the undulator under a relatively poor vacuum ($\sim 1 \times 10^{-7}$ Torr) in the initial period of the beam-line operation. The contamination in (B) might have resulted from a back flow of oil vapor, as it was directly facing a turbomolecular pump but had never been struck by radiation. No apparent contamination was seen in the part of (C). However, a close comparison of the part with a clean mirror revealed a slight change in color, which would also be caused by oil vapor. The measurement of reflectance showed that the degradation of reflectance was significant in the part of (A) and its reflectance was much lower than 1% over the entire energy range of measurement (see Fig. 3.6.1(b)). The spectrum for the part of (B) exhibited no feature of platinum but essentially similar features of carbon. The spectrum for the part of (C) also indicated an effect of contamination, though it still retained the spectral features of platinum.

Fig. 3.6.1(b) shows the history of reflectance recovery of the part (A) during the cleaning of the mirror^{2,3)}. The mirror was exposed to an oxygen plasma. The first high-power cleaning of about 45 W was made for 45 min. With this treatment, the contaminated overlayers were almost completely removed. The second cleaning was made at a low power of about 26 W for 35 min. Then the remnant of contamination disappeared and a satisfactory recovery of the reflectance to that of platinum was attained. In order to examine the effect of the exposure to reactive atomic oxygen, the mirror was further exposed to the plasma at a medium power of about 32 W for a longer time of 100 min. A slight improvement of the reflectance was observed for the photon energies below about 10 eV, while some decrease was observed above 10 eV. This should be ascribed to the change in optical properties of the surface (i.e., surface oxidation). The above facts indicate that there exists an optimum exposure time for the cleaning of mirrors.

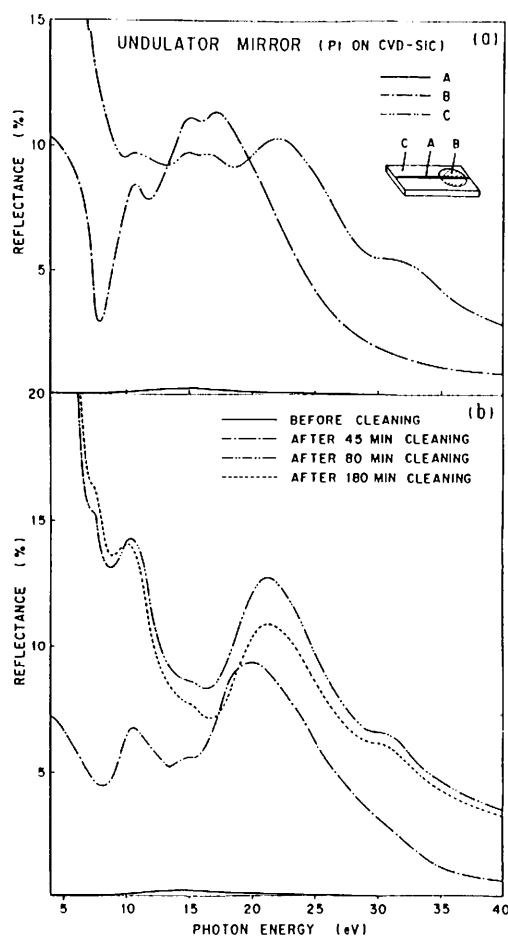


Fig. 3.6.1 (a) Reflectance spectra for three portions of an undulator mirror before cleaning at an angle of incidence of 20° . (b) Reflectance spectra for the highly contaminated central part (A) before and after three cleanings.

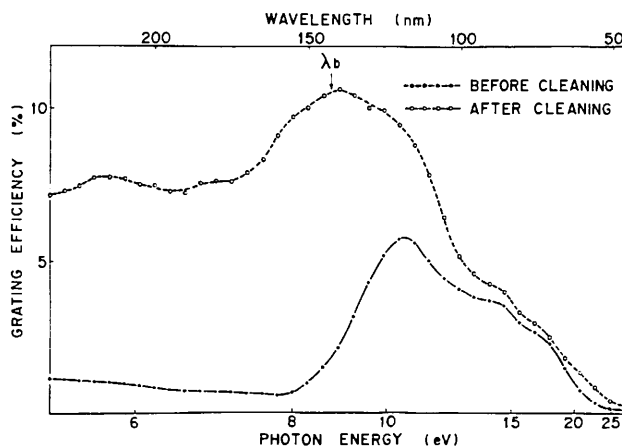


Fig. 3.6.2 Efficiency spectra of the inside-first-order of a 1200 lines/mm grating before and after the cleaning, obtained at an angle of incidence of 23° . The blazed wavelength at the angle of incidence is denoted by an arrow.

Grating

A recovery of carbon-contaminated gratings by using oxygen discharge cleaning had been studied. An gold-coated grating with 1200 lines/mm (blaze angle of $5^{\circ}10'$) used at an average pressure of about 3×10^{-9} Torr for about two years was adopted as a first sample grating. The contamination level was relatively low because of the good vacuum of the monochromator. Fig. 3.6.2 shows the efficiency of the inside first order spectrum for the grating before and after cleaning. The cleaning was made at a low power of about 19 W for only 10 min., and any trace of contamination did not remain after 8 min. The angle of incidence for the measurement was chosen to be 23° . The blazed wavelength at this angle of incidence was calculated to be 143 nm ($h\nu \approx 8.7$ eV) for the inside first order. The upper abscissa in Fig. 3.6.2 is a linear scale of the wavelength in order to give a clear view around the blazed wavelength. The spectrum before cleaning shows an apparent degradation in the efficiency below ~ 10 eV and the efficiency was less than or equal to 1% below ~ 8 eV. The cleaning increased the efficiency by one order of magnitude below ~ 9 eV. Further the measured peak spectrum agreed with the calculated blazed wavelength, which is denoted by an arrow in the figure. Before cleaning it was difficult to identify the peak spectrum. This feature indicates that the cleaning procedure can lead to a recovery of a grating blaze.

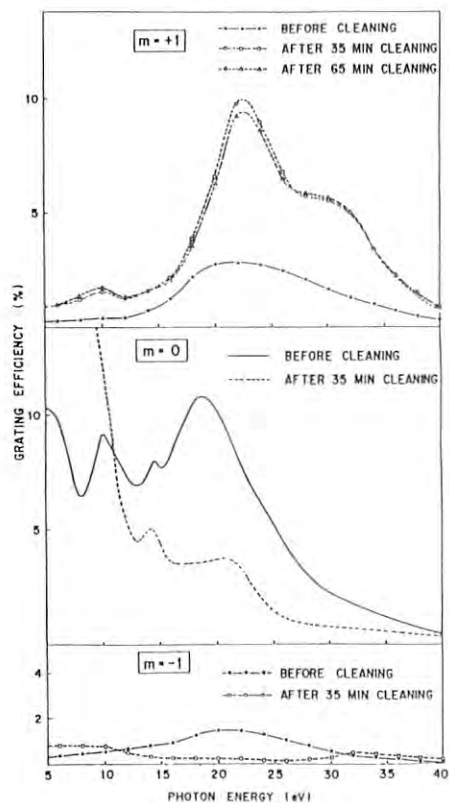
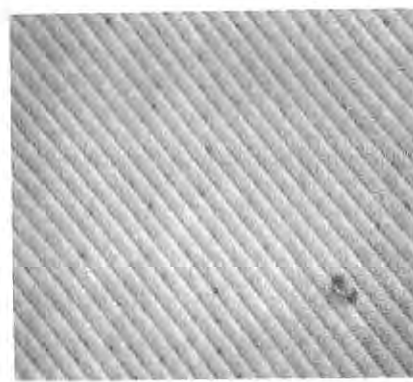
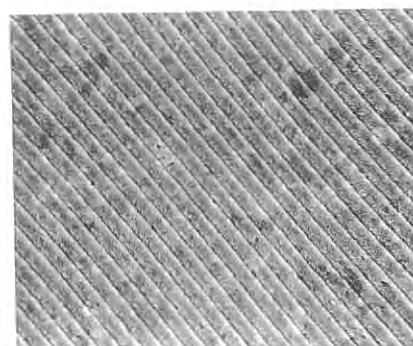


Fig. 3.6.3 Efficiency spectra for several orders of a 2400 lines/mm grating before and after cleaning, obtained in a constant-deviation geometry of $\alpha + \beta = 70^{\circ}30'$.

The next sample is an gold-coated grating with 2400 lines/mm (blaze angle of $4^{\circ}16'$), which had been used at a relatively poor vacuum of about 2×10^{-8} Torr for two years. In this case, the contamination level was very high. The cleaning was made at about 29 W for 35 min. As the result, the contamination disappeared completely even within 30 min. Figure 3.6.3 shows the efficiency spectra of several orders for the grating before and after cleaning. These spectra were taken under a constant-deviation geometry of $\alpha + \beta = 70^{\circ}30'$ (Seya-Namioka). Under this circumstance the blazed energy is approximately constant (about 24 eV for the inside first order) for the photon-energy scanning between ~ 10 and 40 eV. Before cleaning, the zeroth-order spectrum was by far highest among all diffracted orders over the entire energy range of measurement. In addition, the zeroth-order spectrum was similar to the reflectance spectrum of the contaminated mirrors both in shape and in magnitude. The spectra of both the inside and outside first orders showed a similar shape and had a comparable magnitude, and no apparent peak at the blazed energy was observed for the inside first order spectrum. All these optical properties



(a)



(b)

Fig. 3.6.4 SEM observation of the 2400 lines/mm grating (a) before and (b) after cleaning.

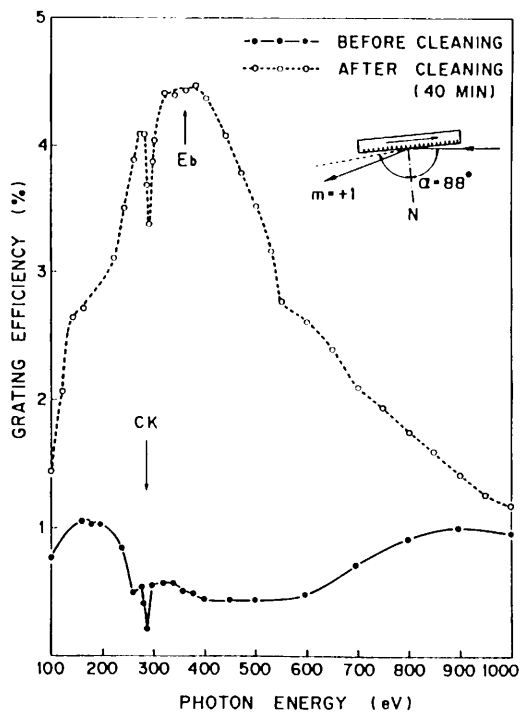


Fig. 3.6.5 Efficiency spectra of the inside-first-order of a 1200 lines/mm grating before and after cleaning, measured at an 88° angle of incidence. The positions of the carbon K edge and the blazed energy are denoted by arrows. The small dip at the carbon K edge after cleaning is not originated from the grating itself.

clearly show that the contaminated grating looked like a mirror.

The cleaning of the grating significantly improved its efficiency, especially over the energy range between 12 and 32 eV, except the efficiency of the zeroth order at high energies. From these experimental results, we can conclude that the inside-first-order efficiency around the blazed energy was improved by the recovery of the blaze and the efficiency at the other energy by the recovery of the reflectance of the coating material on the whole surface of the grating.

The conclusion is also supported by the measurement of the grating with scanning electron micrographs as shown in Fig. 3.6.4.³⁾ It can be seen that before cleaning the grating grooves were covered with contamination deposits, while after cleaning the sharp-edged structures of the original facets were recovered.

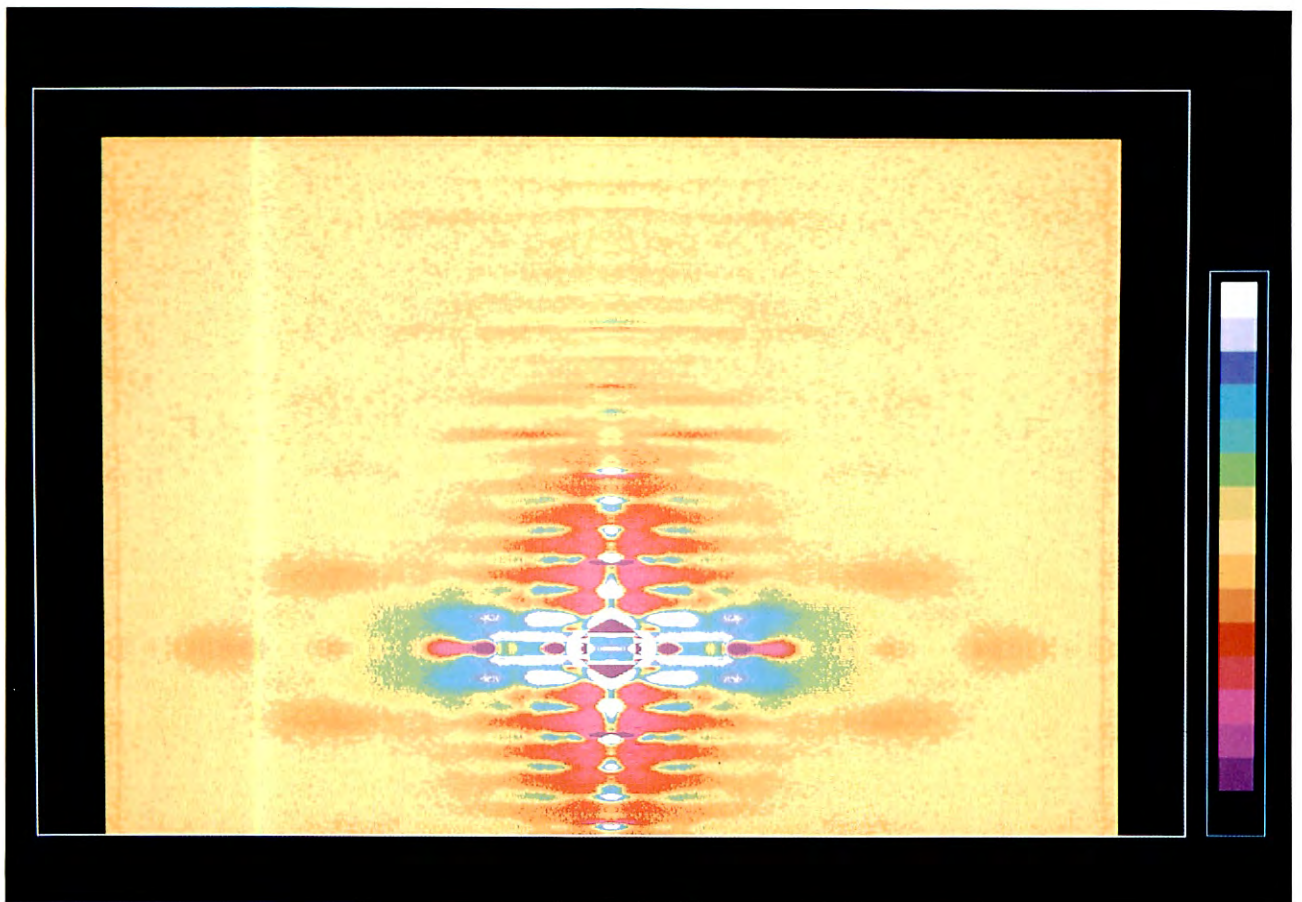
The grating was further exposed to oxygen plasma for 30 min. to find the optimum exposure time. This second discharge was made at a power of about 23 W. The results measured for the inside-first-order is shown in Fig. 3.6.3. The improvement of the efficiency was found to be negligible in this case. This fact indicates that the long-time exposure does not improve the efficiency so much. In other words, the recovery of the efficiency saturates within several minutes.³⁾ We measured the efficiency spectra of a gold-coated grating with 1200 lines/mm (blaze angle of $1^\circ 47'$) over the energy range from 100 to 1000 eV before and after cleaning of the grating.²⁾ The cleaning was made in two steps. The first cleaning was made at 22 W for 25 min, and the second at 21 W for 15 minutes. The measurement used a thin silver film as a filter for the region covering the carbon K edge. The inside-first-order efficiency was remarkably improved by the cleaning, but a deep dip still remained at the carbon K edge. This dip was also observed in the zeroth-order spectrum which can be compared with the usual reflectance spectrum. The depth of the dip is almost the same order as that observed in the reflectance spectrum of a "clean" platinum coated mirror. Thus we suppose that the K-dip is not originated from the remaining carbon layer on the grating surface but from the another origin, for example, carbon contamination of the spectroscopic system used during measurements. The remarkable recovery of the efficiency of the grating with a thicker (250 nm) silver filter is shown in Fig. 3.6.5⁴⁾. From these results it can be concluded that the grating efficiency has been significantly recovered and improved by a factor of 17 at the carbon K edge. It is also noted that the peak spectrum after cleaning agrees very well with the calculated blazed energy denoted by an arrow in the figure.

Other results of cleaning in the 100-1000-eV are given in the section for users' reports of this issue.

References

- 1) T. Koide, S. Sato, T. Shidara, M. Niwano, M. Yanagihara, A. Yamada, A. Fujimori, A. Mikuni, H. Kato and T. Miyahara, Nucl. Instr. and Meth. A246 (1986) 215.
- 2) T. Koide, M. Yanagihara, Y. Aiura, S. Sato, H. Kato and H. Fukutani, Phys. Scr. 35 (1987) 313.
- 3) T. Koide, M. Yanagihara, Y. Aiura, S. Sato, T. Shidara, A. Fujimori, H. Fukutani, M. Niwano and H. Kato, Appl. Opt. 26 (1987) 3884.
- 4) T. Koide, T. Shidara, M. Yanagihara and S. Sato, Appl. Opt. (to be published).

Instrumentation Department



*A processed small angle X-ray diffraction pattern from the frog muscle.
A resting pattern was subtracted from a contracting pattern.
Exposure time of each pattern was 10 sec.(BL-15A, Imaging Plate,
in collaboration with Osaka Univ.)*

1. BEAM LINES, OPTICS AND INSTRUMENTATION

1.1 Beam Lines and Optics

To meet increasing demands of light sources for scientific research and industrial applications, we have started construction of four new beam lines in the PF storage ring. These are (1) BL-16 which accepts brilliant synchrotron radiation (SR) from a newly designed multipole wiggler/undulator¹⁾, (2) BL-13, under the collaboration of the national laboratories in Tsukuba and KEK-PF, which utilizes SR from a multipole wiggler, (3) BL-17, under the collaboration of Fujitsu Laboratories and KEK-PF, which utilizes SR from a bending magnet and (4) BL-19, under the collaboration of the University of Tokyo and KEK-PF, which accepts brilliant SR from the revolver, a new type of undulator²⁾. Recently new scientific opportunities have been developed with SR of higher energy and we have decided to construct a new beam line at the TRISTAN Accumulation Ring which is operated at an accelerating energy of 6.5 GeV.

Besides the construction of new beam lines, continuous efforts have been made to improve the design and performance of the old beam lines.

In the following a description is given on the construction and improvement work done in 1987.

1) In this issue. Light Source Department.

2) In this issue. Light Source Department.

Beam Line 16

Beamline 16 is designed for use of radiation obtained from a 53 pole hybrid permanent magnet (NdFe and permendur) wiggler/undulator device installed in the straight section between the bending magnets 15 and 16. The maximum magnetic field of 1.5 tesla is obtained with a gap of 18

mm and a period of 12 cm. With a larger gap, the device can be operated as an undulator, the first harmonic of which covers a photon energy range of 40 eV - 400 eV. In the X-ray region, an intensity gain of about 100 is expected. The calculated spectra or brightness of the source can be found in last year's activity report (p.80).

The beam line consists of an undulator branch and a wiggler branch as schematically shown in Fig. 1. The undulator radiation is reflected sideways by a SiC mirror. A new monochromator of quasi-Rowland circle mounting is being designed for this branch line.

By translating the SiC mirror out of the beam line center, X-ray beams obtained under wiggler mode operation can be guided into the X-ray branch. Two 0.2 mm thick water cooled Be windows separate the ring vacuum from the beam line vacuum. Before the Be-windows 5 carbon foils of 0.1 mm thick are inserted to absorb the low energy part of the synchrotron radiation. The X-ray optics of this branch beam line is being constructed in three steps. In the first phase, only a sagittal focusing double-crystal monochromator is installed. In the second phase, a one-to-one vertically focusing mirror made of SiC will be installed before the monochromator. In the third phase, this mirror will be used as a collimating mirror to make the beam incident on the double-crystal monochromator. A refocusing mirror will be installed behind the monochromator. The beamline and the sagittal focusing monochromator will be commissioned in winter of 1987 - 1988. The estimated maximum heat load on the first crystal of the monochromator is 4 - 5 kW. A good solution is not yet found to handle such a big heat load. A cooling scheme to directly flow water in channels in the crystal is being considered.

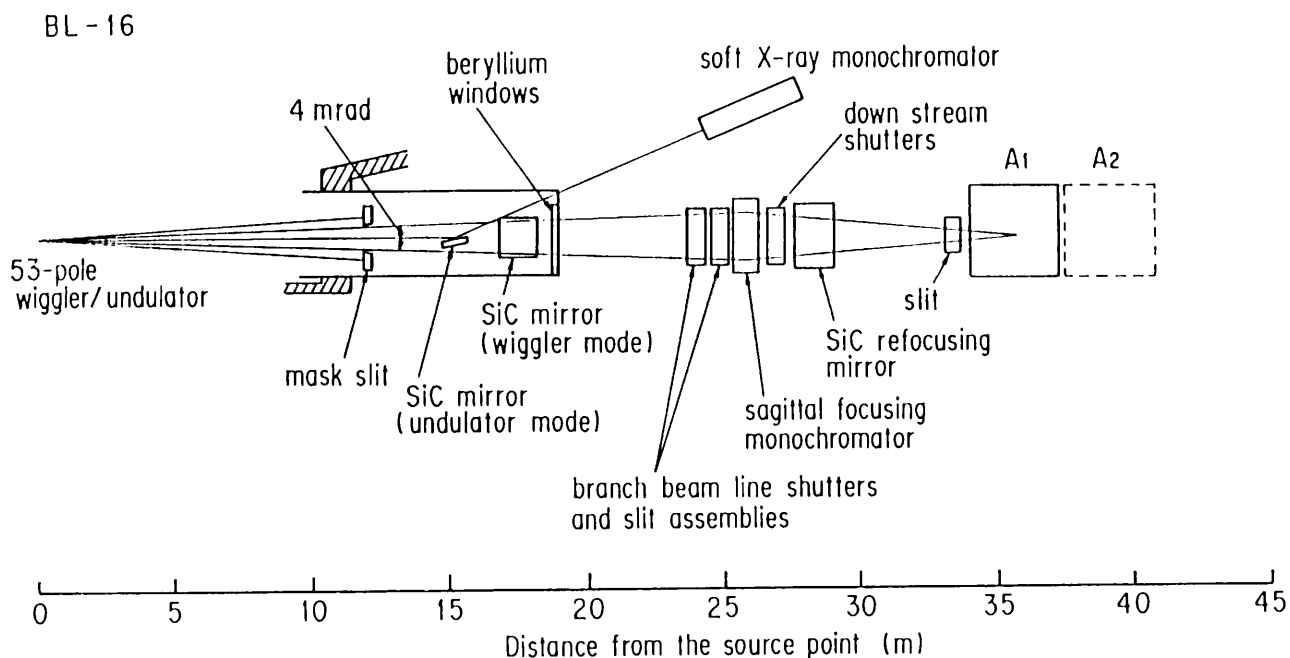


Fig. 1 Layout of Beam Line 16.

Beam Line 13

BL-13 is a newly constructed hard X-ray beamline which will utilize radiation from a multi-pole wiggler to be inserted in a straight section between the bending magnets B12 and B13. BL-13 has been designed and built by four national laboratories in Tsukuba* and the Institute of Physical and Chemical Research in collaboration with KEK-PF based on a project funded by the Agency of Science and Technology. Two branch beam lines BL-13A and BL-13B have been constructed in FY1986. A multi-pole wiggler and front-end section will be installed in FY1987. BL-13 has been designed to accept 5 mrad of radiation from a 29-pole wiggler magnet and additional 2 mrad for a future VUV branch beam line BL-13C. Although BL-13A and BL-13B are both hard X-ray beam lines separated with a front-end UHV section by Be windows, optical components and beam transport systems have been designed to be compatible with high vacuum (10^{-8} - 10^{-9} Torr) for future low energy experiments. Upstream masks and slits are placed in UHV chambers in front of Be windows ($200 \mu\text{m} \times 2$). A part (1 mrad) of the incident white X-ray beam (5 mrad) is split into BL-13A by a so-called branch beam line monochromator. A hard X-ray monochromatic beam is provided to the experimental hutch in BL-13A whereas either monochromatized or white X-ray beam is available at two experimental hutches BL-13B₁ and BL-13B₂, which are tandemly placed and used in a time-share mode.

Layout of BL-13 is shown in Fig. 2.

* National Research Laboratory of Metrology, National Institute of Research for Inorganic Materials, Electrotechnical Laboratory and National Laboratory for Industrial Chemistry

BL-13A

BL-13A is a hard X-ray branch beam line with an energy range of 4 - 30 keV. A branch beam line monochromator is a horizontal double crystal monochromator capable of providing a fixed output beam position. Asymmetrically cut Si crystals and a grazing incidence geometry are used to split the incident beam. The position of a second crystal goniometer mounted on a computer-controlled linear slide table which keeps the deviation of output beam position constant.

BL-13B

The optics of BL-13B consist of a sagittal focusing double crystal monochromator and a focusing mirror. In this monochromator, a mechanical link originally designed by Matsushita et al.¹⁾ is replaced by a computer controlled XY stage. Horizontal acceptance of this monochromator is 4 mrad and covers an energy range 4 - 25 keV using Si(111) and Si(220) reflections. A bent-flat mirror (Pt-coated fused quartz, 150(W) mm \times 580(L) mm) is placed behind the focusing monochromator, which is designed to (1) vertically focus the monochromatized beam and (2) reject higher harmonics to cover the energy range below 21 keV with a glancing angle of 4 mrad. Optical components are controlled through a CAMAC system by a 32-bit minicomputer (DGE, ECLIPSE MV7000).

1) T. Matsushita, T. Ishikawa and H. Oyanagi: Nucl. Instr. and Meth. **A246**, 377-9 (1986).

BL-13

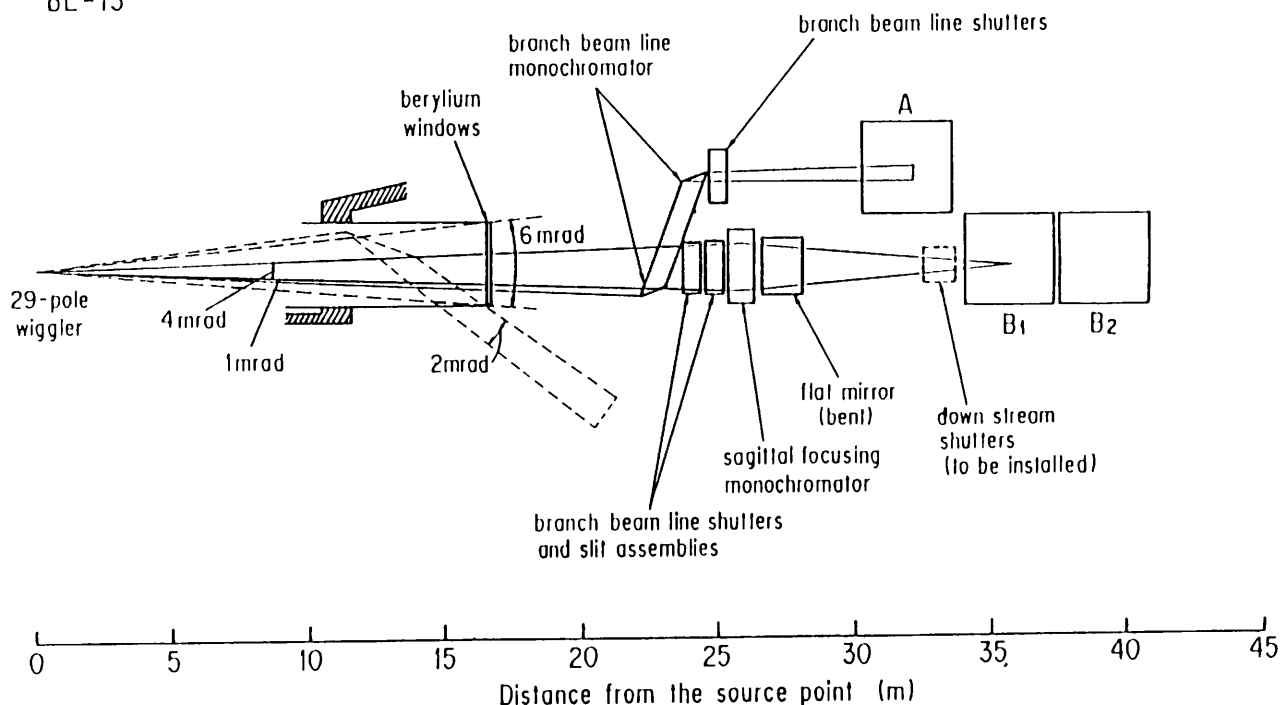


Fig. 2 Layout of Beam Line 13.

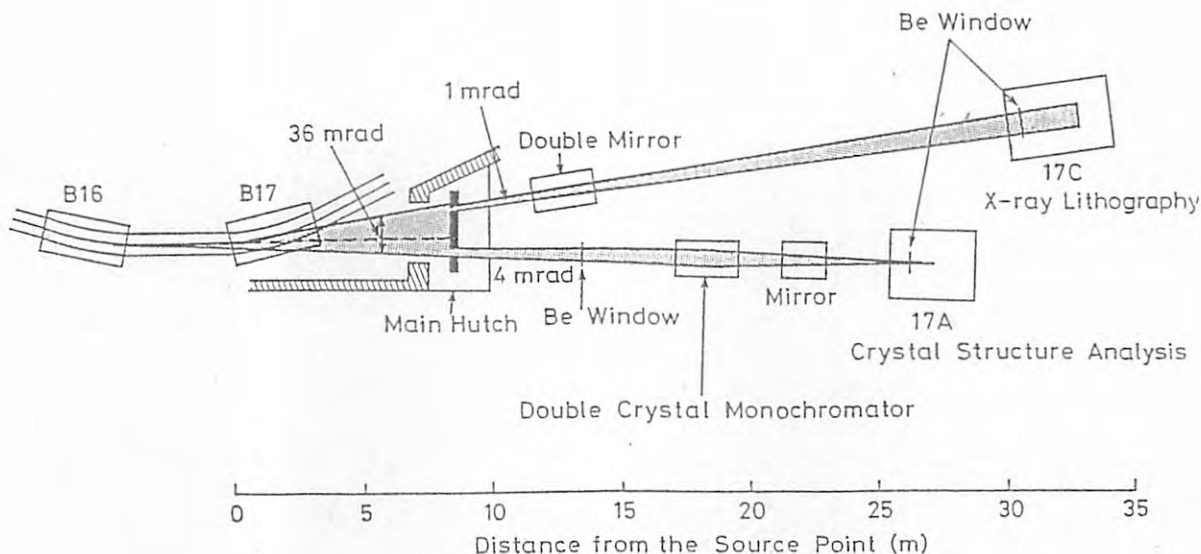


Fig. 3 Layout of Beam Line 17.

Beam Line 17

This beam line is designed for experiments of X-ray diffraction, photochemical reaction and X-ray lithography. The line consists of three branch lines, BL-17A, 17B and 17C. The bending magnet B16 generates radiation with a divergence of 6 mrad and the bending magnet B17 radiation of a divergence of 30 mrad and therefore the total horizontal divergence is 36 mrad. The layout of the beam line is schematically shown in Fig. 3. Construction of BL-17C, which accepts radiation of 10 mrad, was completed in May 1987. BL-17A, which accepts radiation of 6 mrad, is now under construction. The last element to be constructed, BL-17B, will be used for photochemical reaction studies. The beam line was designed and constructed by Fujitsu Laboratories Ltd. in collaboration with KEK-PF. A side view of the beam line is shown in Fig. 4.

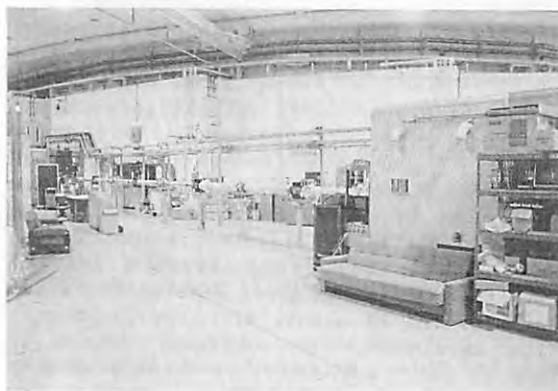


Fig. 4 A side view of Beam Line 17.

Front End

The basic design of the front end is similar to that of BL-11 constructed by KEK-PF. The front end provides protection from radiation hazards and accidental vacuum breakdown at the branch lines. A beam shutter is installed for personnel protection. A water-cooled absorber protects the beam shutter and pneumatic valves from overheating due to the bombardment of synchrotron radiation. A fast closing valve (FCV) and an acoustic delay line (ADL) were installed to protect the storage ring from accidental vacuum breakdown. The closing time of the FCV is less than 30 ms (including the response time of the sensor located downstream of the ADL). The measured delay time of the ADL was longer than 100 ms, which is short enough to close the FCV.

BL-17C

This branch line is designed for X-ray lithography. The line is evacuated to 10^{-9} Torr, and a Be window (20 mm diameter) separates the line from the atmosphere. Exposure experiments

are carried out in the exposure chamber in a He gas atmosphere. Fused quartz mirrors and a Be window serve as the band-pass filter and are used to limit the wavelength region (0.2 nm to 2 nm) to be suitable for X-ray lithography. To keep the reflected beam horizontal, double parallel plane mirrors are set up. A white beam can also be obtained by removing the mirrors. A vertically movable Be window is installed in order to enlarge the exposure area by oscillating the second mirror. Preliminary experiments have been done using this branch line.

BL-17A

This branch line is now under construction and will be used for EXAFS measurements, X-ray diffraction studies, and photoelectron spectroscopy. Using the double Si and InSb crystal monochromator located 21 m from the source point (the bending magnet B16), monochromatic X-rays with a wavelength in between 0.1 nm and 0.7 nm will be obtained. The beam will then be focussed by a sagittally focusing technique. To reject higher harmonic components, a Pt coated fused quartz mirror will be installed at a distance of 26 m from the source point. Crystal structure determination will be carried out at this branch line.

Beam Line 19

Construction of beam line 19 is now proceeding under collaboration between the Synchrotron Radiation Laboratory of the Institute for Solid State Physics, the University of Tokyo (SRL-ISSP) and KEK-PF. This beam line is designed to accept radiation emitted from an undulator¹⁾, called a revolver, and divided into two branch beam lines, BL-19A and BL-19B. BL-19A will include a grazing incidence monochromator, which will cover a photon energy range from 20 to 300 eV and will be devoted to spin-polarized photoelectron spectroscopy. BL-19B will cover a photon energy range from 10 to 1000 eV by means of a plane grating monochromator and will be dedicated to the photoelectron spectroscopic studies of solids at various temperatures. At present (August 1987), only the construction of the front-end of the beam line is completed. The construction of the whole system including experimental apparatuses will be finished in the summer of 1988.

- 1) Activity Report of SRL-ISSP, the University of Tokyo 1986

Beam Line at the TRISTAN Accumulation Ring

The PF storage ring has a wiggler beam line BL-14 from which high energy X-ray photons are available. Each of three stations accommodates an experimental set up optimized for the vertical polarization of X-rays available from the magnetic field. At BL-14A mostly protein crystallography is under way using either a four circle diffractometer or the Arndt camera; EXAFS measurements for the 4f metals are also performed. At BL-14B development of Mossbauer source fabrication is under way, where vertical axes are also used as goniometers. In case of multiple precision axes this function is quite useful in arranging goniometers on the same horizontal incidence plane. The energy used there is 14.4 keV. At BL-14C a high resolution Compton scattering experiment is under way. Further there exists a great amount of demand for high energy X-ray photons from high pressure-high temperature experiments, angiography, nuclear excitation by electron transition and magnetic scattering by 4f metals.

On the other hand, the fundamental energy of an undulator spectrum is proportional to the square of the ring energy, and, if undulator X-ray photons greater than 10 keV in energy are required, it is necessary to proceed to a higher energy storage ring.

Under these requirements, recently a design has been started for a beam line using an insertion device in the TRISTAN Accumulation Ring (AR) which is currently used as an injector into the Main Ring. The machine parameters of AR are as follows; energy: max 6.5 GeV; current: 20 mA; field strength: 0.86 - 0.93 T; bending radius: 23.3 m; critical photon energy: 26.4 keV; number of straight sections for the insertion devices: 2; emittance: 310 nm·rad (present) and 130 nm·rad in the near future.

In this year a device producing circularly polarized SR is under fabrication. This particular beam line is designed so that one can perform magnetic Compton scattering experiments with 60

keV X-ray photons. Of course normal Compton scattering experiments are also possible. Furthermore, a double-crystal monochromator to be installed will provide us with monochromatic parallel circularly polarized X-ray photons with a fixed exit beam position.

Improvement of AR as a synchrotron radiation source will naturally be necessary; Especially a much longer life time of beams and the stability of an electron orbit over a long period is quite crucial. So far the longest life time is only 60 minutes and the beam deviation is 1.5 mm. Brilliant SR from the insertion device will be needed in a couple of years. In order to meet this requirement, joint work between the TRISTAN group and the PF group is now being planned.

Beam Line 1

In this beamline, the branch beam lines were modified this year as follows;

- (1) At BL-1A a low conductance beam duct with a 160 l/sec ion pump was introduced in order to decrease the effect of gas desorption from the pre-mirror to the beam splitting section and to utilize the whole SR beam. A laser port for adjustment of the beam axis was also installed.
- (2) At BL-1B a vacuum chamber for photo-stimulated desorption experiments by synchrotron radiation was set. Furthermore, this branch beam line was split into two by inserting a 6 deg Pt coated fused quartz mirror, one a conventional straight line for the short wavelength X-ray lithography, and the other a new line for long wavelength X-ray lithography. This splitting is for the effective use of BL-1B.

At BL-1A, we succeeded in the soft X-ray monochromatization as well as VUV monochromatization by using the Grating/Crystal Monochromator (GCM) for the first time. This monochromator was installed at BL-1A in order to provide a monochromatic beam with an energy ranging from VUV to soft X-rays, namely from 50 eV to 5 keV, for the combined surface analysis of photoemission spectroscopy, surface EXAFS, and other kind of analysis of solid samples such as semiconductors. Last year VUV monochromatization was performed in the energy range from 50 eV to 400 eV by using a 1200 g/mm grating. This year synchrotron radiation in the 400 - 900 eV range was monochromatized by using 2400 g/mm grating with a 2 deg blaze angle under the "on blaze" condition which is a merit of the GCM. An oxygen K-edge EXAFS measurement of several oxide films including GaAs plasma oxides was carried out using this monochromatic beam.

Then, the plane mirror and the grating were changed into the InSb double crystal in the GCM. By developing original energy scan software, soft X-rays in the energy range from 2.7 keV to 4.0 keV were successfully monochromatized. The photocurrent measured with an Au photocathode was about 20 pA. A Cl K-edge EXAFS measurement was carried out on a cleaved NaCl crystal and a Cl-contaminated Si substrate by detecting Cl K α radiation by using this monochromatic beam. However there are still some problems to be

solved such as widening of energy range of monochromatic soft X-rays, stability of the monitor and sensitivity of the detector.

One more topic to be noted is the striking improvement of the FWHM of the zero order beam profile in the low emittance operation mode of the PF ring which started in February 1987. Since the FWHM of the beam was broad in the normal emittance mode, about 1 mm in vertical and 4 mm in horizontal size, at BL-1A, an entrance slit of 500 μm in vertical width was placed in order to obtain high energy resolution. In the low emittance mode where the source size is about 0.3 mm in vertical and 1.0 mm in horizontal, it is found that the same energy resolution and several times brighter beam can be obtained without using the entrance slit. Therefore the low conductance duct has been installed in front of the pre-mirror located at the distance of 17 m from the source point.

Beam Line 7

The construction of BL-7 was completed in 1986 under collaboration between the Research Center of Spectrochemistry, University of Tokyo and KEK-PF. Performance test of the beam line optics and significant improvements were repeated in 1986/1987. A view of BL-7 is shown in Fig. 5. The present status of the branch lines is summarized below. Some characteristics of BL-7A and BL-7B are presented in the user's short report section.

BL-7A

Several improvements of the pre-focusing mirror apparatus and of the plane grating monochromator were successfully performed. Some of them are: (1) modification of the support system of the pre-focusing mirror, (2) adaptation of a new material (SiC) for the grating substrate and setting up of a cooling system for the grating, (3) modification of the diaphragms and the slit mechanism. After these improvements, preliminary experiments of X-ray photoelectron spectroscopy and surface EXAFS were started.

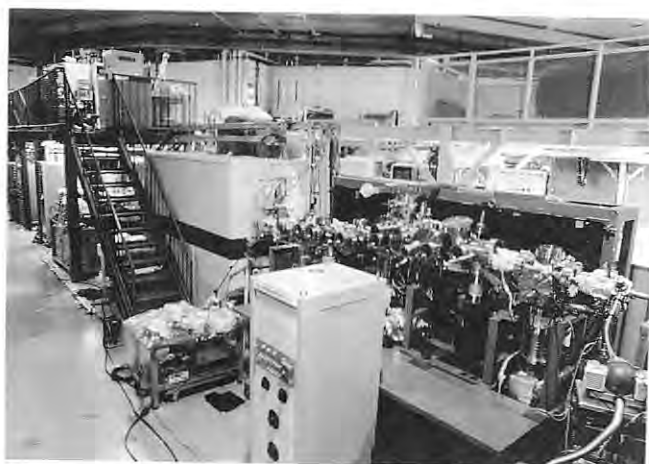


Fig. 5 A view of Beam Line 7.

However, degradation of the grating surface due to impingement of intense synchrotron radiation, previously observed in the performance test, has not been completely overcome yet.

BL-7B

The main modifications were as follows. The first pre-focusing mirror made of copper (OFHC) was reshaped by the KEK-Workshop. By using the new mirror, the beam size at the sample position and the photon intensity have greatly been improved. A water cooling system for the first mirror was set in the pre-focusing mirror apparatus in order to diminish shift of the beam position on the entrance slit of the monochromator.

BL-7C

Stabilization of the vertical beam position and focusing of monochromatic beam have been performed since September 1986¹⁾. Movement of beam height due to the change in Bragg angle is decreased to 0.2 mm for the photon energy range from 4 to 18 keV using Si(111) flat double crystals. The main reason of this movement is the difference in the lattice constants between the first and the second crystals. Focusing of the beam using a sagittal focusing monochromator²⁾ has been attempted. The photon flux through a hole 6 mm wide and 1 mm high was 2×10^{10} photons/s around the energy of 7 keV when the storage ring was operated at 2.5 GeV and 100 mA, which was about ten times larger than that obtained without focusing. At this time, the width of the rocking curve was not increased seriously and the intensity ratio of higher harmonics decreased to a tenth.

Control of the monochromator and data acquisition of absorption spectra is performed using a microcomputer (NEC PC-9800E)³⁾. The data stored in the computer can be transferred to a large scale computer (FACOM M360MP).

An example of fluorescent EXAFS spectra is shown in Fig. 6. An aqueous solution of copper(II) sulphate of 1 mmol/dm³ conc. was used and data accumulation was done within one hour using a fluorescent EXAFS detector⁴⁾. Absorption spectra of more dilute aqueous solutions and those of lighter elements such as K, Ar, Cl were also measured at this station.

1. Photon Factory Activity Report 1986 p.90 (1987).
2. T. Matsushita, T. Ishikawa and H. Oyanagi, Nucl. Instr. and Methods, A246, 377 (1986).
3. M. Nomura, KEK Internal 87-1 (1987).
4. F. W. Lytle, R.B. Gregor, D.R. Sandstrom, E. C. Marques, J. Wong, C.L. Spiro, G.P. Huffman and F.E. Huggins, Nucl. Instr. and Methods, 226, 524 (1984).

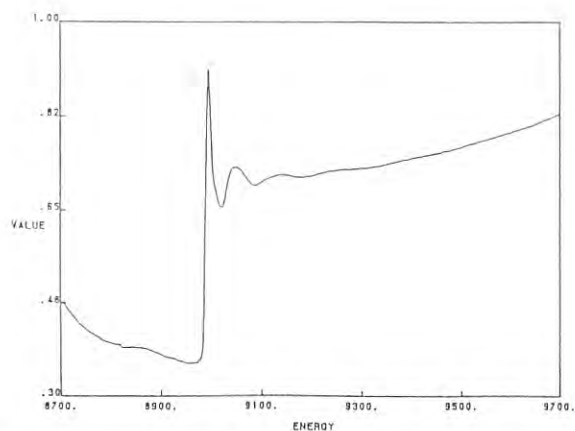


Fig. 6 A fluorescent EXAFS spectrum of 1 mmol/dm³ copper (II) aqueous solution. BL-11B

Serious trouble has been observed in optical elements in this branch beam line owing to high-current operation of the storage ring. The first mirror was damaged and the temperature of the first crystal of double-crystal monochromator was increased. The set-up of the beam line and monochromator have been already reported¹⁾.

Many cracks were found on the surface of the first mirror (Pt coated bent cylindrical one made of quartz), though contamination was not so serious in the summer shut-down of 1986 (Fig. 7), resulting in a rather large focus size. The mirror was replaced by a new one during the spring shut-down of 1987. A large carbon foil 5000 Å thick²⁾ was installed on the entrance mask of the mirror in order to absorb low energy photons and to reduce the heat load of the mirror as much as possible. After this improvement it has been working without any damage. It seems that the cracks occurred not on the surface Pt layer but on the quartz surface. After the replacement, the focus size of the beam became smaller.

How to reduce the heat load induced by the focussed white beam illumination is an important matter. As the monochromator is located near to the focal point, the power density becomes very high (5 W/mm²). For example, aluminum foil and

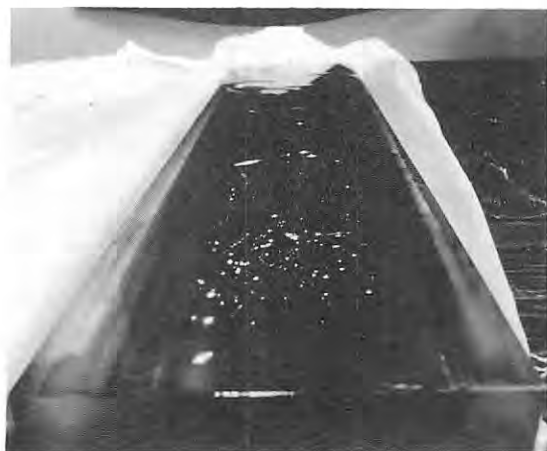


Fig. 7 Damaged cylindrical mirror. The photo is taken from back-side of the mirror.

graphite foil placed in front of the first crystal evaporated within a time as short as 30 sec when irradiated and tungsten mesh became red in color.

When the lattice constant of the first crystal increases owing to a temperature increase, the beam position moves as a result of the change in Bragg angle. The software controlling the monochromator was improved in order to fix the beam position even when the lattice constants of the two crystals are different. Also the double crystal monochromator optimization method was improved. The temperature measured on the side face of the crystal using a thermo-couple was about 150 - 200 °C. However, the first crystal (InSb) melted during the run of July 1987 (melting point is 525 °C, see Fig. 8), being due to the low thermal conductivity of the crystal (about a tenth of that of Si). If the beam is accidentally focused on the crystal, it will melt when its thickness is larger than 3 mm. Thinning of the crystal and design of a cooling system is in progress.

- 1) T. Ohta, P.M. Stefan, M. Nomura and H. Sekiyama, Nucl. Instr. and Methods, A246, 373 (1986).
- 2) The carbon foil was kindly prepared by Mr. Sugai of Institute of Nuclear Science, University of Tokyo.

BL-12C

This branch line was constructed originally for soft X-ray spectroscopy using a 10 m grazing incidence monochromator (10-GIM). After moving the 10-GIM to BL-2B, this branch line has been reconstructed so that either monochromatized radiation in the energy region of 1.8 - 4.0 keV or white radiation below 4.0 keV in energy can be selectively used.

The optics consist of a Pt coated SiC plane mirror and a channel cut InSb(111) crystal monochromator. The mirror is placed 29 m downstream of the source point and deflects the beam up-ward by 2 degrees. The crystal monochromator is located 31.3 m downstream of the source point and provides monochromatized radiation. At the

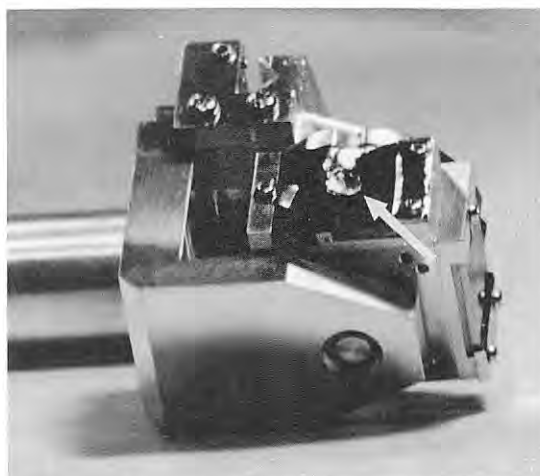


Fig. 8 Molten InSb crystal. An arrow indicates the hollow created by melting.

end of this branch line, several kinds of experiments including radiation biology and SR lithography have been performed.

Beam Position Monitoring at Branch Beam Lines

A stable and reproducible beam position is very important for all experiments using synchrotron radiation. The positional stability of the

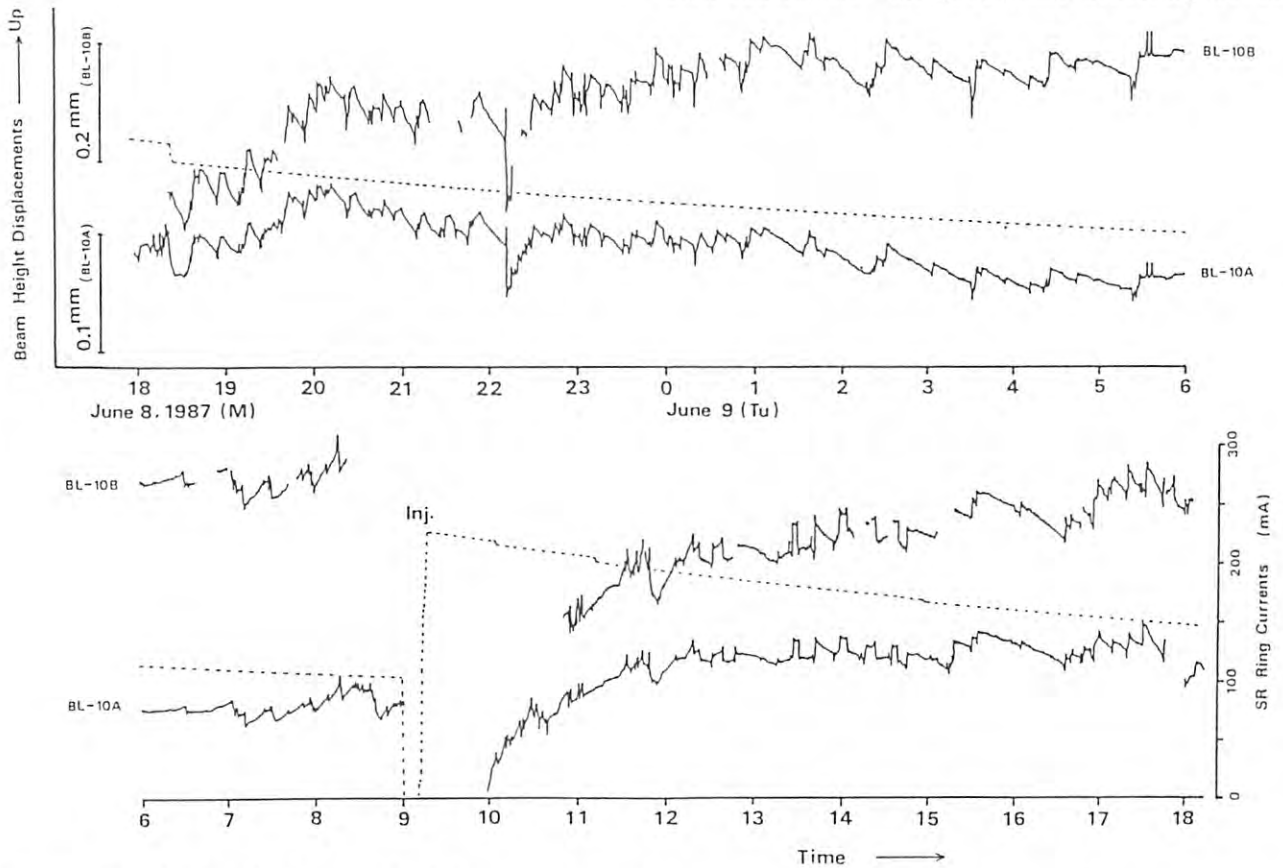


Fig. 9 The drift of the vertical beam position measured at BL-10A and BL-10B stations during the period of June 8th to 9th, 1987.

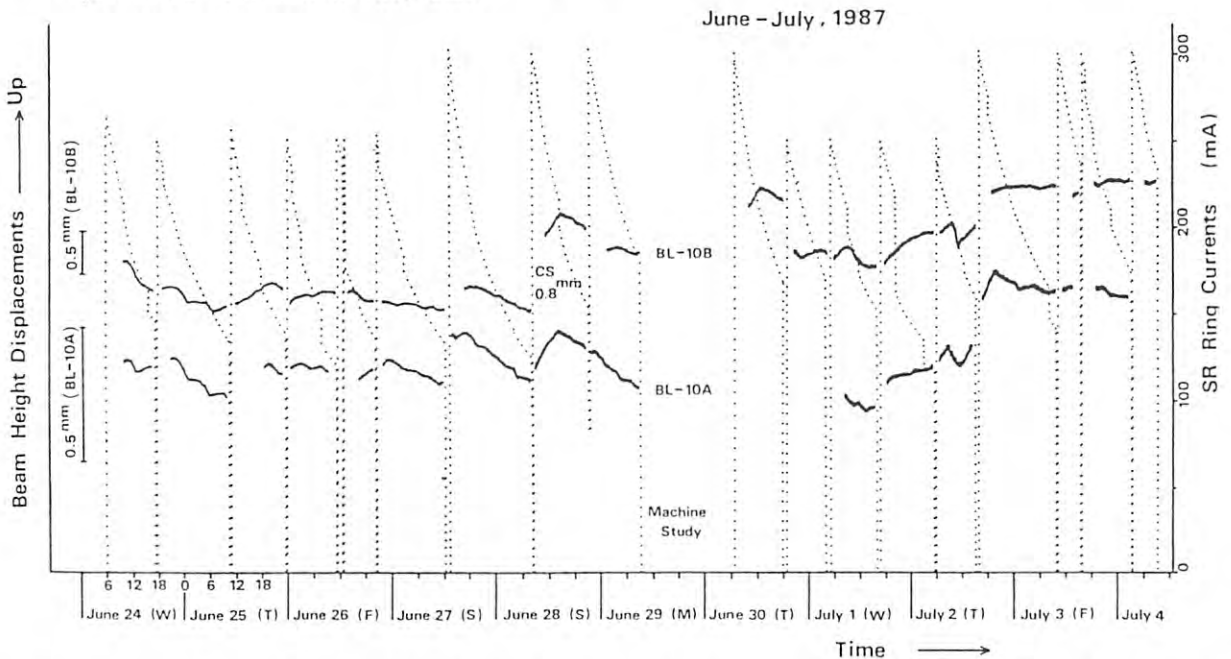


Fig. 10 The movement of the vertical beam position at BL-10A and BL-10B during the period from June 24th to July 4th, 1987. The dotted line shows beam current of the storage ring in mA. Measurements were made with a vertical-type wiggler, corresponding to 250 mA injection of electrons, and without the wiggler (300 mA injection). The lower solid lines are the beam position displacements measured at BL-10A, and upper ones are of BL-10A.

primary photon beam is sensitively dependent on the stability of stored electron orbit near the bending magnet. In particular, small angle changes of the orbit near the source point induce a shift of the beam position which is dependent on the distance. Therefore, the photon beam position should be monitored near experimental stations to serve as a sensitive indicator of stability.

Except the beam line BL-21, which is for the monitoring of beam position by the Light Source department, we have already installed and operated seven photon-beam position monitors in the front of monochromators and/or mirrors of the following experimental stations: BL-10A (split-anode type ionization chamber), BL-4C, BL-6B, BL-6c, BL-7C and BL-10B (monitor using slit blades) and BL-11B (photoemission wire monitor). Description of each type of monitor is given in the previous report (see Photon Factory Activity Report, No. 4, 1986, pp.66-71, pp.91-92).

Most recent measurements of the displacements of the vertical beam-position (beam height) were made during the experimental time at the BL-10A and BL-10B stations which are located at a distance of 12 and 24 meters from the same source point, respectively. Figure 9 is the record of beam movements for one day (June 8-9, 1987). It shows at maximum 0.1 mm (BL-10A) and 0.2 mm (BL-10B) drift, suggesting the existence of an inclination of the electron orbit. Since February 1987 digital feedback with the COD correction has been applied to reduce the drift of the beam position. Figure 10 is the same kind of diagram obtained for two weeks. Maximum displacement of vertical beam-positions is 0.5 mm and 1 mm at BL-10A and BL-10B, respectively.

The Light Source and Instrumentation Department jointly examined the effect of analog

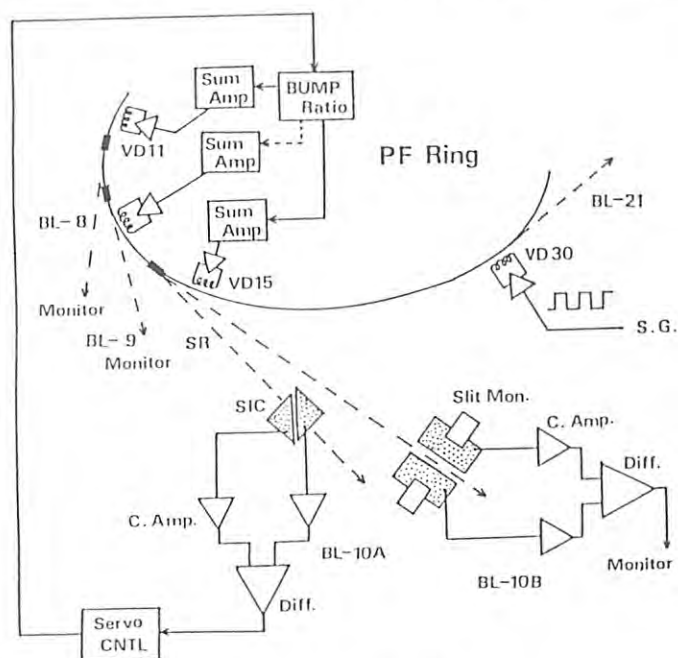


Fig. 11 Analog Feedback

The schematic diagram of the beam steering servo and monitoring systems used in the analog feedback experiments last December.

feedback on each beam line in December 1986. The localized beam-bump of the orbit was produced by two dipole magnets (VD11 and VD15 in Fig. 11) and the beam position movements were monitored at almost all beam lines around the ring. Part of the results are shown in Fig. 12. The suppression effect of a rectangular modulation generated at BL-21 is clearly seen for the beam lines (BL-8,9,10) which are controlled, while there is little effect for the beam lines outside the bump.

1.2 Instrumentation

Four-Circle Diffractometer with a Crystal Analyser

X-ray scattering and diffraction measurements provide information on the structure of matter on the atomic scale and have become the most useful technique for research in physics and materials science. In these researches it is often required to make measurements of scattering and diffraction intensities over a limited volume in reciprocal space but with a high momentum (Q) resolution. Intensity measurements on samples subjected to variable temperature and pressure conditions are also required to detect structural changes. A conventional four circle diffractometer is not necessarily suitable to these measurements and we have constructed a new diffractometer for the study of structural phase transitions and structural fluctuations in solids.

The main part of the diffractometer is based on a Huber 5020.4 four-circle diffractometer for vertical arrangement. Its characteristic fea-

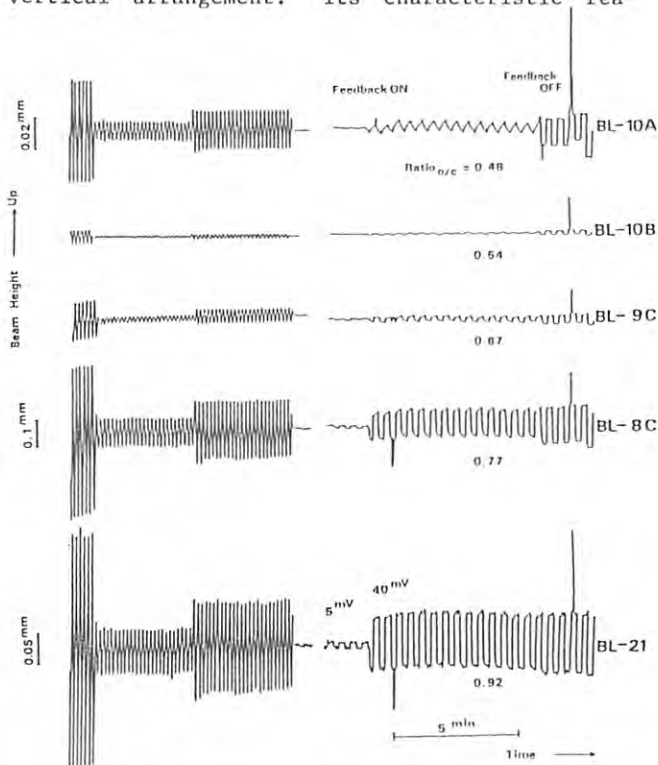


Fig. 12 Observations of the vertical beam position movement with the analog feedback system. The left-side sine curves are the results of examining the sensitivity of each monitor.

tures are (a) large χ, ω and 2θ circles which enable us to make precise angle-setting easier, (b) off-center positioning of the χ -circle on the ω -circle table which allows a cryostat or high-pressure cell to be put on the ϕ -circle table and (c) a crystal analyzer on the 2θ arm which receives scattered (diffracted) beams with small divergence and eliminates fluorescence radiation from the sample. The diffractometer is fixed on a large mounting table which can adjust, with the aid of stepping motors, the position of the diffractometer with respect to the incident SR beam. A scintillation counter is used to detect scattered (diffracted) beams. Acquisition of intensity data and control of the diffractometer and the mounting table are performed through CAMAC modules with a mini-computer (PDP 11/23).

In order to obtain better performance of the diffractometer, several devices were made and used successfully. One is a centering device fixed to the χ -circle which makes a narrow incident beam to pass exactly the intersection point of the axes of the χ - and ϕ -circles. Another is a remote-control entrance slit system which changes the size and shape of the incident beam cross section and makes positioning of sample easier.

With the use of laser optics the accuracy of the diffractometer angle setting was measured with the results (in sec of arc):

	2θ	ω	χ	ϕ
full rotation	39	30	/	34
local rotation	4	8	9	/
reproducibility	< 2	< 2	< 2	< 2
backlash	27	12		14

The diffractometer is installed at BL-4C where monochromatic radiation from a sagittally focusing double crystal (Si) monochromator¹⁾ is available. With Si crystals as a sample and an analyser, measurement of the resolution function was made following a method shown by Pynn et

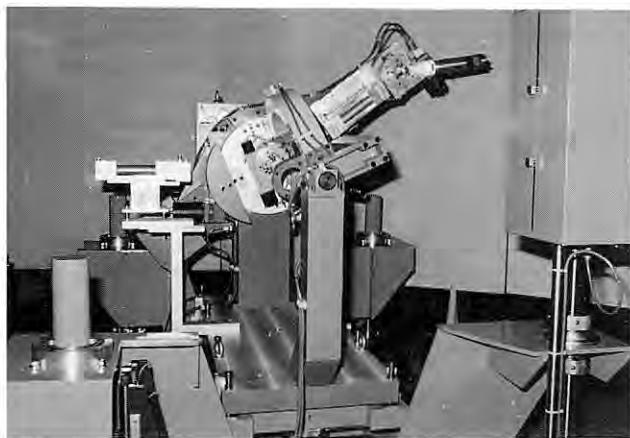


Fig. 13 Four-circle diffractometer with a crystal-analyser, fixed on the mounting table.

al.²⁾ The configuration of reflecting planes is $\text{Si}(111)^- - \text{Si}(111)^+ - \text{Si}(400)^- - \text{Si}(111)^+$. SR of the wavelength of 0.1387 nm was used. This method has given a section of the resolution function by a plane of diffraction (containing k_0 and k vectors) and it has elliptical shape of the diameter $58 \times 10^{-4} \text{ nm}^{-1}$ in the direction of $k - k_0$ and $36 \times 10^{-4} \text{ nm}^{-1}$ in the direction perpendicular to it.

Figure 13 shows a photograph of the diffractometer on the mounting table.

Typical experiments recently done using the diffractometer are: (a) precise measurement of X-ray diffuse scattering from the surface of Si crystals, (b) separation of the intensity profile of ion implanted Si crystals into dynamical and kinematical components, (c) observation of pressure-induced commensurate incommensurate phase transitions in $\{\text{N}(\text{CH}_3)_4\}_2\text{MnCl}_4$, (d) observation of the temperature dependence of planar diffuse scattering from β' -AgZn.

- 1) T. Matsushita, T. Ishikawa and H. Oyanagi: Nucl. Instr. and Meth. **A246**, 377-9 (1986).
- 2) R. Pynn, Y. Fujii and G. Shirane: Acta Cryst. **A39**, 38-46 (1983).

Weissenberg Camera for Macromolecular Crystallography

The first Weissenberg camera for macromolecular crystallography was designed and constructed for the recording of many reflections up to high resolution from a crystal with large unit cell dimensions (N. Sakabe, J. Appl. Cryst. (1983) **16**, 542-547, Photon Factory Activity Report (1983/84 V-7)). A second camera was built taking into account the experiences gained using the first camera. This camera utilizes a curved PSPC detector for the precise alignment of the crystal axis. Figure 14 shows a plane and a side view of the optical bench, the monochromator, and the main components of the camera. The most prominent feature of this camera is that an independent stepping motor is attached to each drive shaft for film translation and specimen rotation. By changing the rotation speed of each of the motors, overlap of the reflection spots on the imaging plate (IP) can be avoided, and as many reflections as possible can be recorded on all layer-lines. The maximum distance the film cassette can move is limited to 40 mm because it is not necessary to exceed the distance between two adjacent layer-lines on a film. The translation speed of the film is changeable from 0.005 mm/min to 0.4 mm/min, and the rotation speed of the specimen is variable from 0.005 to 2.0 °/min. The two speed ranges are independently changeable. The film translation and the sample rotation can also be synchronized.

All motors can be controlled from the keyboard of a NEC-PC9801. The radius of the film cassette can be set to either 143.25 mm, 286.5 mm, or 430.0 mm, an angle of one degree in θ corresponds to a distance of either 5 mm, 10 mm, or 30 mm on the film, respectively. Up to four layers of film can be used when the multiple film method is utilized. The space between the specimen and film or IP can be filled with helium gas to reduce background noise and X-ray absorption by air. The rotation axis of the specimen

can be adjusted from -10° to 30° in the horizontal plane to record as many independent reflections as possible from higher order layers. In principle, this camera does not require a layer-line screen but the use of a multi-layer-line screen improves the S/N ratio. This screen is mounted on a screen holder, which in turn is mounted on a cylindrical support. A number of adjustments are provided to allow remote alignment of the crystal axis with the rotation axis. The rotation axis (ω) is also moved along the parallel direction to the ω axis by a z direction shaft driven with a stepping motor. In addition, two arcs mounted perpendicular to each other allow for angular alignment in the X-Y direction. This enables precise alignment of the crystal axis with the rotation axis. It is possible to mark four fiducial points of the incident beam on the film or IP by using a remotely operated electro-magnetic shutter provided for this purpose.

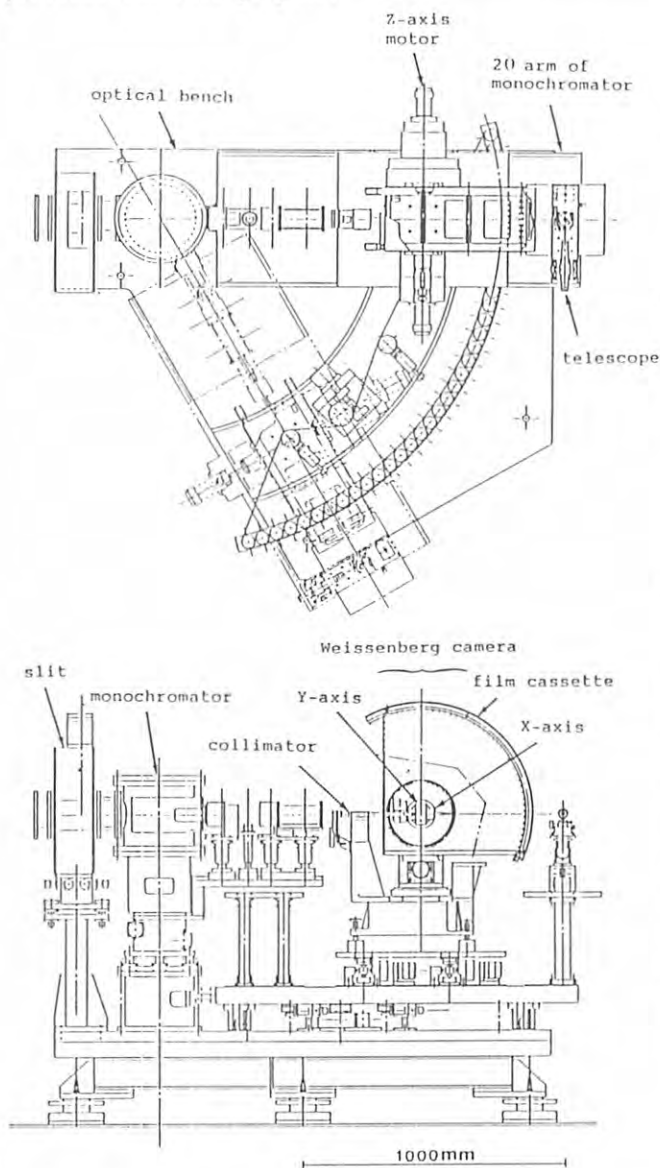


Fig. 14 Weissenberg camera and monochromator system.

Camera Specifications:

a. Film cassette

	1	2	3
Radius of film cassette	143.25 mm	286.5 mm	430 mm
Angular range (2θ)	-90° to 110°	-28° to 120°	-19° to 100°
Usable width of cassette	200 mm (max. 270 mm)	190 mm or 240 mm	190 mm

b. A Fuji Imaging Plate; 400 200 or 250x 200 mm (only these two types are available).

- c. Translation mechanism of the film cassette (PSPC shift mechanism) by a stepping motor:
 Moving range 40 mm
 Step ratio 0.002 mm/step
 Moving speed min. 0.005 mm/sec
 max. 4.0 mm/sec

- d. Rotation mechanism of the ω axis driven by a stepping motor:
 Rotation range $\pm 180^\circ$
 Step ratio 0.001 $^\circ$ /step
 Rotation speed min. 0.005 $^\circ$ /sec
 max. 2.0 $^\circ$ /sec

- e. Rotation mechanism of the μ axis driven by a stepping motor:
 Rotation range -10° to 30°
 Step ratio 0.0025 $^\circ$ /sec

- f. Collimator:
 0.4x0.4, 0.3x0.3, 0.2x0.2, 0.1x0.1 and 0.05x0.05 mm provided with an evacuation port.
 Height from base to center of optical axis: 531 mm

- g. Specimen holder
 Arc X/Y rotation driven by a stepping motor:
 Rotation range $\pm 20^\circ$
 Step ratio 0.000625 $^\circ$ /step

- h. Z direction shaft driven by a stepping motor:
 Shift range 10 mm
 Step ratio 0.0025 mm/step

- i. Goniometer head:
 Eucentric goniometer

- j. Telescope
 Magnification 20 times (fitted with a scale and cross lines)

- k. X-ray detector (curved position sensitive proportional counter-PSPC)
 Radius of detector 200 mm
 Effective range of the angular measurement (2θ) 28°
 Position accuracy 0.25 mm (0.072)
 Mounting position of PSPC It can be held at angles of 0° , 20° , 40° and 60° from the direction of incident beam. Either the PSPC or film cassette can be mounted on the same slide of the table.

- l. Multi-channel analyzer 4096 channels

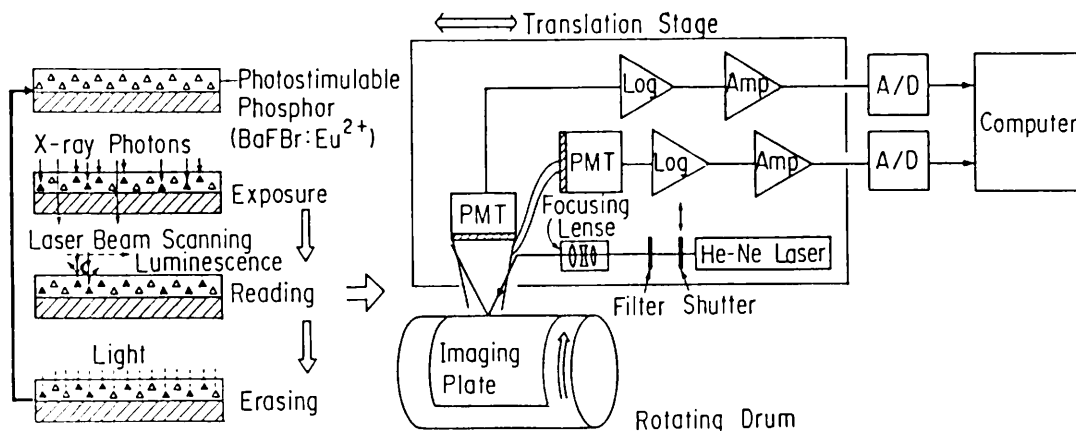


Fig. 15 Principle of Imaging Plate.

- m. Position analysis circuit..... High voltage power source for PSPC
- n. Pre-amplifier
- o. Rate-meter
- p. Layer-line screen holder

Imaging Plate (Storage Phosphor)

It is important for structure analysis to use a two-dimensional detector having a high quantum detection efficiency (DQE) and a wide dynamic range. Moreover, high counting rate capability is inevitably required in order to make the best use of the high X-ray flux of synchrotron radiation. A storage phosphor screen called an "Imaging plate" was developed for diagnostic radiography by Fuji Photo Film Co. Ltd. It was found recently that the imaging plate is also very useful for experiments of X-ray diffraction. The imaging plate stores an X-ray image without any substantial fading for several days (half life is about 16 days) and then the stored image is converted into time-series signals via photostimulated luminescence (PSL) emitted by a scanning laser beam as shown in Fig. 15.

The imaging plate (IP) is a flexible plastic plate coated with a photostimulable phosphor (BaFBr:Eu²⁺). The IP is used like photographic film but repeatedly by erasing stored images with irradiation of visible light. The grain size of the phosphor is about 5 μm, and the resolution is limited to about 150 μm due mainly to scattering of laser beam in the phosphor layer with a thickness of 150 μm.

Storing X-ray images and emitting the PSL are by the following process: Electrons of Eu²⁺ ions are released to the conduction band by X-ray irradiation and trapped at quasi-stable levels due to vacancies of Br ions (F-centers). By stimulating with visible light, the trapped electrons return to excited Eu²⁺ ions through the conduction band and then emit PSL to return to the ground state.

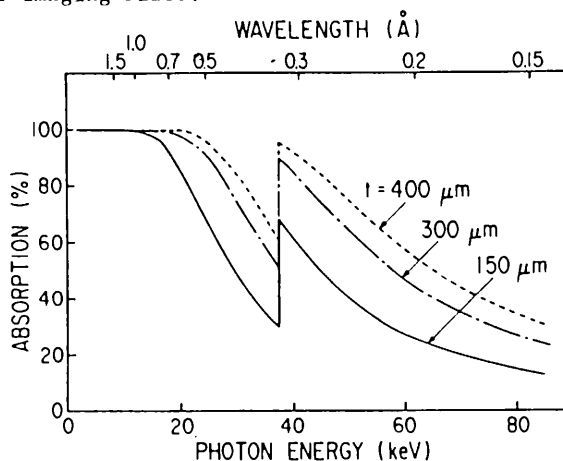


Fig. 16 X-ray absorption in photostimulable phosphor (BaFBr : Eu²⁺) as a function of wavelength.

The imaging plate has a high absorption efficiency for X-rays as shown Fig. 16, and the PSL radiation is effectively released with a response time of 0.8 μs under visible light stimulation such as a He-Ne laser beam. The intensity of PSL is linear to the incident X-ray intensity in the range from 10¹ to 4 × 10⁴ photons/pixel (pixel size = 100 × 100 μm²). The dynamic range of PSL is five orders of magnitude. The wavelength of PSL is 390 nm, sufficiently far from that of the stimulation light, to be detected with a high quantum efficiency with a conventional photomultiplier. The back ground noise of the system is less than the signal height of 3 photons per 100 × 100 μm² for MoKα. This noise level is favorably compared with the intrinsic chemical fog level of X-ray film which is, in general, equivalent to the level for about 1000 photons per the same area. Non-uniformity of response is less than 1.6 % over the entire active area. Image distortion is less than 1.0 %.

Together with these characteristics, the high sensitivity and wide dynamic range of the IP enable us to obtain high-quality images with low X-ray doses or with a very short exposure time.

1.3 Summary of beam lines and optics

Table 1 X-Ray beam lines and optics

Branch Beam Line	Horizontal Acceptance Angle (mrad)	Typical Beam Size (H mm × V mm)	Photon Flux at Sample Position	Monochromator (Crystal)	Energy Resolution ($\Delta E/E$) × 10 ⁻⁴	Energy Range (keV)	Mirror	Line Vacuum (Gas)
BL-4A	6	50 × 4 (4 × 1)		Double Crystal Si (111) (Sagittal Focusing)	~ 2	4 ~ 20	None	Vacuum
BL-4B	4.5	50 × 5		Double Crystal Si (111)	~ 2	4 ~ 35	None	Vacuum
BL-4C	4	4 × 1		Double Crystal Si (111) Sagittal Focusing	~ 2	4 ~ 20	None	Vacuum
BL-6A ₁	0.1	10 × 3		Plane (111)	7.5	8 ~ 17		Vacuum
BL-6A ₂	4	2.5 × 1		Bent Si (111) ($\alpha = 0, 6.0^\circ, 7.8^\circ, 9.5^\circ, 11.4^\circ, 13.7^\circ, 16.5^\circ$)		5 ~ 25	Bent Plane Fused Quartz	Vacuum
BL-6B	4 (6 if required)			None		4 ~ 30		Vacuum
BL-6C ₁	0.5 (4 in future)	10 × 5		None		8 ~ 30		Vacuum
BL-6C ₂	0.5	5 × 5		Channel-Cut Si (111)	7.5	8 ~ 12		Vacuum
BL-7C	4	8 × 1	$4 \times 10^9/7\text{mm}^2$ (8 keV, 100 mA) 3×10^{10} (when focused)	Double Crystal Si (111) Sagittal Focusing	2	4 ~ 20 (4 ~ 13) when focused	None	Vacuum
BL-8C (Hitachi)	5	50 × 5	$2 \times 10^6/\text{mA}\cdot\text{mm}^2$ at 10 keV with Si (111)	Channel-Cut Si (200), Si (111), Si (400)	~ 2	5 ~ 40	None	Vacuum & He
BL-9C (NEC)	5	150 × 5		Double Crystal Si (111) Sagittal Focusing	~ 2	5 ~ 25	None	Vacuum
BL-10A	1	10 × 3		Si (111), Si (220) Ge (111), InSb (111) Quartz (100), PG (002) Curved Si (111) ($\alpha \sim 4^\circ, 8^\circ$)	50 ~ 5	5 ~ 25	None	Helium

BL-10B	2	8 × 1	$3 \times 10^8 / 7\text{mm}^2$ (10 keV, 100 mA) with Si (311)	Channel-Cut Si(311) Double Si (111) Double Si (220)	1	6 ~ 30 3.5 ~ 15 5.5 ~ 25	None	Vacuum
BL-10C	4	6 × 1.5	$\sim 10^{10} / 9\text{mm}^2$ (8 keV, 100 mA)	Double Crystal Si (111) Fixed Beam Position	2	4 ~ 10	Bent Cylinder	Helium
BL-14A	1.28 (Vertical)	5 × 38		Double Si (111) Double Si (331) Double Si (553)	2	5.1 ~ 19.1 12.9 ~ 48 22.7 ~ 84.5	Bent Cylinder for Vertical Focusing, Pt-cated Fused Quartz	Vacuum (line) He(monochromator)
BL-14B	2.2	5 × 30		Double Si (111), Si (220), Si (311) Sagittal Focusing	2	5.2 ~ 57	None	Vacuum
BL-14C	1.3	10 × 40		Double Si (111)	2	5.5 ~ 43	None	Vacuum
BL-15A	2	2.6 × 1.3	$9 \times 10^{10} / 6\text{mm}^2$ (8.0 keV, 150 mA)	Curved Ge (111) ($\alpha=8.0^\circ$)	~ 10	5.6 ~ 12.4	Cylinder, Fused Quartz	Vacuum and He
BL-15B	0.14	5 × 5		None		3.5 ~ 34	None	Vacuum
BL-15C	2	60 × 6		None		4 ~ 35	None	Vacuum
BL-16X (under construction)	4	4 × 1		Double Crystal Si (111) Sagittal Focusing	~ 2	4 ~ 35	Currently None	Vacuum
BL-17C (Fujitsu)	1	20 × 5		None		~ 1	Quartz (plane)	Vacuum

Table 2 VUV and Soft X-ray beam lines and optics

Branch Beam Line	Monochromator					Pre - Mirrors							Refocusing Mirrors							
	Monochromator	Grating (Crystal)	Groove Density (λ/mm)	Blaze (A)	Resolution	Wavelength Range (A)	Type	Radius of Curvature (mm)	Angle of Incidence	Material	Coating Material	Dimensions (mm)	Horizontal & Vertical Acceptance (mrad)	Type	Radius of Curvature (mm)	Angle of Incidence	Material	Coating Material	Dimensions (mm)	Beam Size (mm)
BL-1A (NTT)	Grating/Crystal Monochromator	Au-Coated Original InSb(111) Si(111)	1200 2d=7.4806 A 2d=6.27064 A		$\lambda/\Delta\lambda \sim 2000^*$	2 ~ 2000	Paraboloidal		89°	Fused Quartz	Pt	500 ^h ×80 ^w ×50 ^t	4.0 ^h ×0.5 ^v	Paraboloidal		89°	Fused Quartz	Pt	500 ^h ×80 ^w ×50 ^t	4 ^h ×1 ^v
BL-1B (NTT)	Filtered White						Plane		88° ~ 89°	SiC			1.2 ^h ×4.0 ^v						19 mm ϕ	
BL-1C (NTT)	Filtered White						Toroidal		86°	Fused Quartz	Pt		2.0 ^h ×4.0 ^v						2 ^h ×10 ^v	
BL-2A	Double Crystal Monochromator with Constant Exit Beam	InSb(111)	2d=7.4806 A			7.3 ~ 2.0														
BL-2B ₁	Fresnel Zone Plate Microscope					30 ~ 15	Plane	—	88°	SiC	Pt	120 ^h ×60 ^w ×15 ^t	—							
BL-2B ₂	10m Grazing Incidence Monochromator with Fixed Incidence Angle of 89°	Hitachi Au-Coated Replica (pyrex)	2400 1200	8 16	$\Delta\lambda=0.004 \text{ A}^*$ $\Delta\lambda=0.008 \text{ A}$ for 10 μ -10 μ Slits	6 ~ 25 6 ~ 50	Plane Concave Concave	— 8903 7527	86.85° ~ 88.83° 89° 89°	SiC Pyrex Pyrex	Pt Pt Pt	120 ^h ×60 ^w ×15 ^t 90 ^h ×15 ^w ×15 ^t 90 ^h ×15 ^w ×15 ^t	0.14 ^h ×0.4 ^v							
BL-7A (RCS)	Grazing Incidence	Plane Au-Coated (Hitachi)	1200		$\lambda/\Delta\lambda \sim 500$	12 ~ 1200	Bent Cylinder	R=7.83×10 ⁵ $\rho=420$	1.6°	Quartz	Pt	750×140×30	6×1	Toroidal	R=2.58×10 ⁴ $\rho=0.09$	1.7°	Quartz	Pt	200×60×18	2×1
BL-7B (RCS)	1m Seya-Namioka	Concave Au-Coated (Hitachi, B&L)	1200 2400	380 960 1600	$\lambda/\Delta\lambda > 1000$	275 ~ 2500	Cylinder	1600	15°	Cu	Pt	250×80×30	6×4	Toroidal	R=2510 $\rho=200$	10°	Quartz	Pt	60×80×20	1×1
BL-8A (Hitachi)	Grazing Incidence	Plane Self-focusing	2400 800	5 80	$\lambda/\Delta\lambda \sim 10^{-3}$	7 ~ 100 80 ~ 300	Plane	∞	1°	Quartz	Pt	400×170×40	0.5 ^h ×1.0 ^v	Bent	6.5×10 ⁴	1°	Quartz	Pt	160×50×5	5×1
BL-8B (Hitachi)	Double Crystal	InSb(111) Beryl(10 $\bar{1}$ 0) Si(220), (422)			$\lambda/\Delta\lambda \sim 10^{-3}$	0.04 ~ 1.5								Toroidal	R=1.6×10 ³ $\rho=1.7\times 10^2$	5 mrad	Quartz	NI	500×120×30	6×2
BL-9A (NEC)							Plane Cylinder	∞ 309.5	0.85° 0.85°	SiC SiC		400×170×40 400×170×40	5×0.33 5×0.33							
BL-11A	Grasshopper Mark VII 2m Grazing Incidence Fixed Incidence Angle of 88° (2GH)	Hitachi Au-Coated Replica (Pyrex)	2400 1200	16.6 33.3	$\Delta\lambda=0.02 \text{ A}^*$ $\Delta\lambda=0.04 \text{ A}$ for 10 μ -10 μ Slits	10 ~ 145 10 ~ 290	Spherical Spherical	360000 28000	88° 88°	Fused Quartz Fused Quartz	Pt Au	400 ^h ×170 ^w ×40 ^t 300 ^h	1.3 ^h ×0.4 ^v	Bent Cylinder	R \sim 3000	89°	Pyrex	Pt	220 ^h ×24 ^w ×6 ^t	8 ^h ×0.3 ^v
BL-11B	Double Crystal Monochromator (DXM)	Ge(111) InSb(111) Beryl(10 $\bar{1}$ 0)	2d=6.53 A 2d=7.4806 A 2d=15.9 A		$\Delta E=1\text{eV}$ at 2KeV $\Delta E=0.8\text{eV}$ at 2KeV $\Delta E=0.6\text{eV}$ at 1KeV	2.7 ~ 6.2 3 ~ 7 8 ~ 16	Bent Cylinder	$\rho=300$ R \sim 950000	89°	Fused Quartz	Pt	580 ^h ×140 ^w ×30 ^t	4.0 ^h ×0.6 ^v							8 ^h ×1 ^v
BL-11C	1m Seya-Namioka Constant Deviation of 70° (SSN)	Hitachi Au-Coated Replica Hitachi Al-Coated Replica	2400 1200 1200	785 785 785	$\Delta\lambda=0.3 \text{ A}$ at 500 A for 50 μ -50 μ Slits	400 ~ 1500 400 ~ 3000	Plane Concave	— 5600	77.5° 42.5°	SiC Fused Quartz	none Pt	250 ^h ×100 ^w ×40 ^t 100 ^h ×100 ^w ×20 ^t	4.8 ^h ×3.0 ^v	Toroidal	$\rho=2000$ R=125	72.5°	Pyrex	Au	90 ^h ×50 ^w ×10 ^t	$\sim 1\phi$

Branch Beam Line	Monochromator				Pre - Mirrors						Refocusing Mirrors																
	Monochromator	Grating (Crystal)	Groove Density (1/mm)	Blaze (A)	Resolution	Wavelength Range (A)	Type	Radius of Curvature (mm)	Angle of Incidence	Material	Coating Material	Dimensions (mm)	Horizontal & Vertical Acceptance (mrad)	Type	Radius of Curvature (mm)	Angle of Incidence	Material	Coating Material	Dimensions (mm)	Beam Size (mm)							
BL-11D	2m Grazing Incidence Constant Deviation Monochromator (CDM) $\alpha + \beta = 154^\circ$	B & L	2400	32	$\lambda/\Delta\lambda \sim 1700$ for 25 μ -25 μ Slits	80 ~ 150	Cylindrical	$\rho=750$	86°	SiC	Pt	400 ^h ×60 ^w ×40 ^t	1.5 ^h ×2.0 ^v	Toroidal	$\rho=400$ R=3100	77°	BK-7	Au	60 ^h ×40 ^w ×10 ^t	0.5 ^h ×0.5 ^v							
		Hitachi Au-Coated Replica	1200	116		120 ~ 300	Plane	—	86°			Fused Quartz BK-7									Au	50 ^h ×40 ^w ×10 ^t					
BL-12A	1m Seya-Namioka Constant Deviation of 70° (GSN)	B & L	2400	508	$\Delta\lambda=0.4$ A at 500 A for 100 μ -100 μ Slits	350 ~ 1000	Cylindrical	$\rho=1850$	80°	SiC	none	250 ^h ×200 ^w ×40 ^t	2.4 ^h ×1.5 ^v	Plane	—	80°	Pyrex	Pt	40 ^h ×40 ^w ×10 ^t	$\sim 1\phi$							
		Hitachi Au-Coated Replica	1200	536		120 ~ 300	Spherical	6250	45°			Fused Quartz							Pt		100 ^h ×20 ^t	Toroidal	$\rho=340$ R=2000	70°	Pyrex	Pt	40 ^h ×40 ^w ×10 ^t
		—	—	—		—	—	—	—			—							—		—	—	—	—	—	—	—
BL-12B	6.65m Normal Incidence Off-Plane Eagle Mounting (6VOPE)	B & L Pt-Coated Replica	1200	1500	$\lambda/\Delta\lambda=2.5 \times 10^5$ A at ~ 800 A	400 ~ 2500	Plane	—	80°	SiC	none	280 ^h ×100 ^w ×40 ^t	5.0 ^h ×3.6 ^v	—	—	—	—	—	—	—	—						
		B & L Os-Coated Replica	1200	5500			Concave	4321	35°			Pyrex										Pt	110 ^h ×20 ^t				
		Hyperfine Os-Coated Replica	4800	900			Concave	2188.5	45°			Pyrex										Pt	110 ^h ×20 ^t				
BL-12C	Channel-cut Double Crystal	InSb(111)	2d=7.4806A	—	—	3 ~ 8 or white	plane	—	89°	SiC	Pt	400×100×40	1.0 ^h ×0.6 ^v	—	—	—	—	—	—	—							
BL-16U (under construction)	Grazing Incidence	Hitachi Au-Coated Replica (Concave)	1200	42.15	$\lambda/\Delta\lambda > 1000$	20 ~ 300	Spherical plane	205294	87°	SiC	Pt	500×50×40	1.74×0.24	Bent Cylinder	$\rho=52.4$	86.22°	Quartz	Pt	220×30×8	Arb.							
							Spherical	1796	87°			100×40×15									100×40×15						
BL-17C (Fujitsu)	—	—	—	—	—	—	Plane	—	$\sim 0.6^\circ \sim 1^\circ$	Quartz	Pt	500×130×30	1.0 ^h ×0.5 ^v	—	—	—	—	—	—	—							

* nominal value

2. LIST OF APPARATUSES

Format

Name of apparatus

1. General characteristics
2. Accessories
3. Other features
4. Typical Experiment
5. Station used
6. Responsibility
7. Pages in (A) "Act. Rept. 82/83", (B) "Act. Rept. 83/84" (c) "Act. Rept. 84/85" and (D) "Act. Rept. 86" describing the details

X-ray

(a) X-ray fluorescence spectrometer

1. Energy dispersive type spectrometer. Equipped with a Si(Li) detector. Elemental analysis with very high sensitivity.
2. X-Z scanning sample stage.
- 3.
4. Trace element analysis of semiconductor, ceramics, sea water, human tissues etc. Surface elemental analysis of semiconductor.
5. BL-4A.
6. A. Iida
7. V-23 in (A)

(b) Monochromatic X-ray irradiation system for radiation biology studies

1. Usable wavelength region, 0.8 Å - 3.0 Å. Beam size, typically 30 mm(H) × 3 mm(V).
2. X-Z sample scanning stage. Ionization chambers for measuring X-ray intensity.
- 3.
4. Studies on Auger enhancement of Bromine atom using various biological samples. Wavelength dependence of radiation effects on biological samples.
5. BL-4A.
6. K. Kobayashi
7. V1-21 in Act. Rept. 84/85.

(c) X-ray diffractometer for liquids and melts

1. Collects intensity-data for radial distribution analysis for non-crystalline materials such as gases, liquids, melts and glasses.
2. θ - 2θ goniometer with monochromator and analyzer. Single-crystal monochromator with quartz and β -alumina. Double crystal monochromator with Si(111). Keramax furnace
- 3.
4. Energy-dispersive study of gas and liquid. Angle-dispersive study of liquids, melts and powder crystals.
5. BL-4B.
6. K. Ohsumi
7. V-24 in (A)

(d) Four-circle Diffractometer with a Crystal Analyser

1. Enables high resolution measurement, in momentum and energy, of intensity distribution. Intensity measurement from the samples at high pressures or at low temperatures is also possible.
2. Liquid nitrogen cryostat.
- 3.
4. High resolution measurement of diffuse scattering intensity, pressure dependence of commensurate-incommensurate transition.
5. BL-4C.
6. S. Kishimoto
7. p.160 in (D)

(e) Focusing Weissenberg camera with multi-layer-linescreens

1. Useful for high resolution macromolecular crystallography. High signal-noise ratio. Equipped with multi-layer-line screens.
2. Cooling unit by N₂ gas.
3. Wide range of ω -axis rotation. Wide 2θ range.
4. X-ray structure determination of macromolecular crystal (insulin, actin-DNase I complex, Plasminostreptin, etc.)
5. BL-6A₂.
6. N. Sakabe
7. VI-5 in (A)

(f) Multi anvil high pressure X-ray system

1. Maximum pressure 13 GPa. Maximum temperature 1700°C. Sample volume (typical) 2 mm ϕ × 3 mmh. Uses white X-ray.
2. Two axis goniometer. Handy type SSD.
3. Best quality in the world for this research field.
4. Compressibility of Au at room and high temperatures. Time resolved observation of B1-B2 transition of BaS.
5. BL-14C.
6. T. Kikegawa
7. V-26 in (A)

(g) Low temperature X-ray diffractometer

1. Equipped with a three-axis goniometer ($\omega, 2\theta, \chi$) mainly used for low temperature (≥ 0.3 K) X-ray diffraction.
2. Some types of refrigerators and magnets.
3. Available addendum limited to 500 kg in weight.
4. Peiels transition in K_{0.3}MoO₃
5. BL-6C.
6. T. Nakajima
7. V-25 in (A)

(h) EXAFS spectrometer (II)

1. Designed for X-ray absorption spectroscopy in transmission mode and in fluorescence detection mode.
2. Control and data acquisition system. Closed cycle refrigerator.

3. The beam height measured from top of optical bench is the same as that of BL-10B.
 4. EXAFS
 5. BL-7C.
 6. M. Nomura
 - 7.
- (i) Vertical-type four-circle diffractometer
1. Used for crystallographic studies and scattering experiments. Large X-circle (280 mm ϕ).
 2. Control system with MELCOM 70/30. High-temperature furnace. X-rays film cassette.
 - 3.
 4. Study on anomalous scattering effect.
 5. BL-10A.
 6. S. Sasaki
 7. V-27 in (A)
- (j) EXAFS Spectrometer (I)
1. Dedicated to X-ray absorption spectroscopy. High-resolution. Easy operation.
 2. Control system with a microcomputer (SORD M-223). Closed cycle refrigerator. Reaction chamber for catalyst. Furnace.
 - 3.
 4. EXAFS
 5. BL-10B.
 6. A. Koyama, M. Nomura
 7. V-8 in (A)
- (k) Small angle X-ray scattering equipment for solutions (SAXES)
1. Dedicated to small-angle scattering for solutions, synthetic polymers.
 2. Stopped flow apparatus. Temperature jump apparatus. Flash light for specimen.
 3. Uses monochromatic beam from the optics installed at BL-10C.
 4. Measurements for Bovine Serum Albumin, Lysozyme, Tobacco Mosaic Virus, Purple Membrane, etc.
 5. BL-10C.
 6. K. Kobayashi
 7. V-29 in (A)
- (l) Ultra-high vacuum X-ray diffractometer
1. Ultra-high vacuum with cryo-pumping system. Equipped with X-ray diffractometer and LEED optics.
 2. Super precision goniometer using elastic torsion mechanism. Microcomputer control system. NaI scintillation counter system and SSD.
 - 3.
 4. Study on Si(7 \times 7) structure.
 5. BL-10C.
 6. T. Ishikawa
 7. V-34 in (A)
- (m) Time-Resolved X-ray measurement system with 1D-PSD
1. Time resolution up to 1 msec. Either 256 ch. \times 191 frames, 512 ch. \times 95 frames, or 1024 ch. \times 47 frames. Fast data acquisition up to 1 MHz.
2. I.SI 11/23 computer. CAMAC modules (Time to Digital Converter, Histogramming Memory, etc.).
 3. Uses monochromatic X-ray ($\lambda=1.5\text{\AA}$).
 4. Measurements on frog skeletal muscle, purple membrane, Ribosome, etc.
 5. BL-10C, BL-15A1.
 6. Y. Amemiya
 7. V-35 in (A)
- (n) Horizontal-type four circle diffractometer
1. Specially built, but having a conventional diffractometer configuration. Fully computer-controlled for rapid, tunable and precise diffraction data collection.
 2. Computer-controlled alignment carriage with 5 stepping motor driven axes, on which the diffractometer is mounted. Rotation camera. MELCOM 70/60 minicomputer with OPTRONICS film scanner.
 3. Mechanical control interfaced through IEEE-488 bus. CAMAC and NIM measuring system.
 4. Crystal structure analysis of antibiotics, biotic metabolites, proteins, etc.
 5. BL-14A.
 6. Y. Satow
 7. V-30 in (A)
- (o) High-speed X-ray topography Camera
1. Equipped with two X-ray TV cameras. Maximum load of 30 kg on sample goniometer. Facilitates simultaneous observation of two different Laue spots.
 2. Microcomputer system (AIDACS-3000). Image processor TF4110. Work shutter for variable exposure time (0.1 \sim 9.9sec).
 3. 1 arc sec accuracy of θ -rotation. Ample space around the specimen position.
 4. Melting process of GaAs. Magnetization process of Fe-3% Si, etc.
 5. BL-15B, BL-14C.
 6. H. Kawata
 7. V-31 in (A)
- (p) X-ray diffractometer for gasses
1. Equipped with horizontal ω -2 θ two-circle goniometer. X- ϕ circle motion available.
 2. Gas cell with boiling system. Gas cell for pressure tight experiments. Incident beam monitor with SSD.
 3. Uses white beam for energy-dispersive method. Uses monochromatic beam for angle-dispersive method.
 4. Angle-dispersive X-ray diffraction and Compton scattering study of carbon dioxide.
 5. BL-15C, 14C.
 6. T. Mitsuhashi
 7. VI-172 in (B)
- (q) Three-axes X-ray Diffractometer
1. Equipped with three precision goniometers (Huber 410, 420, and 440).
 2. Scintillation counter. SSD with MCA. Asymmetry cut plane monochromator.
 3. Having precision of 0.36 arc sec per pulse.

4. Phase-contrast microscopy.
Development of application to medical diagnosis.
 5. BL-15B.
 6. H. Kawata
 7. V-32, VI-97, VI-98 in (A)
- (r) Precision X-ray optics
1. Goniometer assembly dedicated to precision diffraction study such as double-, triple-, and more than triple-crystal diffractometry and topography.
 2. Microcomputer control system.
NaI scintillation detector system.
SSD and MCA.
Ionization chamber for monitoring.
Room temperature controller.
Experimental table with air springs
 3. 1 arc sec accuracy for full rotation.
0.1 arc sec accuracy within 6° using tangential bar system.
Employs super-precision rotation mechanism with elastic torsion and PZT.
 4. Detection of polarization rotation under magnetic diffraction condition.
Structure analysis of epitaxial layer/substrate interfaces with standing wave method.
 5. BL-15C.
 6. T. Ishikawa
 7. V-33 in (A)
- (s) Rapid acquisition system of two dimensional images for medical application
1. Dedicated to development of medical diagnosis using two-dimensional image acquisition system.
Large exposure area ($70 \text{ mmH} \times 120 \text{ mmV}$) is obtained by asymmetrical reflection from a crystal.
Usable energy is $33 \text{ KeV} \pm 3 \text{ KeV}$.
 2. Two-dimensional detector system using a metal image intensifier (I.I.).
Polished Si single-crystal monochromator with 311 reflection.
Z scanning table detector and sample.
X scanning stage for sample.
 - 3.
 4. Studies on medical application to diagnosis such as angiography, K-edge subtraction and computed tomography.
 5. AR-NE4A1.
 6. K. Hyodo
 - 7.
- (t) EXAFS spectrometer (NEC)
1. Designed for X-ray absorption spectroscopy in transmission mode and in fluorescence detection mode.
 2. Control and data acquisition system, closed cycle refrigerator ($GK \leq T \leq 300 \text{ K}$).
 3. Focused beam is available.
 4. EXAFS.
 5. BL-9C.
 - 6.
 - 7.
- (u) High-precision Triple-Crystal X-ray Diffractometer (NEC)
1. Equipped with three crystal stages whose height can be changed. Mainly used for a grazing incidence diffraction, X-ray topography.
2. Two high-precision goniometers ($0.01''/\text{pulse}$ for θ , $0.004^\circ/\text{pulse}$ for 2θ), two 220ϕ goniometers ($0.0002^\circ/\text{pulse}$ for θ , $0.0004^\circ/\text{pulse}$ for 2θ), a 400ϕ goniometer ($0.002^\circ/\text{pulse}$ for θ), a goniometer for grazing incidence diffraction.
 - 3.
 4. X-ray topograph. Grazing incidence X-ray diffraction.
 5. BL-9C.
 - 6.
 - 7.
- (v) Six-circle-X-ray diffractometer (NEC)
1. Useful for a study of crystal structure for single crystal under various conditions (pressure & temperature).
 2. Closed cycle refrigerator ($13 \text{ K} \leq T \leq 300 \text{ K}$), image furnace ($300 \text{ K} \leq T \leq 800 \text{ K}$).
 - 3.
 4. Single crystal X-ray diffraction. Diffuse scattering.
 5. BL-9C.
 - 6.
 - 7.
- Soft X-ray and VUV
- (a) Monochromatic soft X-ray irradiation system for radiation biology studies
1. Usable wavelength $3 \text{ \AA} \sim 6.5 \text{ \AA}$.
Beam size, typically $7 \text{ mm (H)} \times 4 \text{ mm (V)}$.
 2. X-Z sample scanning chamber.
 - 3.
 4. Biological effects of soft X-ray resonance absorption around the K-shell absorption edge of phosphorus.
 5. BL-1B.
 6. K. Kobayashi
 7. in (D)
- (b) Gas phase angle resolved photoelectron spectrometer
1. Ultimate pressure $5 \times 10^{-8} \text{ Torr}$.
Equipped with a conventional hemispherical electrostatic analyzer and with a position-sensitive parallel-plate electrostatic analyzer.
 2. Sample-gas inlet system.
 3. A sample gas is confined in a gas cell.
 4. The measurements of absolute intensity and polarization of synchrotron radiation from the undulator.
 5. BL-2, BL-12A.
 6. A. Yagishita
 7. V-42 in (A)
- (c) VUV and Soft X-ray Reflectometer
1. Equipped with a goniometer, insuring accurate incidence angle (30 sec).
Up to 89.4° incidence angle.
Easy optical alignment.
Easy sample exchange.
High vacuum ($2 \times 10^{-9} \text{ Torr}$).
 - 2.
 3. Equipped with ports for vacuum evaporation.
 4. Optical constants of mirror materials.
Surface roughness.
 5. BL-11A.
 6. T. Miyahara
 7. V-41, VI-78 in (A)

- (d) UHV experimental chamber for absorption measurements I.
1. Ultra-high vacuum (1×10^{-10} Torr).
Equipped with an electron-beam gun for evaporation of samples.
Equipped with a quartz oscillator capable of being cooled to LNT.
 2. Sample holder with an adjustable linear motion, capable of being cooled to LNT.
 3. Designed mainly for very reactive metal samples.
 4. Absorption measurement of alkali metals, alkali metal alloys, and rare earth metals. VI-114
 5. BL-11C, BL-11D.
 6. T. Miyahara
 7. VI-82 in (A)
- (e) Apparatus for ARPES experiment for solid state
1. Base pressure 5×10^{-11} Torr.
Equipped with a hemispherical analyzer mounted on a two axis rotation mechanism.
 2. Some equipments for sample preparation and characterization.
Sample bank and transfer system.
Sample gas inlet system.
 - 3.
 4. Mainly for angle-resolved photoelectron spectroscopy (ARPES) of single crystals.
 5. BL-11D.
 6. H. Kato
 7. V-10 in (B)
- (f) Time-of flight spectrometer for photoion measurements
1. Ultimate pressure 5×10^{-8} Torr.
Electrostatic lenses satisfying the conditions of single-field space focusing for threshold electrons and double-field space focusing for ions.
 2. Furnace to evaporate alkali-and alkaliearth-metals.
 - 3.
 4. The measurements of single and double-photoionization cross sections of Ca and Sr.
 5. BL-12A.
 6. A. Yagishita
 7. V-40 in (A)
- (g) Multi-technique surface analysis system (NTT)
1. Surface analyses such as photoemission spectroscopy, surface EXAFS, AES, SIMS, LEED EELS and ISS in conjunction with an MBE chamber.
 2. CLAM analyzer, angle-resolved electron analyzer, LEED optics, Q-mass filter, X-ray source, ELS electron gun, auger electron gun, He ion gun.
 - 3.
 4. Surfaces and Interfaces of semiconductors and superconductors by using SRPES and SEXAFS.
 5. BL-1A.
 6. M. Oshima (NTT)
 7. p.144-117 in (D)
- (h) Angle resolved electron spectrometer (RCS)
1. Electron spectroscopy for surface studies.
2. Low energy electron diffraction, auger electron spectroscopy, surface preparation tools.
 3. Based on beam line ADES 400 of V.G.
 4. Photoelectron spectroscopy, surface EXAFS.
 5. BL-7A and 7B.
 6. H. Namba (University of Tokyo)
 - 7.
- (i) X-ray lithography (Fujitsu Lab.)
1. X-ray lithography.
 2. Low-pass mirror, Energy dispersive type spectrometer with a Si(Li) detector.
White beam is available.
 3. X-ray lithography.
 4. BL-17C.
 - 5.
 - 6.
 - 7.

**PHOTON FACTORY
ACTIVITY REPORT**

1987

PHOTON FACTORY ACTIVITY REPORT 1987

#5

5

PF
10th
Anniversary



NATIONAL LABORATORY FOR HIGH ENERGY PHYSICS, KEK